Deep learning based image analysis identifies a DAT-negative subpopulation of dopaminergic neurons in the lateral Substantia nigra.

Nicole Burkert[1*], Shoumik Roy[1*], Max Häusler[1*], Dominik Wuttke[2,3], Sonja Müller[1], Johanna Wiemer[1], Helene Hollmann[1], Jorge Ramirez-Franco[4,5], Julia Benkert[1], Michael Fauler[6], Johanna Duda[1], Christina Pötschke[1], Jean-Marc Goaillard[4,5], Moritz Münchmeyer[3], Rosanna Parlato[1#], Birgit Liss[1,7]

* These authors contributed equally

Present address: Division of Neurodegenerative Disorders, Department of Neurology, Mannheim Center for Translational Neurosciences, Heidelberg University, Germany.

[1] Institute of Applied Physiology, Medical Faculty, Ulm University, 89081 Ulm, Germany

[2] Wolution GmbH & Co. KG, 82152 Munich, Germany

[3] University of Wisconsin-Madison, Dept. of Physics, Madison, WI, US

[4] UMR_S 1072, Aix Marseille Université, INSERM, Faculté de Médecine Secteur Nord, Marseille, France

[5] INT, Aix Marseille Université, CNRS, Campus Santé Timone, Marseille, FRANCE

[6] Institute of General Physiology, Medical Faculty, Ulm University, 89081 Ulm, Germany

[7] Linacre College & New College, Oxford University, OX1 4 BH Oxford, UK

Corresponding author:

Birgit Liss
Institute of Applied Physiology, Medical Faculty, University of Ulm
Albert-Einstein-Allee 11, 89081 Ulm, Germany
Phone: +49 731 50 36214
E-mail: birgit.liss@uni-ulm.de

Abstract

Here we present a deep learning-based image analysis platform (DLAP), tailored to autonomously quantify numbers of neuronal subtypes in defined areas, and of fluorescence signals, derived from RNAscope probes or immunohistochemistry, in defined cellular compartments. As proof-of-principle, we utilized DLAP to analyse subtypes of dopaminergic midbrain neurons in mouse and human brain-sections. These neurons modulate complex behaviour like voluntary movement, and are differentially affected in Parkinson's and other diseases. DLAP allows the analysis of large cell numbers from different species, and facilitates the identification of small cellular subpopulations, based on differential mRNA- or protein-expression, and anatomical location. Using DLAP, we identified a small subpopulation of dopaminergic midbrain neurons (~5%), mainly located in the very lateral Substantia nigra (SN), that was immunofluorescence-negative for the plasmalemmal dopamine transporter (DAT). These results have important implications, as DAT is crucial for dopamine-signalling, and its expression is commonly used as marker for dopaminergic SN neurons.

Introduction

Dopamine releasing (DA) neurons within the midbrain are important for a variety of brain functions and behavioral processes like voluntary movement control, learning, cognition, and motivation (Berke, 2018; Björklund & Dunnett, 2007; Liu & Kaeser, 2019; Wise, 2004). The cell bodies of DA midbrain neurons are predominantly located in two overlapping nuclei, the Substantia nigra pars compacta (SN) and the ventral tegmental area (VTA), with axonal projections to the dorsal striatum, and the ventral striatum and prefrontal cortex, respectively (Gantz, Ford, Morikawa, & Williams, 2018; Haber & Fudge, 1997; Halliday, Reyes, & Double, 2012; Roeper, 2013). In line with these differential functions and projections, dysfunction of the dopaminergic midbrain system can lead to severe diseases like Parkinson's, Schizophrenia, addiction, or attention deficit hyperactivity disorders (ADHD) (A. P. F. Chen, Chen, Kim, & Xiong, 2021; Klein et al., 2019; Lerner et al., 2015; Montero et al., 2021). Importantly, not all DA midbrain neurons are affected equally in these diseases. More precisely, in Parkinson's disease (PD), the second most common neurodegenerative disorder, a subpopulation of mesostriatal SN DA neurons is progressively degenerating, while neighboring VTA DA neurons remain largely intact (Bloem, Okun, & Klein, 2021; P. Damier, E. C. Hirsch, Y. Agid, & A. M. Graybiel, 1999; Hirsch, Faucheux, Damier, Mouatt-Prigent, & Agid, 1997; Surmeier, Obeso, & Halliday, 2017). In contrast, in Schizophrenia, mesocorticolimbic VTA DA neurons display complex dysfunctions, while SN DA neurons are mainly unaffected (Jauhar, Johnstone, & McKenna, 2022; Kegeles et al., 2010; Owen, Sawa, & Mortensen, 2016). The cause for this differential vulnerability of dopaminergic midbrain neurons is still unclear, and up to now, only unspecific, symptomatic therapies are available, with their respective side-effects (Smeland, Frei, Dale, & Andreassen, 2020; Vijiaratnam, Simuni, Bandmann, Morris, & Foltynie, 2021).

One prerequisite for curative and cell-type specific therapies is a better understanding of the distinct subpopulations of dopaminergic neurons and their selective pathophysiology (Gantz et al., 2018; Roeper, 2013). Analysis of mRNA and protein expression with single cell resolution and its correlation with anatomical locations and projections in health and disease states is an essential approach for identifying molecular determinants of differential neuronal vulnerability (Dumrongprechachan et al., 2021; Glock et al., 2021; Benjamin D. Hobson et al., 2022; B. D. Hobson et al., 2022; Paget-Blanc et al., 2022). To address this, labelling of mRNA or proteins in tissue sections, followed by microscopic imaging, are important tools, as spatial distribution and tissue context are preserved (Jonkman, Brown, Wright, Anderson, & North, 2020; Lichtman & Conchello, 2005; Reilly & Obara, 2021). However, manual neuronal mapping, cell counting, and quantification of mRNA- and protein-derived fluorescence signals is very time consuming and prone to human error (Maier-Hein et al., 2018; Sommer & Gerlich, 2013; Xu et al., 2019).

84 Here we present a deep learning-based image analysis platform (DLAP) that overcomes these
85 issues. Our single cell DLAP approach and six individual algorithms were tailored to
86 autonomously quantify (i) the number of distinct neuronal types in defined areas, as well as (ii)
87 fluorescence signals, derived from either RNAscope probes (mRNA) or immunohistochemistry
88 (proteins), in defined cellular compartments - more precisely, in plasma-membranes, cell
89 body/cytoplasm, and nuclei of individual neurons. This is desired, as advanced methodologies
90 are leading to increasingly large biological datasets (Greener, Kandathil, Moffat, & Jones,
91 2022), and the general need for their efficient, unbiased, and reproducible analysis (Krenn et
92 al., 2022; Moen et al., 2019). We utilized artificial neuronal networks (ANN) based deep
93 learning approaches for image analysis. ANN are biologically inspired computer programs,
94 designed to simulate the way in which the human brain processes information. ANN gather
95 their knowledge by detecting the patterns and relationships in data (segementation), and learn
96 (or are trained) through experience, not by programming (Agatonovic-Kustrin & Beresford,
97 2000; Hassabis, Kumaran, Summerfield, & Botvinick, 2017; LeCun, Bengio, & Hinton, 2015;
98 Yang & Wang, 2020). ANN consist of artificial neurons, arranged in different layers
99 (Angermueller, Pärnamaa, Parts, & Stegle, 2016; Greener et al., 2022), where each
100 consecutive layer obtains inputs from its preceding layer. As only the first (input) and the last
101 (output) layer are visible/accessible, all layers in between are referred to as hidden layers.
102 Network architectures containing hundreds of hidden layers are called deep networks (LeCun
103 et al., 2015). After suitable training, deep learning networks can effectively extract relevant
104 cellular features for automated image analysis (Falk et al., 2019).

105 To facilitate easy adaption to the most common respective tasks in life-science, we have
106 predesigned six algorithms, based on two distinct network structures, DeepLab3 (DL3) and
107 fully convolutional neural networks (FCN) (L. C. Chen, Papandreou, Kokkinos, Murphy, &
108 Yuille, 2018; Long, Shelhamer, & Darrell, 2015). We trained them to detect, count, and analyse
109 individual DA midbrain neurons, labelled for tyrosine hydroxylase (TH), the key-enzyme for
110 synthesis of dopamine and other catecholamines (Daubner, Le, & Wang, 2011). However, the
111 flexible design of the algorithms and the workflow allows quick and easy adaptions to other
112 cell types and specimens, and thus is of general interest.

113 Here we detail the DLAP pipeline, including all six predesigned algorithms for automated image
114 processing, and we demonstrate its reliable identification and count of cells in defined areas,
115 as well as fluorescence-signal quantification in cellular compartments. By using this approach
116 for quantification of the immunofluorescence signal of the plasmalemma dopamine transporter
117 (DAT) in TH-positive SN neurons, we identified a small subpopulation of DAT immuno-negative
118 DA neurons, mainly located in the very lateral parts of the SN (~5 % of TH-positive SN
119 neurons). The DAT is an electrogenic symporter and a member of the Na^+/Cl^- dependent
120 transporter family (SLC6). It is crucial for re-uptake of dopamine at somatodendrites and

axons, and also mediates electric conductances (Ryan, Ingram, & Scimemi, 2021). The identification of a DAT negative SN DA neuron population has not only physiological relevance (Bu, Farrer, & Khoshbouei, 2021; Miller et al., 2021; Savchenko et al., 2022), but it has additional implications, as DAT is commonly used as marker for SN DA neurons and for their specific targeting, e.g. to generate DA neuron specific knock out mice, expressing Cre-recombinase under the control of the DAT-promoter (Gong et al., 2007; Stephan Lammel et al., 2015; Papathanou, Dumas, Pettersson, Olson, & Wallén-Mackenzie, 2019; Stuber, Stamatakis, & Kantak, 2015).

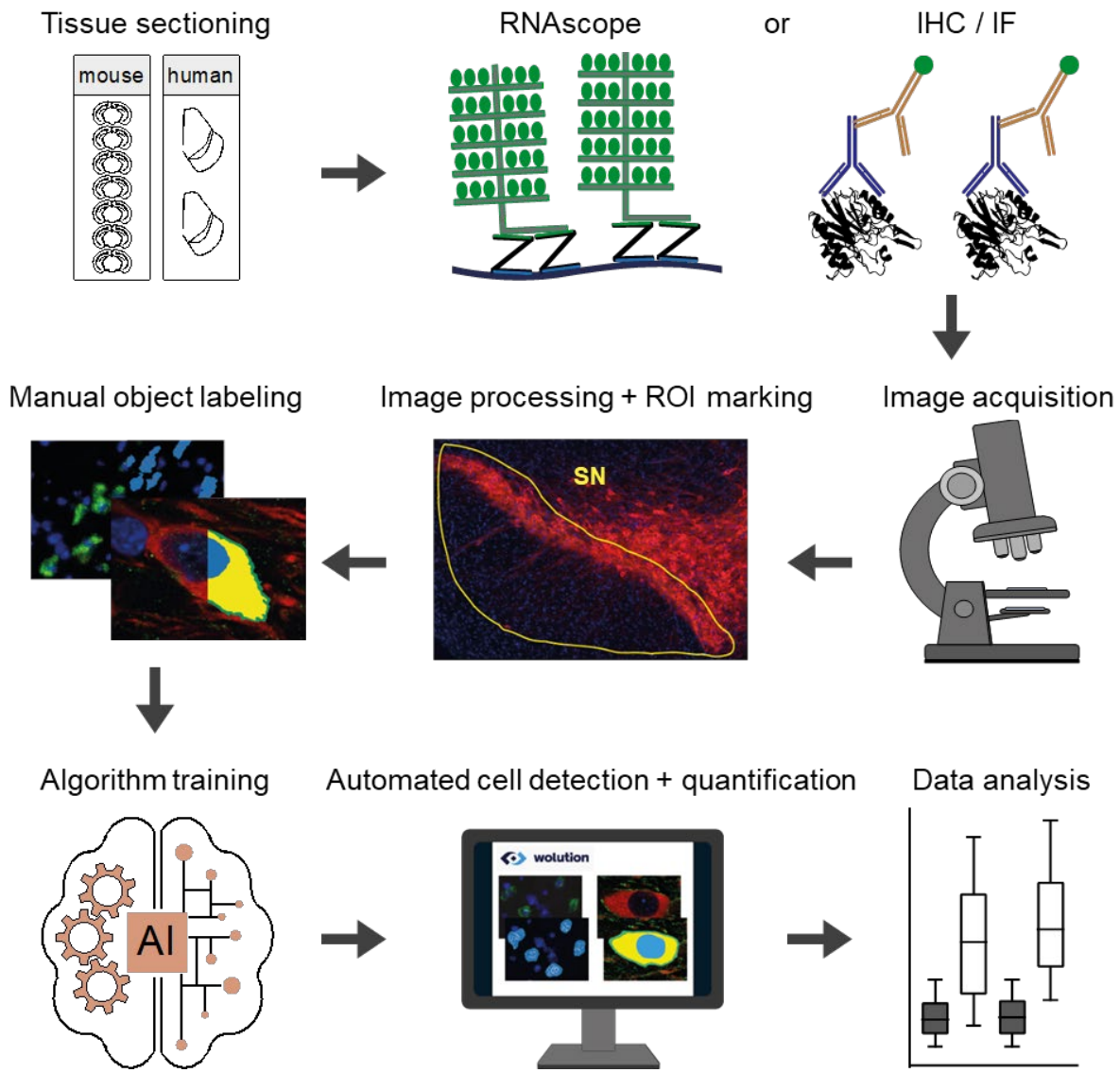

Figure 1: Graphic illustration of deep learning-based image analysis platform (DLAP). After sectioning of murine/human midbrain samples either mRNA- (RNAscope) or protein- (IHC/IF) staining is performed. According to image acquisition, acquired images are preprocessed and the ROIs (e.g. SN) are manually marked. Distinct cell types and compartments (e.g. plasma membrane, nucleus) are manually labeled in a training data set to generate the ground truth data that is then used to train the individual networks. After successful training, images are automatically analyzed.

Results

Based on the Wolution web-interfaces (https://wolution.ai/), we developed a deep learning-based automated image analysis platform (DLAP) as well as six tailored algorithms (two based on FCN, four based on DL3) for fast and reliable identification and quantitative analysis of TH-positive midbrain neurons within the SN and VTA of mouse and human *post mortem* brain sections. These six DLAP algorithms were trained by hundreds of manually marked TH- and DAPI-positive cell bodies of midbrain neurons. **Figure 1** illustrates the general workflow.

145 **Table 1, 2 and S1** provide details of algorithms, trainings, and performances (further details in
146 methods and supplement). For all approaches, the region of interest (ROI) for cell type
147 identification and quantification (i.e the SN) was marked manually, according to anatomical
148 landmarks (Paxinos & Keith B. J. Franklin, 2007). All six algorithms allowed reliable
149 identification of target cells, as well as their quantification in a given ROI (DLAP-3 & 4), and/or
150 quantification of mRNA-derived (DLAP-1 &-2) or protein-derived (DLAP-5 & 6) fluorescence
151 signals of distinct genes of interest in these target cells – all common tasks in life science.

152

153 **Table 1: Quality evaluation parameters for all six algorithms.** Performances were
154 determined by comparing DLAP analysis results of the test image sets to ground truth data
155 (provided by manual labeling). Class name defines the identified molecular or cellular
156 structures. The following quality measures were assessed separately for each class: pixel error
157 rate, rate for true positive (TP), true negative (TN), false positive (FP), false negative (FN)
158 detection, as well as relative specificity (spec.) [defined as TN/(TN+FP)], and sensitivity (sens.)
159 [defined as TP/(TP+FN)].

160

DLAP algorithm	class name	Error [%]	TP [%]	TN [%]	FP [%]	FN [%]	Spec [%]	Sens [%]
1	cell body	5.08	10.3	84.7	4.1	0.8	95.3	92.7
	mRNA		0.3	98.9	0.7	0.0	99.3	92.5
2 (human)	cell body	4.13	5.2	91.0	2.5	1.4	97.3	80.8
	mRNA		0.2	98.9	0.9	0.0	99.1	94.7
3	nucleus	0.61	0.5	98.9	0.5	0.1	99.5	85.5
4	nucleus	0.26	0.1	99.7	0.2	0.0	99.8	59.8
5	nucleus	3.3	0.9	98.5	0.3	0.3	99.7	74.5
	cytoplasm		4.1	92.9	2.2	0.8	97.7	83.7
6	nucleus	5.49	3.0	93.5	2.5	1.0	97.4	75.6
	cytoplasm		9.7	89.0	0.8	0.5	99.1	95.0
	membrane		11.7	85.2	2.2	0.9	97.5	92.4

161

Table 2: Overview of six individual DLAP algorithms and workflow, optimized for distinct image sets and analysis tasks. For detailed description, see methods. Abbreviations: BF brightfield, DAB diaminobenzidine, DAPI 4′,6-diamidino-2-phenylindole, FCN fully convolutional neural network, HE hematoxylin, IF immunofluorescence, NM neuromelanin, RGB red-green-blue, TH tyrosine hydroxylase. * For training, only the cellular nuclei were marked, not the full cell-body, similar as in stereology; only clearly visible, full nuclei were counted.

DLAP algorithm	Trained by / optimized for	Algorithm task	Network-Type	Training-set		post training image analysis optimization (a-e)
				images	cells	
1	RNAscope fluorescence: TH-mouse (DAPI)	1) Algorithm identifies cells of interest and delineates the shape of cell bodies by TH-derived fluorescence signals (green channel). 2) Within these marked cell bodies, target gene derived individual fluorescent dots (red channel) are detected, marked, and counted.	FCN	100	~1000	(a) watershed algorithm for improved separation of mRNA molecules. (b) morphological operations (type dilation and erosion) applied, for better separation of neurons.
2 modification of algorithm 1	RNAscope fluorescence: TH-human (DAPI)	3) A fourth BF channel was included, as a measure for NM-content. After Step (1) and (2) from algorithm 1, in an additional step, the BF signal intensity is quantified within the marked cell bodies.	FCN*	200	~500*	(a) watershed algorithm for improved separation of mRNA molecules. (b) morphological operations (type dilation & erosion) applied, for better separation of neurons.
3	DAB-labelling: TH-mouse	Algorithm identifies and counts nuclei of DAB-positive cells (TH-stained).	DeepLab3*	100	~3000*	none
4 modification of algorithm 3	DAB-labelling: TH-mouse & HE-counterstain	Algorithm extends the automated counting of DAB-positive cells (TH-stained) to sections that are counterstained by HE.	DeepLab3*	300	~2500*	(a) watershed algorithm for improved separation of individual nuclei. (c) filling holes within recognized compartments.
5	IF-labelling: TH-mouse, DAPI DAT-mouse	1) Algorithm identifies and counts cells of interest (i.e TH-positive cells). It delineates the shape of the cell body by immunofluorescence signals for TH (red channel) and nucleus by DAPI fluorescence signal (blue channel). 2) Within these marked compartments, the relative signal intensities are quantified for all three fluorescent channels.	DeepLab3	95	~500	(a) watershed algorithm for improved separation of neurons. (c) filling holes within recognized compartments. (d) removing target gene channel during cell identification. (e) RGB intensity threshold for background-signal determination.
6	IF-labelling: TH-mouse, Kv4.3-mouse, DAPI	1) Algorithm identifies cells of interest and delineates the shape of the cell body by immunofluorescence signals for TH (red channel), of the nucleus by DAPI fluorescence signal (blue channel), and of the membrane (originally learned by Kv4.3 staining, after training no membrane marker needed). 2) Within these marked compartments, the relative signal intensities are quantified for all three fluorescent channels.	DeepLab3	94	~110	(c) filling holes within recognized compartments. (d) removing target gene channel during cell identification. (e) RGB intensity threshold for background-signal determination.

167 Deep learning networks for image segmentation of complicated scenes, such as the Pascal
168 Visual Object Classes (VOC) data set (Everingham et al., 2015), that we used in the DeepLab3
169 based algorithms, are usually very large, and their filters are particularly trained to learn
170 abstract concepts such as “tree” or “car”. Particularly, for the analysis of simple, RNAscope
171 derived fluorescence signals (i.e. individual small dots, Ø ~ 0.3 µm), we found that such a
172 complicated pre-trained neural network was not of benefit. RNAscope derived fluorescence
173 signals are mainly small dots (Ø ~ 0.3 µm), within the somata, which makes threshold based
174 automatic recognition/segmentation of the cell body difficult. Thus, we custom-designed and
175 optimized two less complex FCN-based algorithms (DLAP-1 and 2), and we demonstrate that
176 they were better suited for the analysis of RNAscope data, compared to DeepLab3
177 approaches. The latter algorithm failed to recognize the small dots (mRNA molecules) as
178 evident from the sensitivity-value of 0.0% for this class, compared to 92.5% and 94.7% for the
179 FCN-based algorithm (**Table S1**). For protein-derived immunohistochemistry signals
180 (diaminobenzidine, DAB and immunofluorescence IF), tailored DeepLab3 algorithms gave
181 better allover-results as indicated by lower overall error (**Table S1**; DLAP-3 to -6).

182

183 **DLAP based automated quantification of mRNA molecules in individual target cells via**
184 **RNAscope approaches.**

185 RNAscope *in situ* hybridization allows absolute quantification of distinct mRNA molecules,
186 without cDNA synthesis, via hybridization-probes, with each fluorescence dot representing one
187 target mRNA-molecule (Jolly et al., 2019; F. Wang et al., 2012). Due to multiple probes for
188 each target-gene, it is hardly affected by degraded RNA. We have used RNAscope for
189 determining mRNA molecule numbers in individual TH-positive SN DA neurons in fresh-frozen,
190 PFA-postfixed mouse midbrain sections (Benkert et al., 2019). For automated quantification of
191 numbers of RNAscope probe derived fluorescence dots, two custom designed FCN based
192 algorithms were used (DLAP-1 & 2). The general principle of the FCN algorithms is given in
193 **Figure 2**. DLAP analysis of RNAscope signals was performed in two steps: in a first step, the
194 cell body was recognized and marked according to the TH-signals, and in a second step,
195 individual target gene mRNA dots (labelled with a different fluorophore) were identified and
196 counted within the marked TH-positive cell body, including the nucleus. DLAP-1 is optimized
197 for detecting TH-positive DA neurons from mice, DLAP-2 for detecting human TH-positive DA
198 neurons, containing neuromelanin (NM), a dark pigment present in DA neurons from humans
199 and primates (Bazelon, Fenichel, & Randall, 1967; Vila, 2019), visible only in bright field (BF).

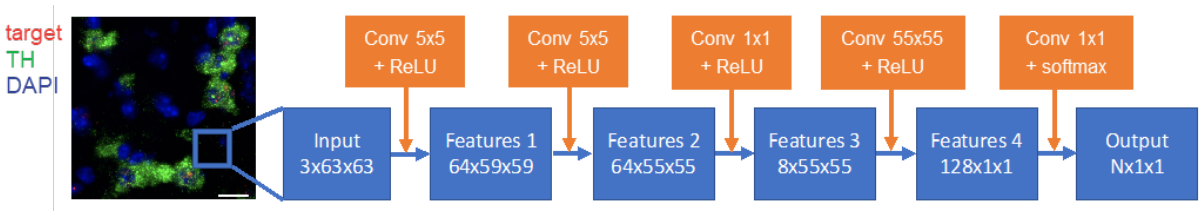

Figure 2: Architecture of the fully convolutional neural network (FCN), used for RNAscope DLAP. The input image on the left shows SN DA neurons RNAscope-labelled for tyrosine hydroxylase (TH) mRNA (green), target mRNA (red) and DAPI (blue); Scale bar: 20 µm. The image is passed through five convolutional layers that are connected by the Rectified Linear Units (ReLU) activation function. The last activation function is the softmax function, which normalized the network output to the probability distribution. The size of the convolutional kernels is specified in the orange boxes. The blue boxes provide the dimensions of the resulting feature maps. The network analyzes image patches of size 63^2 pixels to determine the class of the central pixel in the patch which is applied convolutionally to every central pixel in the image, so that the final output image has the same dimensions as the input image.

Figure 3a shows a typical image of TH-positive SN neurons in a coronal mouse brain section, after RNAscope *in situ* hybridization, before (input image, left) and after automated identification of TH-positive cell bodies and quantification of individual fluorescence dots, derived from target mRNA molecules. Cell bodies were identified and marked according to the TH-derived fluorescence signal (green), and target mRNA were identified as probe-derived fluorescence-signals (red dots, **Table S2**). Results for two different target genes - with lower (Cav1.3) and higher (Cav2.3) mRNA abundance - are given (**Figure 3b, Table S3, S4**). Both target genes code for a specific voltage gated Ca^{2+} channel α-subunit that has been linked to Parkinson's disease (Benkert et al., 2019; Birgit Liss & Surmeier, 2022; Ortner, 2021). The manual and the automated analysis (DLAP-1) resulted in very similar results for both genes, over the full range of mRNA molecule numbers (Cav1.3 manual: 24±1 mRNA molecules, DLAP-1 24±1, N=3, n=499 neurons analysed, p=0.999, R^2=0.92; Cav2.3 manual: 69±5, DLAP-1: 69±5; N=3, n=372; p=0.999, R^2=0.92; **Figure 3b/c, S1, Table S3, S4**). Accordingly, the significant, ~3-fold higher number of Cav2.3 mRNA molecules in mouse SN DA neurons, compared to those of Cav1.3 is robustly detected with manual and with DLAP-1 analysis ($p<0.0001$ for both), similar as previously described (Benkert et al., 2019).

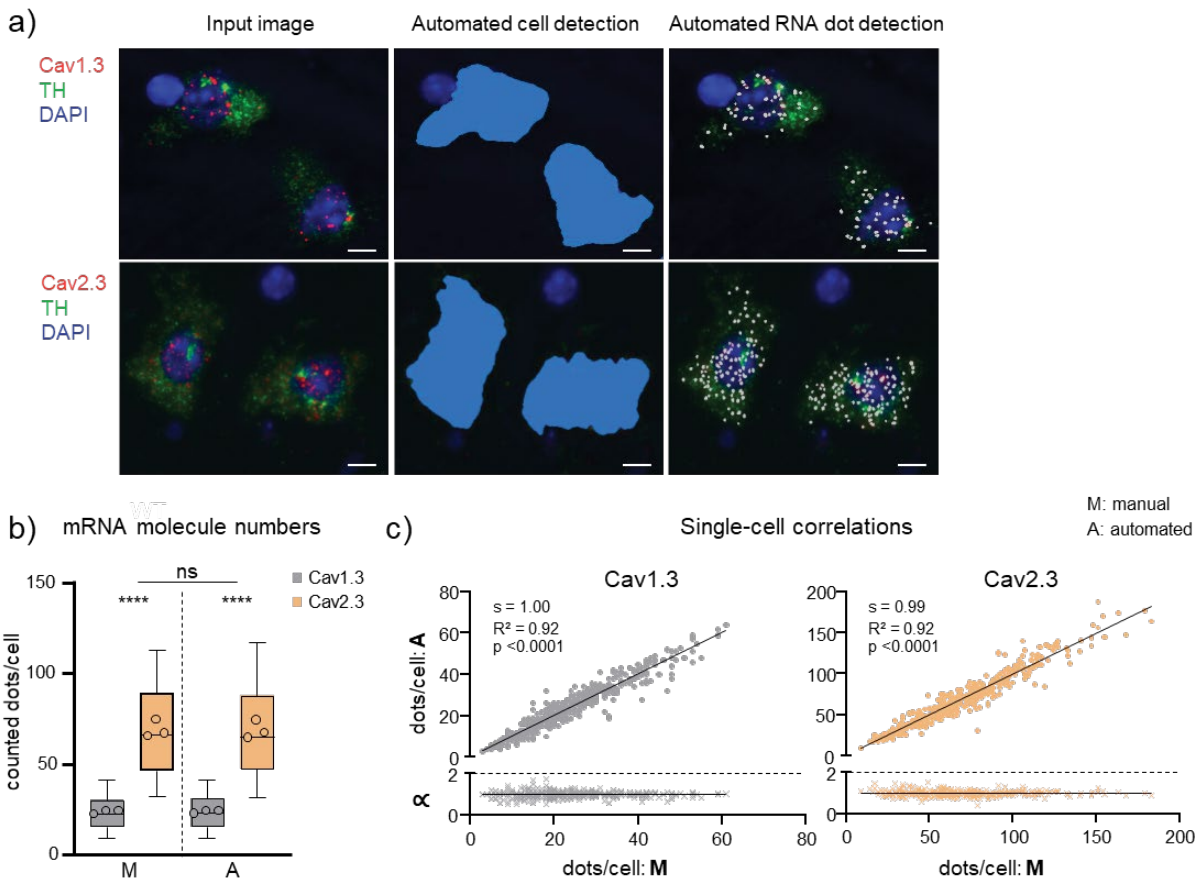

Figure 3: Comparison between manual and automated RNAscope-derived image analysis of mouse midbrain sections. a) SN DA neurons in coronal midbrain section from adult mice after RNAscope for tyrosine hydroxylase (TH, green) and Cav1.3 or Cav2.3 Ca^{2+} channels (red). Nuclei are marked by DAPI-staining (blue). Left: input images, middle and right: images after automated recognition of the TH labelled cell bodies (middle, blue area) and of target mRNA molecules (right, white dots) with DLAP-1. Scale bars: 5 µm. b) mRNA molecule numbers/SN DA neuron, counted manually (M) or automatically (A) via DLAP-1, as indicated. Data are given as boxplots (median, 10-90 percentile) for all analysed neurons (Cav1.3: n = 449, Cav2.3: n = 372). The open circles indicate mean values for each analysed animal (N = 3 each). Significant differences (for analysed neurons) according to two-way ANOVA with Tukey's multiple comparison tests are indicated by asterisks (****: $p < 0.0001$, ns: $p > 0.05$). c) Upper: Single neuron correlations of mRNA-derived dot counts/cell between manual and automated analysis according to Pearson correlation test. Lower: corresponding proportionality constants ∝, calculated from the manual and automated dot count ratios. All data are detailed in Supplementary Table S3/4 and Supplementary Figure S1.

Similar robust results were obtained for RNAscope analysis of human SN DA neurons with the DLAP-2 algorithm. To optimize DLAP for human SN DA neurons, the D-LAP1 algorithm was extended to quantify the brightfield (BF) intensity, as a measure for the variable NM content of human SN DA neurons, to evaluate possible confounding effects of different NM content on RNAscope results (**Figure 4, S2, Table 2**). Cav1.3 mRNA molecules as well as NM content were compared in SN DA neurons from adult and aged individuals (adult: 42±7 years; aged:

252 78±3, details in **Table S5**). Manual and automated DLAP-2 analysis provided very similar
253 results, and we detected a strong linear correlation between manually and automatically
254 determined mRNA molecule numbers as well as NM-content (**Figure 4b/d/e, Table S6, S7)**.
255 Interestingly, the number of Cav1.3 mRNA molecules was significantly lower (~60%) in SN DA
256 neurons from aged individuals (**Figure 4b left**, manual: adult 38±5, aged 14±3; N=3, n=223;
257 p<0.001; DLAP-2: adult 40±7, aged 17±4; N=3, n=258; p<0.001).

258 Noteworthy, the BF-value derived NM content was also significantly different between adult
259 and aged samples, with ~30% higher NM content in aged SN DA neurons (p<0.0001, **Figure**
260 **4b right**, **Table S6, S7**). To exclude that the lower number of mRNA molecules determined in
261 aged SN DA neurons were artificially caused by the higher BF values (as measure for NM
262 content), we addressed possible confounding parameters by applying a mixed effects model
263 that we had optimized for these kind of human sample-derived data that are in general more
264 heterogeneous (J. Duda, Fauler, Grundemann, & Liss, 2018; Schlaudraff et al., 2014). As the
265 model indicated that the NM content indeed affected the detected Cav1.3 mRNA molecule
266 numbers we corrected the automated data for the NM-content attributed effect. However, as
267 evident in **Figure 4c, Table S6**, we still detected a similar highly significant lower number of
268 Cav1.3 mRNA molecules (~35%) in SN DA neurons from aged donors.

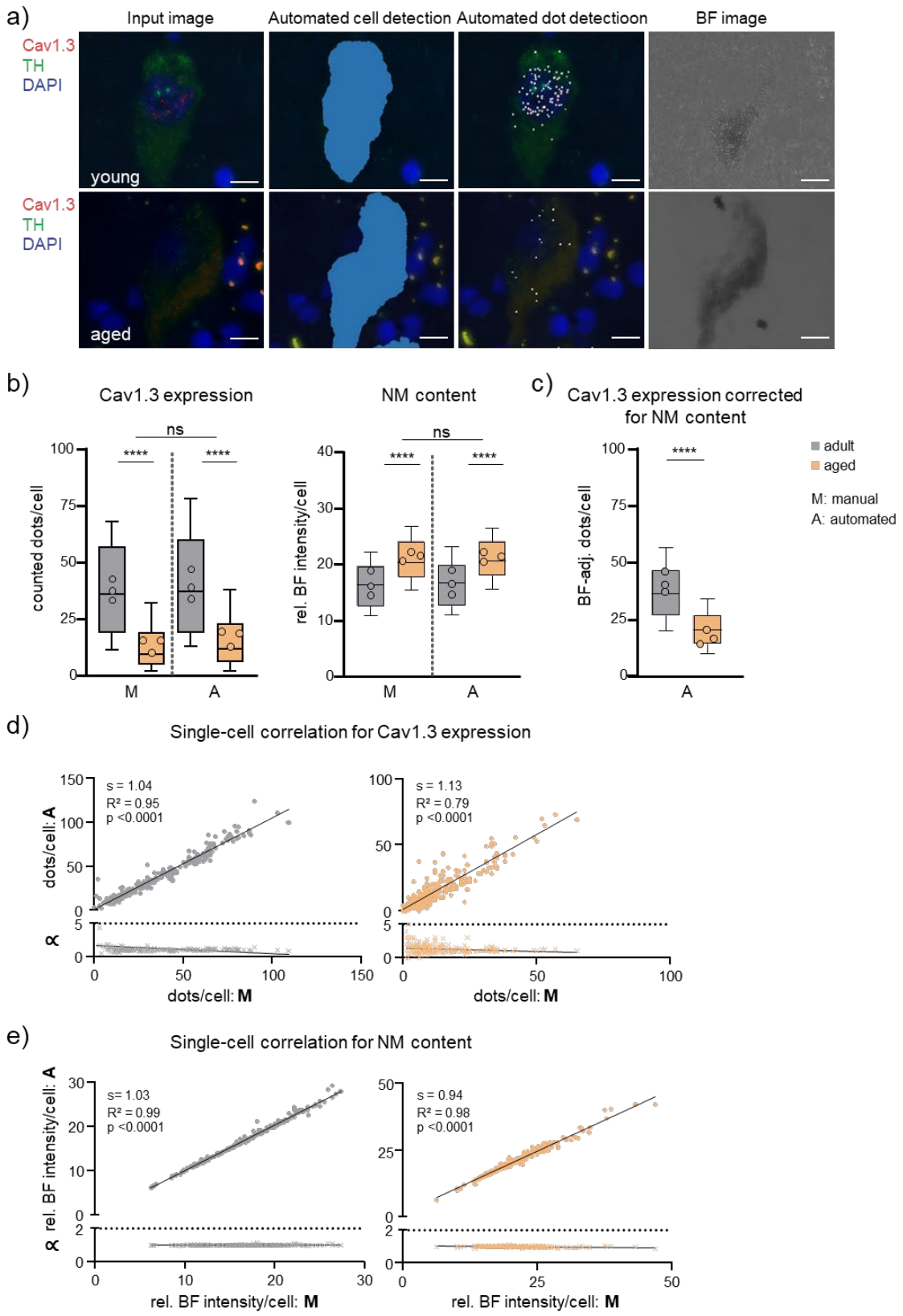

Figure 4: Comparison between manual and automated RNAscope-derived image analysis of human midbrain sections. a) SN DA neurons in coronal midbrain section from human adult and aged post mortem brain samples after RNAscope for tyrosine hydroxylase (TH, green) and Cav1.3 Ca^{2+} channels (red). Nuclei are marked by DAPI-staining (blue). Left: input images, middle: images after automated recognition of the TH labelled cell bodies (middle

275 left, blue area) and of target mRNA molecules (middle right, white dots) with DLAP-2. Right:
276 corresponding brightfield (BF) images used to quantify neuromelanin (NM) content. Relative
277 BF intensity is measured within the delineated cell shapes. Scale bars: 10 µm. b) mRNA
278 molecule numbers/SN DA neuron (left) and NM content (rel. BF signal intensity; right),
279 quantified manually (M) or automatically (A) via DLAP-2, as indicated. Data are given as
280 boxplots (median, 10-90 percentile) for all analysed neuros (adult: n = 223, aged: n = 258).
281 The open circles indicate mean values for each analysed brain sample (N = 3 each). Significant
282 differences (for analysed neurons) according to two-way ANOVA with Tukey's multiple
283 comparison tests are indicated by asterisks (****: $p < 0.0001$, ns: $p > 0.05$). c) mRNA molecule
284 numbers/SN DA neuron, determined via DLAP-2, adjusted for NM using the Linear Mixed
285 Effects Model. Data are given as boxplots (median, 10-90 percentile) for all analysed neurons
286 (adult: n = 206, aged: n = 231). The open circles indicate mean values for each analysed brain
287 sample (N = 3 each). Significant differences (for analysed neurons) according to Mann-
288 Whitney test are indicated by asterisks (****: $p < 0.0001$). d) and e) Upper: Single neuron
289 correlations of Cav1.3 mRNA-derived dot counts/cell (d) and rel. BF signal intensity/cell (e)
290 between manual and automated analysis according to Pearson correlation test. Lower:
291 corresponding proportionality constants ∝, calculated from the manual and automated dot
292 count ratios. All data are detailed in Supplementary Table S5-7 and Supplementary Figure S2.

293

294 **DLAP based automated quantification of immuno-labeled neuron numbers in tissue**
295 **sections.**

296 Determination of numbers of cellular populations in defined ROI is a common task e.g. for
297 quantifying selective cell loss in neurodegenerative diseases, and to assess neuroprotective
298 therapeutic effects (Golub et al., 2015). However, commonly used stereological approaches
299 (still the gold-standard), are time consuming, and they provide only a - more or less exact -
300 estimation of cell numbers, depending on the size of the manually counted fraction of cells
301 (Brown, 2017; West, 1999). Approaches have been developed to increase sampling sizes and
302 thus accuracy of estimates (Mouton et al., 2017). Nevertheless, estimates are prone to over-
303 or underestimating total cell numbers, particularly if the target cells are not homogeneously
304 distributed in the ROI, as it is the case e.g. due to differential neuronal vulnerability in
305 degenerative disease (Baddeley, 2001; Miles & Davy, 1976; Noori & Fornal, 2011). However,
306 manual approaches to count all neurons in a given ROI are extremely time consuming and
307 prone to bias/human error. To overcome these issues, we developed three DLAP algorithms,
308 dramatically reducing the time for valid determination of cell numbers, tailored to detect and
309 count target cells, immuno-labelled by either DAB - without (DLAP-3) or in the presence of a
310 hematoxylin counterstain (DLAP-4) - or by IF (DLAP-5). According to our stereological
311 procedures, the DLAP-3 and 4 algorithms were trained by marking the neuronal nuclei only,
312 not the whole cell-bodies, and we also counted only clearly visible nuclei of TH-positive cells.

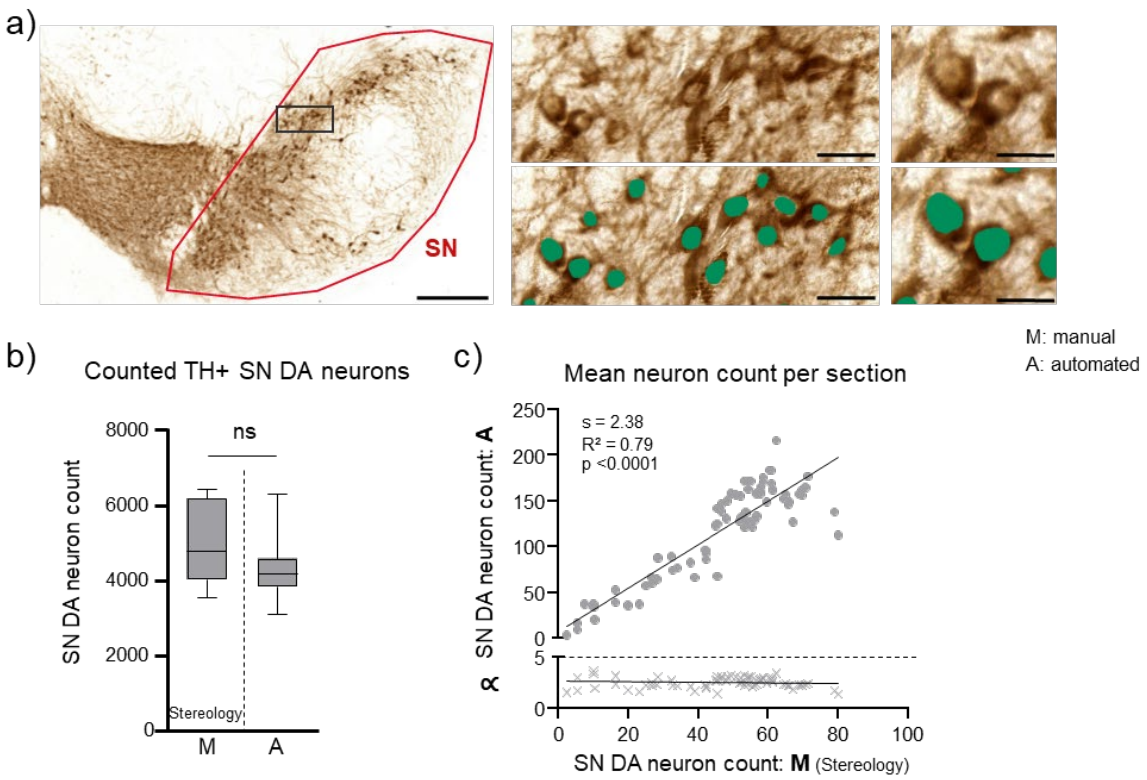

Figure 5: Comparison between unbiased stereology and automated IHC-derived image analysis of juvenile mouse midbrain sections. a) SN DA neurons in coronal midbrain section from juvenile mice after DAB-IHC for tyrosine hydroxylase (TH, brown). Left. input image where total SN is delineated in red. Scale bar: 200 µm. Middle and right: enlarged images before (upper) and after (lower) automated recognition of the nuclei within TH labelled cell bodies (green area) with DLAP-3. Scale bars: 50 µm (middle) and 10 µm (right). b) SN DA neurons/mouse quantified via unbiased stereology (extrapolated via the optical fractionator method, M) or automatically (A) via DLAP-3, as indicated. Data are given as boxplots (median, 10-90 percentile) for all analysed mice (N = 10). Significant differences according to Mann-Whitney test are indicated by asterisks (ns: $p > 0.05$). c) Upper: correlations of SN DA neuron counts/section between unbiased stereology and automated analysis according to Pearson correlation test. Lower: corresponding proportionality constants ∝, calculated from the manual and automated cell count ratios. All data are detailed in Supplementary Table S8/11 and Supplementary Figure S3.

DAB-labelling is more commonly used for determining cell-numbers in histological samples, as stained sections can be archived and e.g. (re-) analyzed. **Figure 5, S3, Table S8, S11** summarize the results for count of TH-positive SN neurons (unilaterally) from juvenile mice after DAB immunostaining, comparing stereological estimates with automated counting, utilizing DLAP-3. The stereological estimates and automated neuron counts resulted in very similar neuron numbers (Stereology: 4951±1079, DLAP-3: 4317±912 neurons unilaterally; $p=0.218$, N=10. linear correlation/section: $R^2=0.79$). These SN DA neuron numbers correspond well to the literature for C57bl/6 mice, ranging from 4000-6000 neurons unilaterally (Brichta & Greengard, 2014; Nelson, Liang, Sinton, & German, 1996).

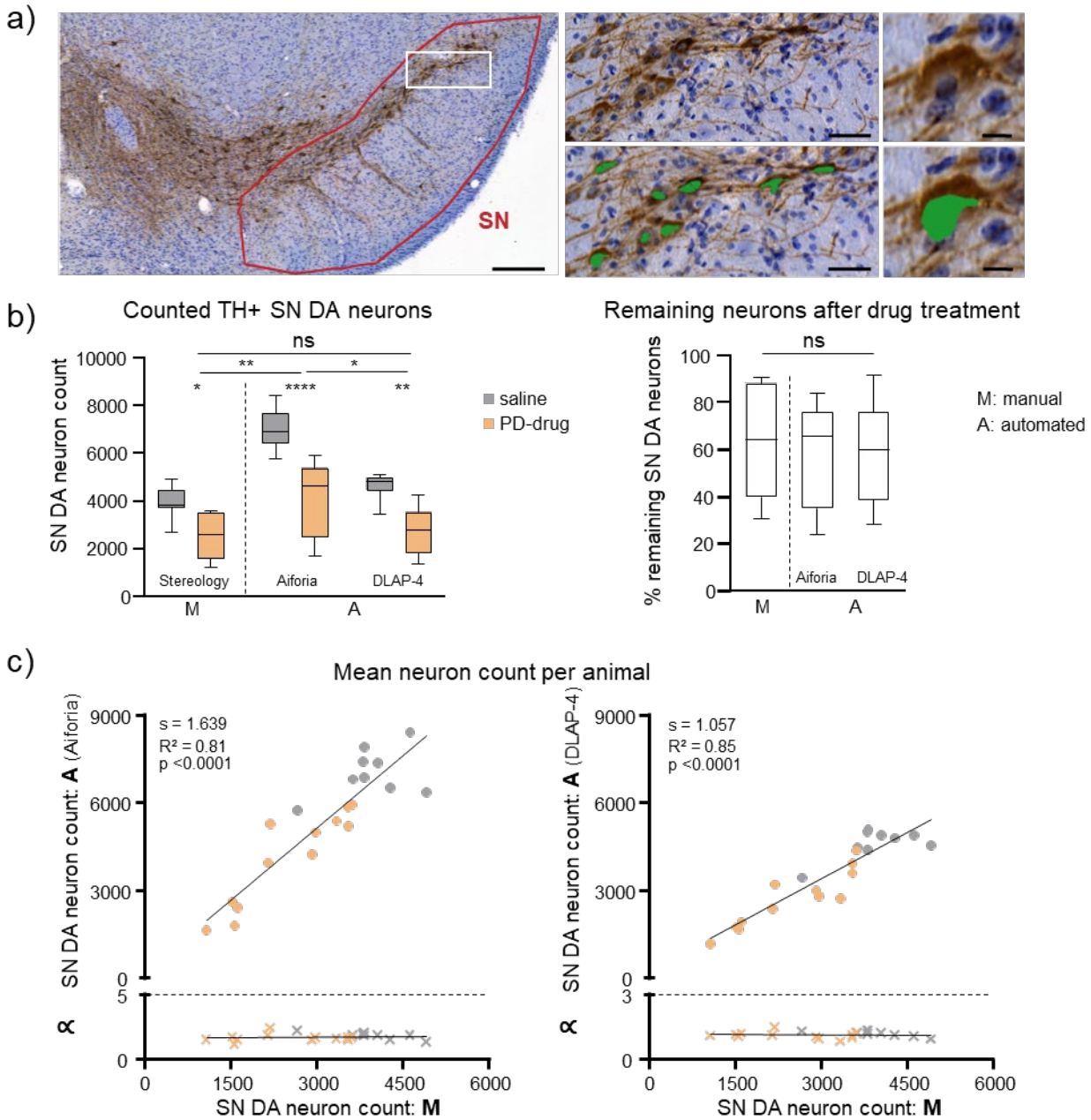

Figure 6: Comparison between unbiased stereology and automated IHC-derived image analysis of adult mouse midbrain sections. a) SN DA neurons in coronal midbrain section from adult mice after DAB-IHC for tyrosine hydroxylase (TH, brown). Nuclei are marked by hematoxylin-staining (blue). Left. input image where total SN is delineated in red. Scale bar: 200 µm. Middle and right: enlarged images before (upper) and after (lower) automated recognition of the nuclei within TH labelled cell bodies (green area) with DLAP-4. Scale bars: 50 µm (middle) and 10 µm (right). b) Left: SN DA neurons/mouse quantified via unbiased stereology (extrapolated via the optical fractionator method, M) or automatically (A) via an algorithm provided by Aiforia or DLAP-4, as indicated. Right: remaining TH-positive neurons [%] in drug-treated mice calculated relative to the mean of the saline-treated group. Data are given as boxplots (median, 10-90 percentile) for all analysed mice (saline: N = 9; PD-drug: N = 12). Significant differences according to two-way ANOVA with Tukey's (absolute counts) or Kruskal-Wallis with Dunn's multiple comparison test (percentage of remaining neurons) are indicated by asterisks (ns: $p > 0.05$, *: $p < 0.05$, **: $p < 0.01$, ****: $p < 0.0001$). c) Upper: correlations of SN DA neuron counts/animal between unbiased stereology and automated

354 analysis (left: Aiforia, right: DLAP-4) according to Pearson correlation test. Lower:
355 corresponding proportionality constants ∝, calculated from the manual and automated cell
356 count ratios. Stereology data and Aiforia data modified from Benkert et al. (2019). All data are
357 detailed in Supplementary Table S9-11 and Supplementary Figure S4.

358

359 Immunohistochemistry sections are often counterstained with an unspecific cellular marker
360 (like Nissl, hematoxylin). For analysis of SN DA neurons, such counterstains are often
361 performed to confirm that a loss of TH-immunopositive neurons (e.g. in a PD-model) indeed
362 corresponds to a loss of the respective neurons, and does not reflect a mere downregulation
363 of TH-expression (Alam, Edler, Burchfield, & Richardson, 2017; Healy-Stoffel, Ahmad,
364 Stanford, & Levant, 2012; Rausch, Wang, & Radad, 2022). As we use hematoxylin-
365 counterstains in such experiments (Benkert et al., 2019; B. Liss et al., 2005), we optimized
366 DLAP-4 to detect DAB stained TH-positive SN neurons in such counterstained sections. With
367 DLAP-4, we re-analysed a cohort of 21 mice that we had already analysed (Benkert et al.,
368 2019) to quantify the effect of a PD drug (1-Methyl-4-phenyl-1,2,3,6-tetrahydropyridin, MPTP)
369 that induces preferential loss of SN DA neurons. Adult C57bl/6J mice were either injected with
370 saline (N=9) or with MPTP/probenecide (N=12). We compared DLAP-4 derived data with the
371 respective already published stereology-derived data, and also with another automated neuron
372 count approach, based on the Aiforia platform (**Figure 6, S4, Table S9-11)**. We had used the
373 Aiforia platform (https://www.aiforia.com) for this cohort, to confirm relative numbers of
374 remaining SN DA neurons after drug-treatment. Indeed, the relative determined cell loss by
375 the Aiforia approach was similar to that estimated by stereology (~40%, p=0.183; **Figure 6b,**
376 **Table S10,** and Benkert et al. (2019)). However, the absolute number of neurons determined
377 with the Aiforia approach was almost double as high (saline: stereology 3959±643, Aiforia
378 7048±843, p<0.0001, drug: stereology 2504±933, Aiforia 4108±1596, p=0.004; **Figure 6b, S4,**
379 **Table S9**). This overcount, and the fact that the convolutional neuronal network (CNN)-based
380 Aiforia system does not allow algorithm training by the users (Penttinen et al., 2018), let us
381 switch to the Wolution-platform in the first instance.

382 With the DLAP-4 approach, a similar relative % of remaining TH-positive SN neurons in the
383 drug-treated mouse cohort was detected, as with stereology or Aiforia (DLAP-4: 59±21%,
384 stereology: 63±59%, p=0.234; Aiforia: 58±23%, p=0.988). Moreover, also the absolute
385 numbers of SN DA neurons/mouse, counted by DLAP-4 were similar to the respective
386 stereological estimates (Saline: DLAP-4 4614±500, stereology 3959±643, p=0.744; Aiforia
387 7048±823, p<0.0001. Drug: DLAP-4 2708±975; stereology: 2504±922, p=0.996; Aiforia
388 4108±1596, p=0.016). The linear correlation coefficients between mean manually and
389 automatically counted neuron numbers were similarly high for both automated approaches.
390 However, the linear regression slope, was higher for the Aiforia algorithm compared to our

391 DLAP-4 algorithm (1.6 vs 1.0), in line with the higher, over-counted neuron-number by the
392 Aiforia approach (**Figure 6, Table S11**).

393 DLAP-5 analysis of immunofluorescence labelled cells defines a novel 394 population of DAT-negative neurons in the lateral SN.

395 We extended our automated cell quantification approach from DAB/BF to cells labelled by
396 immunofluorescence (IF). IF has a greater dynamic signal range (Hofman, 2002; Peck et al.,
397 2016), and allows the parallel quantification of more than one cell-population, defined by
398 distinct markers (Katikireddy & O'Sullivan, 2011). Moreover, it can provide additional
399 information regarding protein localization and relative expression levels.

400 We trained DLAP-5, based on TH and DAPI signals only, to detect and count
401 immunofluorescence TH-positive SN DA neurons in DAPI co-stained sections, and to mark the
402 neuronal cell-body and the nucleus of TH-positive neurons. After identification of TH-positive
403 cell-bodies, in a next step, DLAP-5 quantifies IF-intensities separately in both identified
404 compartments for up to three distinct fluorescent channels, enabling co-expression analyses.
405 **Figure 7a** illustrates the automated identification of TH IF-positive SN neurons (red) in a
406 coronal mouse midbrain section.

407 As the expression of the dopamine transporter DAT is commonly used as an additional maker
408 for SN DA neurons besides TH, we used DLAP-5 to quantify the relative DAT-IF signals in the
409 marked TH-positive cell bodies. Our central aim here was to quantify the co-expression of TH
410 and DAT in SN neurons, and their relative expression levels, rather than determining absolute
411 numbers of TH-positive SN neurons (**Figure 7, S5, S6)**. Thus, we only included those TH-
412 positive SN neurons into further quantitative DAT analysis that were clearly
413 separated/segmented, with marked cell-bodies of proper size and clearly visible full nuclei. Our
414 exclusion criteria are specified in methods and in **Figure S5a,** and resulted in manual exclusion
415 of ~28±4% of the automatically identified TH-positive SN neurons (**Figure S5b, Table S12**). In
416 the remaining number of TH-positive SN neurons (3015±374 neurons/mouse, N=7), we
417 detected only in ~95% a DAT-IF signal above the background signal (2880±340
418 neurons/mouse, p=0.0156). The remaining ~5% (4.6±1.4%) of TH-positive SN neurons were
419 negative for DAT (**Figure 7b, S5c, Table S12, S13)**.

420 In order to further characterize this small subpopulation of SN neurons, we used the x,y-
421 coordinates of the analyzed TH-positive neurons (automatically provided by the algorithm) to
422 generate 2D anatomical maps for each analyzed mouse and coronal section and merged maps
423 for all mice. These maps revealed that the TH-positive DAT-negative neurons were clustered
424 in the very lateral parts of the SN (**Figure 7c, S5, S6)**. This excludes that these DAT-negative
425 TH-positive neuron population was a contamination by VTA DA neurons, overlapping with the
426 medial SN. Interestingly, the DAT-negative TH-positive neurons were significantly enriched in

427 the caudal parts of the lateral SN, as their relative amount of was about 6-fold higher compared
428 to those in the rostral parts of the lateral SN (7.4±2.4% vs 1.2±0.6%, p=0.03; **Figure S5d,**
429 **Table S12**). Moreover, the DAT-negative SN neurons were about 35% smaller compared to
430 the DAT-positive neurons (according to x,y-coordinates: DAT positive: 214±13 µm², DAT
431 negative: 142±13 µm², p=0.006, **Figure S5e, Table S14**).

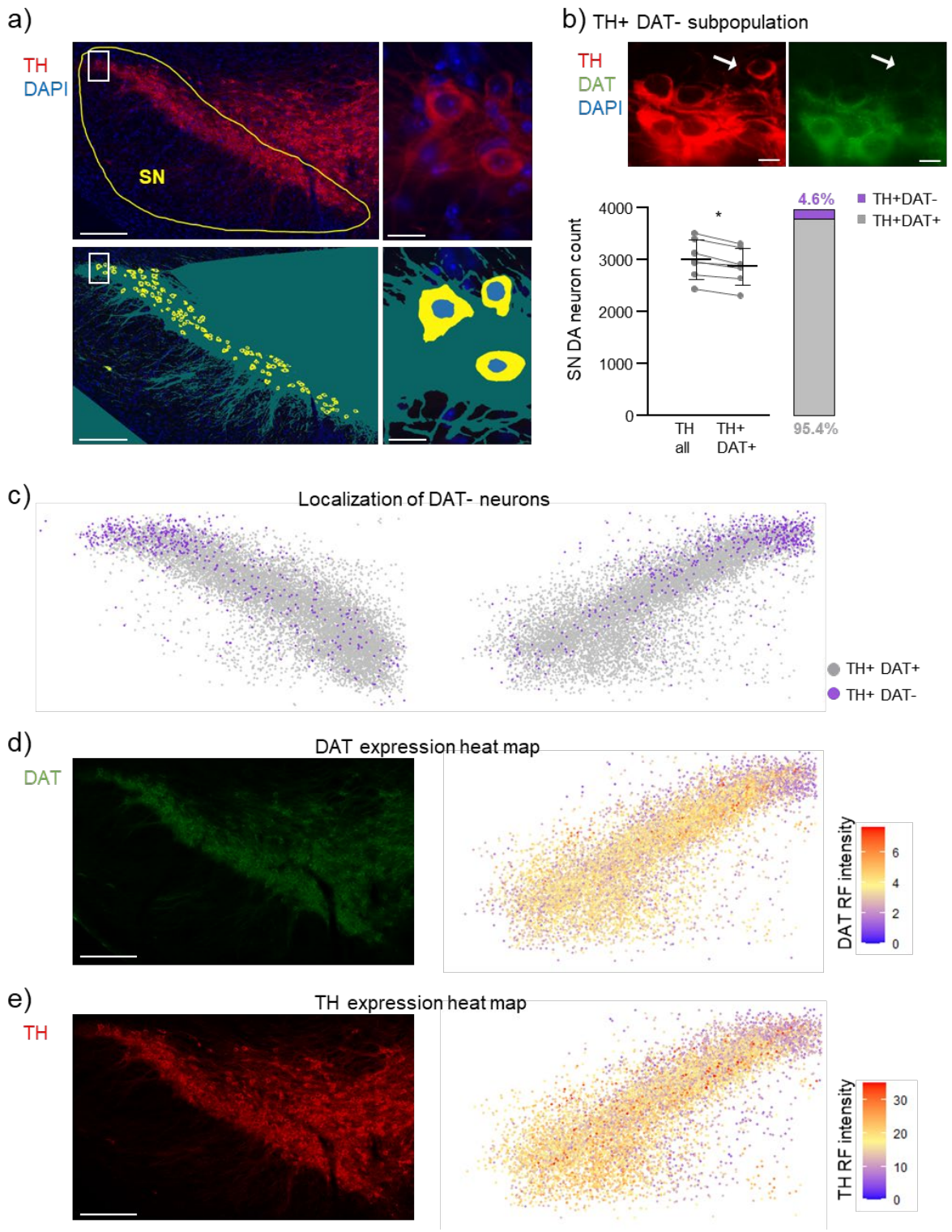

Figure 7: Automated IF-derived image analysis of mouse midbrain sections. a) Top: SN DA neurons in coronal midbrain section from adult mice after IF for tyrosine hydroxylase (TH, red). Nuclei are marked by DAPI-staining (blue) and the SN region is delineated in yellow. Bottom: output image after automated recognition of TH labelled cell bodies (yellow area) and corresponding nuclei (blue area) with DLAP-5. Scale bars: 200 µm (left) and 20 µm (right). b) Top: enlarged input image separated for TH fluorescence (red, left) and DAT fluorescence (green, right). Scale bars: 10 µm. The white arrow indicates a TH positive, DAT negative SN DA neuron. Bottom left: SN DA neurons/mouse quantified via DLAP-5. Shown are the total number of analyzed TH+ neurons and number of TH+ DAT+ neurons. Data are given as

442 scatterplots (mean, SD) for all analysed mice (N = 7). Significant differences according to
443 Wilcoxon test are indicated by asterisks (*: $p < 0.05$). Bottom right: Vertically sliced bar giving
444 the percentage of TH+DAT+ and TH+DAT- neurons. c) Anatomical map showing the
445 distribution of TH+DAT+ and TH+DAT- neurons within the whole SN region. Given are the
446 individual neurons for all analyzed animals (n = 21106, N = 7). e/f) Heat-map showing DAT (d)
447 and TH (e) relative fluorescence (RF) intensity gradient for each neuron within the whole SN
448 region. Given are the individual neurons for all analyzed animals (n = 21106, N = 7). All data
449 are detailed in Supplementary Table S12-14 and Supplementary Figure S5/S6.

450

451 For subpopulations of VTA DA neurons, DAT-expression gradients have been described (Fu
452 et al., 2012; S. Lammel et al., 2008; Li, Qi, Yamaguchi, Wang, & Morales, 2013; Morales &
453 Margolis, 2017), and a lower DAT/TH ratio for lateral SN DA neurons has been briefly
454 discussed (Fu et al., 2012). To systematically address whether a gradient in DAT expression
455 is present within the SN, we used the relative, non-saturated fluorescence signal intensities
456 (RF) of each DAT-analyzed TH IF-positive neuron, determined by DLAP-5, and the respective
457 x,y-coordinates to generate heat-maps (**Figure 7d**). Those maps indicated a medio-lateral
458 DAT-protein gradient, with lowest DAT-immunosignals, within those of the background in the
459 very lateral SN. Corresponding heat-maps for TH suggested a similar, but less prominent
460 gradient (**Figure 7e**), similar as in (Blanchard et al., 1994; Fu et al., 2012). To our knowledge,
461 such DAT-gradient and neurons in the very lateral SN that are immune-positive for TH but
462 immuno-negative for DAT have not yet been systematically described. We enabled this by
463 analysing DAT-expression in more than 20,000 SN neurons - hardly possible without the
464 automated DLAP-5 approach. However, this algorithm does not allow conclusions regarding
465 the sub-cellular location of the IF-signal.

466

467 DLAP-6 based relative quantification of immuno-fluorescence derived signals in 468 cellular compartments.

469 As proteins can mediate different functions in dependence of their cellular localization, analysis
470 with higher resolution is desired. To enable relative quantification of immunofluorescence
471 signals in plasma-membranes, cytoplasm and nucleus, we developed the DLAP-6 algorithm,
472 optimized to detect and analyse neurons in high-resolution confocal fluorescent images.

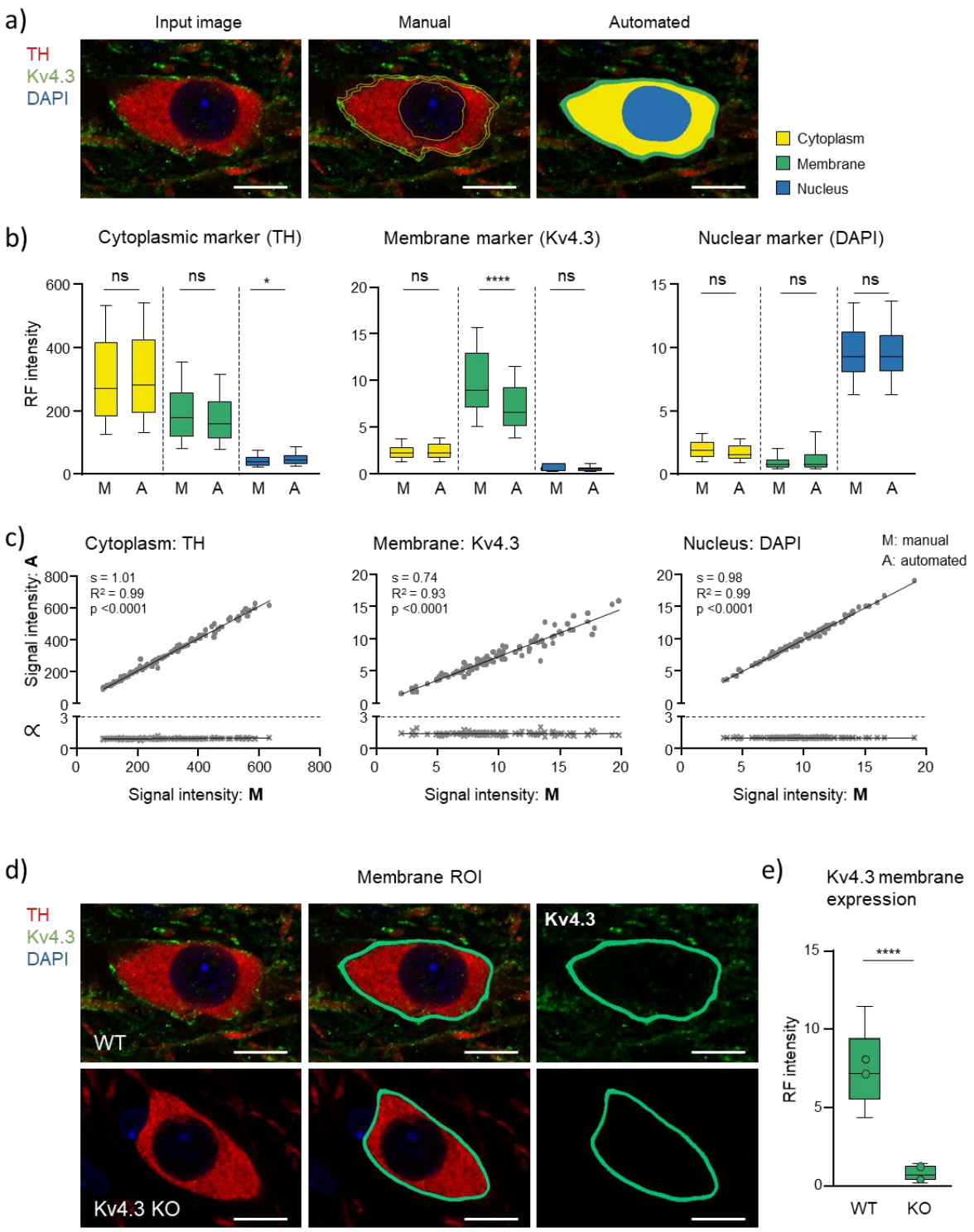

Figure 8: Comparison between manual and automated IF-derived image analysis of mouse midbrain sections. a) SN DA neurons in coronal midbrain section from adult mice after IF for tyrosine hydroxylase (TH, red) and Kv4.3 (green). Nuclei are marked by DAPI-staining (blue). Left: input image, middle: image after manual labeling of cell body, nucleus and membrane, right: image after automated recognition of the TH labelled cell body (yellow area), nucleus (blue area) and membrane (green area) with DLAP-6. Scale bars: 10 µm. b) Relative fluorescence (RF) intensity/SN DA neuron in different sub-cellular compartments, quantified manually (M) or automatically (A) via DLAP-6, as indicated. Data are given as boxplots (median, 10-90 percentile) for all analysed neurons (n = 94). Significant differences according

483 Mann-Whitney test are indicated by asterisks (ns: $p > 0.05$, ****: $p < 0.0001$). c) Upper: Single
484 neuron correlations of RF intensities/cell between manual and automated analysis for all three
485 marker genes in their respective compartment according to Pearson correlation test. Lower:
486 corresponding proportionality constants ∝, calculated from the manual and automated dot
487 count ratios. d) SN DA neurons in coronal midbrain section from adult WT (top) and Kv4.3 KO
488 (bottom) mice after IF for tyrosine hydroxylase (TH, red) and Kv4.3 (green). Nuclei are marked
489 by DAPI-staining (blue). Left: input images, middle and right: images after automated
490 recognition of Kv4.3 labelled plasma membrane with DLAP-6. Scale bars: 10 µm. e) Kv4.3
491 relative fluorescence (RF) intensity/SN DA neuron membrane in WT and Kv4.3 KO mice, as
492 indicated. . Data are given as boxplots (median, 10-90 percentile) for all analysed neurons
493 (WT: n = 179, Kv4.3 KO: n = 200). The open circles indicate mean values for each analysed
494 animal (N = 2 each). Significant differences according to Mann-Whitney test are indicated by
495 asterisks (****: $p < 0.0001$). All data are detailed in Supplementary Table S15-17 and
496 Supplementary Figure S7.

497

498 DLAP-6 was specifically trained by using TH as marker for the cell body/cytoplasm, DAPI as
499 marker for the nucleus, and the ion channel subunit Kv4.3 as marker for the plasma-membrane
500 of SN DA neurons. Kv4.3 is highly expressed in plasma-membranes of SN DA neurons, and it
501 is the pore-forming subunit of voltage and Ca^{2+} sensitive A-type K^+ channels that modulate the
502 activity and the vulnerability of SN DA neurons (Aidi-Knani, Regaya, Amalric, & Mourre, 2015;
503 Dragicevic, Schiemann, & Liss, 2015; Haddjeri-Hopkins et al., 2021; B. Liss et al., 2001;
504 Serôdio & Rudy, 1998; Subramaniam et al., 2014). The Ca^{2+}-sensitivity of Kv4.3 channel
505 complexes is mediated by plasma-membrane associated KChip3. However, in the cytoplasm,
506 KChip3 is also known as the enzyme calsenilin, regulating presenilins, and in the nucleus,
507 KChip3 acts as gene-transcription-repressor DREAM (downstream regulatory element
508 antagonist modulator), illustrating the importance of cellular localization-analysis (Burgoyne,
509 Helassa, McCue, & Haynes, 2019; Naranjo & Mellström, 2012). A prerequisite for DLAP-6
510 training was the availability of a suitable Kv4.3 antibody that we and others had already used
511 for immunoelectron-microscopy (Haddjeri-Hopkins et al., 2021; B. Liss et al., 2001;
512 Subramaniam et al., 2014).

513 **Figure 8a** shows a typical confocal image of a TH-positive SN neuron in a coronal mouse brain
514 section, after IF-staining, before automated cell-body detection (input image), and after manual
515 as well as algorithm-based identification of the cell cytoplasm (TH, red), the nucleus (DAPI,
516 blue), and the plasma-membrane (Kv4.3, green). As expected, the highest relative
517 fluorescence (RF) signals each were detected in these respective compartments, with manual
518 as well as with DLAP-6 (RF for TH in cytoplasmic compartment: manual 55±3% vs. DLAP-6
519 57±4%, p=0.5862; DAPI/nucleus: 76±7% vs. 76±8%, p=0.9270; Kv4.3/membrane: 75±8% vs.
520 68±9%, p<0.0001; **Figure 8b, Table S15, S16**).

521 Particularly for detecting the RF-signal in the plasma-membrane compartment, the algorithm
522 appeared superior or more consistent/precise than the manual analysis. Accordingly, the
523 single cell correlation manual vs DLAP-6 is less good - but still very high - (R^2=0.93 for
524 membrane compared to 0.99 for cytoplasm and nucleus, **Figure 8c, Table S16**). Most
525 importantly, the DLAP-6 algorithm has successfully learned to identify SN DA neuron plasma-
526 membranes, irrespective of a Kv4.3 derived fluorescence signal, and thus enables a reliable
527 identification of the membrane-compartment in the absence of a membrane-derived
528 fluorescence-signal. For a direct proof, we tested the DLAP-6 approach on SN DA neurons
529 from Kv4.3 knock-out (KO) mice (**Figure 8d, S7, Table S17).** As expected, SN DA neurons
530 from Kv4.3 KO mice did not show any Kv4.3 derived membrane-signal higher than the
531 background, while in wildtype (WT), mean RF-values were ~10-fold higher (DLAP-6: RF KO:
532 0.8±0.5, RF WT: 7.7±2.9, $p<0.0001$). Nevertheless, the plasma-membrane compartment was
533 marked by the DLAP-6 approach in TH-positive neurons from KO mice with similar robustness
534 as for neurons from wildtype mice - a nearly impossible task by manual analysis.

535

536

537 ## Discussion

538 Here, we detail a deep learning-based image analysis platform (DLAP), including six pre-
539 designed algorithms for automated image analysis, that allows rapid and unbiased cell count,
540 as well as quantification of fluorescence signals (e.g. derived from mRNA or proteins) in a
541 given ROI. These are common tasks in cell biology, but manual analysis is time consuming
542 and prone to human error (Sommer & Gerlich, 2013; Xu et al., 2019). However, automated AI
543 based and related approaches like ImageJ/Fiji plugins such as the Trainable Weka
544 Segmentation (Arganda-Carreras et al., 2017), CellProfiler (Carpenter et al., 2006; McQuin et
545 al., 2018), QuPath (Bankhead et al., 2017), U-Net (Falk et al., 2019), and DeepImageJ
546 (Gómez-de-Mariscal et al., 2021), or the HALO® image analysis platform by Indica Labs
547 (Brodie, 2020), require significant computational skills and/or high-end hardware, a significant
548 barrier for their routine use (Kraus et al., 2017; Levet et al., 2021; von Chamier, Laine, &
549 Henriques, 2019). Hence, manual approaches are still widely used for image-analysis in life
550 sciences (Brown, 2017; Helmstadter et al., 2021; Holland & Davies, 2020).

551 Our DLAP approach overcomes these issues by providing already pre-trained neural network
552 algorithms that can learn to detected new labels and extract desired features, with only a small
553 amount of additional training-images. The six DLAP algorithms are pre-designed to suit most
554 common life science tasks, and are easily adapted to distinct scientific needs. DLAP
555 dramatically reduces the respective analysis-time, and it is straightforward to use (utilized by
556 under-graduate students in our lab). Moreover, as training and image-analyses are carried out

557 via an easy-to-use web-based interface (https://wolution.ai/), and Wolution provides in case in-
558 depth support for specific adjustments, our approach does not require any sophisticated
559 hardware, software, or programming skills. Importantly, DLAP details are not proprietary, but
560 all steps and strategies are provided here for free and in full detail, to facilitate distribution and
561 use within the scientific community. These features represent important advantages in
562 comparison to other cloud-based analysis pipelines, for example Aiforia (Benkert et al., 2019;
563 Penttinen et al., 2018), CDeep3M (Haberl et al, 2018), or Visiopharm (Maffeis et al., 2019) that
564 do not disclose insights into the underlying algorithms, do not allow user-based modifications,
565 or require advanced programming experience (e.g. DeepCell Kiosk (Bannon et al., 2021)).

566 We have trained and optimized our DLAP procedures to detect, count, and analyse individual
567 dopaminergic neurons from fixed mice and human brain samples, identified by tyrosine-
568 hydroxylase (TH) expression, but the flexible design allows their quick and easy adaption to
569 other cell types, specimens, and scientific questions. The here detailed DLAP approach allows
570 the systematic quantitative analysis and anatomical mapping of several thousands of neurons
571 in reasonable time, and thus facilitates the identification and characterization of small cellular
572 subpopulations. Accordingly, by DLAP-analysis of more than 20.000 TH-immuno-positive SN
573 neurons in PFA-fixed brain-sections from adult mice, and by generation of expression-maps
574 according to anatomical coordinates, we defined a small subpopulation of neurons (~5% of all
575 TH-positive SN neurons). These neurons were immuno-negative for the dopamine transporter
576 DAT, and were mainly located in the caudo-lateral SN. DAT is a major determinant of activity
577 and excitability of DA neurons, and of dopamine homeostasis and transmission (Bu et al.,
578 2021; Condon et al., 2019; Miller et al., 2021). It is inhibited e.g. by methylphenidate and
579 amphetamines as treatment for ADHD and depression (Torres, Gainetdinov, & Caron, 2003;
580 Vaughan & Foster, 2013). In line, changes in DAT expression have been reported in
581 schizophrenia, ADHD, and Parkinson's (Palermo & Ceravolo, 2019; Salatino-Oliveira, Rohde,
582 & Hutz, 2018).

583 However up to now, independent from disease states, only for VTA DA neurons, lower DAT
584 expression levels have been systematically analyzed (Fu et al., 2012; S. Lammel et al., 2008;
585 Li et al., 2013). On the contrary, for SN DA neurons, DAT is commonly used as marker besides
586 TH (Ciliax et al., 1995; Palermo & Ceravolo, 2019; Poulin, Gaertner, Moreno-Ramos, &
587 Awatramani, 2020), and for their targeting, for instance, via DAT-Cre transgenic mouse lines,
588 expressing the Cre-recombinase under the DAT-promotor (Gong et al., 2007; Stephan Lammel
589 et al., 2015; Papathanou et al., 2019; Stuber et al., 2015). Our results imply that with such
590 approaches, target-gene expression might not be affected in those lateral SN DA neurons that
591 are immuno-negative for DAT protein. However, it must be noted that we did not perform an
592 absolute DAT-protein quantification. Hence, we explicitly do not exclude very low expression
593 of DAT protein in the plasma-membranes of these lateral SN neurons, within the range of the

respective detected DAT-background immuno-signals. Such a low expression would be sufficient for successful DAT-Cre recombination. Using the TH-promotor instead of DAT could cause issues due to its non-specificity to dopamine neurons (Stephan Lammel et al., 2015; Stuber et al., 2015). An alternative marker for all SN DA neurons might be DCC (deleted in colon cancer), the receptor for the axon guidance molecule netrin. In the midbrain, DCC expression is largely restricted to TH-positive neurons (Brichta & Greengard, 2014; Osborne, Halliday, Cooper, & Keast, 2005). However, we did not yet analyze DCC-expression in DAT-negative SN DA neurons.

We have also not yet systematically addressed for the co-expression of the Ca^{2+} binding protein calbindin-$_{d28k}$ (CB), a marker for less vulnerable SN DA neurons in the dorsal tier (Brichta & Greengard, 2014; González-Hernández, Cruz-Muros, Afonso-Oramas, Salas-Hernández, & CastroHernández, 2010). However, DA neurons in the lateral SN which express CB are more sensitive to the effect of the PD-toxin 6-OHDA than other SN DA neurons which do not express CB (Rodríguez, Barroso-Chinea, Abdala, Obeso, & González-Hernández, 2001), and even more compared to the resistant CB-positive dorsal tier SN neurons (Brichta & Greengard, 2014; P. Damier, E. Hirsch, Y. Agid, & A. Graybiel, 1999; Yamada, McGeer, Baimbridge, & McGeer, 1990). Hence, it is likely, that the DAT-negative lateral SN neurons might co-express CB to a higher degree, than DAT-positive SN DA neurons. Very lateral SN DA neurons have been reported to be negative for aldehyde dehydrogenase 1 (Aldh1a1), negative for SOX6, and positive for the vesicular glutamtate transporter Vglut2 (Poulin et al., 2020). However, whether they are also negative for DAT, and a possible co-expression pattern with CB has not yet been systematically addressed.

In terms of differential vulnerability of SN DA neurons, it is important to note that the (caudo-) lateral SN DA neurons project into the (rostro-) dorsolateral striatum (Ambrosi & Lerner, 2022), and correspond to the ventro-lateral SN DA neurons in humans (Düzel et al., 2009; McCutcheon, Abi-Dargham, & Howes, 2019). These neurons display a particularly high vulnerability in Parkinson's compared to rostro-medial SN DA neurons (P. Damier et al., 1999; German, Manaye, Smith, Woodward, & Saper, 1989; Hassler; Jellinger, 2012). In fact, the ventrolateral SN DA neurons are almost completely lost in early PD, at a time point were other SN DA neurons are still largely intact (Kordower et al., 2013). Hence, it is tempting to speculate that the here described DAT-negative population of very lateral SN DA neurons is highly vulnerable and particularly affected by PD-stressors. In line, there is no clear positive correlation between DAT-expression and vulnerability (González-Hernández et al., 2010), suggested in earlier studies (Hurd, Pristupa, Herman, Niznik, & Kleinman, 1994; Uhl, Walther, Mash, Faucheux, & Javoy-Agid, 1994).

What is known about the function of lateral SN DA neurons? Vglut2 and CB positive but Aldh1a1 negative lateral SN DA neurons are important for responses to novel cues and salience (Kim, Ghazizadeh, & Hikosaka, 2015; Menegas, Babayan, Uchida, & Watabe-Uchida, 2017; Todd, Lipski, & Freestone, 2022). Some lateral SN DA neurons are activated by aversive stimuli or cues that predict aversive stimuli (Matsumoto & Hikosaka, 2009). Lateral SN DA neurons *in vivo* display a higher burst activity (that is particularly metabolically demanding) compared to medial SN DA neurons (Farassat et al., 2019). *In vitro*, the pacemaker frequency of lateral but not medial SN DA neurons is positively coupled to the activity of Cav1.3 L-type voltage gated Ca^{2+} channels (Shin et al., 2022). These channels have been linked to defining the distinct vulnerabilities of DA neurons in PD (Johanna Duda, Pötschke, & Liss, 2016; Birgit Liss & Surmeier, 2022; Ortner, 2021; Sandoval et al., 2022). However, it should be noted that the definition of the “lateral SN” in most of these studies is much broader, and likely includes the here defined very lateral SN DA neurons, but also more medial, DAT-positive neurons in the lateral SN.

One very recent study has indeed addressed the electrophysiological properties exclusively of only very lateral SN DA neurons, expressing either CB or Vglut2, most likely overlapping with the very lateral DAT immuno-negative neuronal population that we describe here. These neurons had a higher input resistance and excitability, and they displayed a less precise pacemaker, with lower frequencies and less prominent after-hyperpolarizations, compared to classical SN DA neurons (Sansalone, Zhang, Evans, & Khaliq, 2022). However, future studies are necessary to fully characterize the here defined and quantified subpopulation of lateral SN DA neurons, in terms of their distinct molecular identity, their axonal projections, their physiological function, and their fate in disease.

Methods

DLAP algorithms 1-6; neural networks, training, post processing parameters

Convolutional neuronal networks - DeepLab3 and FCN.

We have used two very different neuronal network architectures, based on either the DeepLab3 network architecture or on a fully convolutional neural network (FCN). DeepLab3 based networks are more powerful for detecting complicated larger objects, like complex neuronal structures, and beyond, while FCN perform in general better for fine structures (like RNAscope probe derived, small individual dots), rather than large global concepts (L.-C. Chen, Papandreou, Schroff, & Adam, 2017; Long et al., 2015). Both types of neural networks belong to the class of convolutional neuronal networks (CNN), commonly used for image analysis (Greener et al., 2022). Convolutional layers do not receive their inputs from the whole previous layer but only from a certain area (called 'filter' or 'kernel') which increases their computational efficiency (S. Wang, Yang, Rong, Zhan, & Xiao, 2019). Moreover, they assign to each pixel in the image a class, such as cellular nucleus or background. This type of analysis is called semantic segmentation. The performance of deep learning based semantic segmentation depends strongly on the neural network architecture, training parameters and in particular the quality of the training data set. By specific training and further optimizing these two network-types for distinct tasks, we generated six distinct algorithms, as specified in **Table1 and 2**.

For cell counting and immunofluorescence signal quantification (DLAP-3 to 6), the large pre-trained neural network DeepLab3 (L. C. Chen et al., 2018) was further trained and optimized past training for the respective specific tasks. DeepLab3 is one of the best performing image segmentation algorithms on the Pascal Visual Object Classes (VOC) dataset (Everingham et al., 2006). This is a standardized image data set for building and evaluating algorithms, often used as a benchmark for segmentation quality. In general, the key innovation of DeepLab algorithms is the use of so called dilated or atrous convolutions. This type of convolutions has a dilated filter size, increasing the area covered by each filter, and the context that can be incorporated. Therefore, they have a higher resolution and can integrate information over larger areas, while keeping the number of parameters of the convolutions the same (L.-C. Chen et al., 2017). Specifically, for our algorithms 3 to 6, we used xception65 as the CNN backend, provided by Google [https://github.com/tensorflow/models/tree/master/research/deeplab] (Chollet, 2017), which was pre-trained on the Pascal VOC 2012 segmentation dataset (Everingham et al, 2015).

For analysis of RNAscope data, we developed (DLAP-1 and 2), belonging to the class of FCN, as the trained respective algorithms based on DeepLab3 were not optimal for reliable detection of RNAscope-derived dot-numbers (**Table S1**). The most important modification of the FCN architecture is that it uses only convolutions, rather than including fully connected linear layers

(Long et al., 2015). Replacing the linear layers with fixed dimensions by convolutions allows the network to accept arbitrarily large images for processing and making predictions (called interference), and to process them very efficiently - limited mainly by the graphics processing unit (GPU) memory size. The FCN architecture, illustrated in **Figure 2**, is our own development, using the Tensorflow library [https://www.tensorflow.org/]. Our FCN network uses five convolutional layers, connected by the Rectified Linear Units (ReLU) activation function. This function only transfers the direct output of the previous layer to the next layer, if it is positive, while it returns zero for negative outputs (Nair & Hinton, 2010). Our network does not include any downsampling/downsizing to reduce image resolution through dropout or strided (kernel step size > 1) convolutions. Therefore, the output image has the same resolution as the input image, and fine structures are not smoothed out. We used another approach of neural network architectures, the so-called 1x1 convolutions, to reduce the number of feature maps and keep the parameter number tractable (Lin, Chen, & Yan, 2013). Such a convolution is used between feature map 2 and feature map 3 to reduce the number of kernels by a factor of 4, thus reducing the parameter size of the following convolution by a factor of 16. To conserve image dimension, we extend the outer frame at the boundary of each image, which increases the space for the filter/kernel to scan the image, a process also called mirror padding. This architecture provided a good compromise between simplicity (and thus computational speed) and segmentation quality.

CNN training parameters for six individual tasks.

Training dataset need to have sufficient quality and size, depending on data variability (Moen et al., 2019; von Chamier et al., 2019). However, using too large training datasets can lead to overfitting, which leads to decreased generalization, and the algorithm fails to optimally apply learned concepts on a sample that it has not already seen during training. We ensured the quality (e.g. resolution, frame size) of our training datasets, and performed a quality evaluation during training (see below), in additional to data-validation by comparison with manual analyses. Images showing different neuronal shapes/forms in different brightness intensities were used for training to ensure the identification and recognition over a vast array of brightness and cellular structure.

As our FCN is not based on a pre-trained neural network (no "transfer learning"), it was trained by us from scratch, by only using our own training data. The FCN-based algorithms 1 and 2 analyse image patches of size 63^2 pixels. To train the network, we randomly cropped the images from our manually labelled training data set (ground truth data) into such patches. Training was performed using the stochastic first-order gradient-based Adam optimizer with default settings (learning rate α=0.001, estimates decay rates β_1=0.9, β_2=0.999, to prevent division by zero $\varepsilon=10^{-8}$) (Kingma & Ba, 2014). For DeepLab3 based algorithms DLAP-3 to 6,

we adjusted the neural network weights by further training with our own data sets using the training script provided by Google Research (Chollet, 2017). This was performed on randomly sampled patches of size 512^2 pixels much larger than the 63^2 pixels we use in the FCN algorithm, as Deeplab3 is designed to detect large, complex objects within an image.

For both network-types, the training time on a modern GPU was several hours for each of the data sets. The number of images and neurons each that were used to train each of the individual algorithms is given in **Table 2**. We used 80% of our manually labelled training data set for training and 20% (referred to as 'test data') to evaluate the segmentation quality. For this performance-evaluation of the individual algorithms, the 'test data' was analyzed and the results were compared to the ground truth provided by the labels. For all algorithms, we assessed typical quality measures (**Table 1**, **S1**): The pixel error rate, i.e. the global percentage of pixels that are wrongly classified. This global error rate was calculated by defining for each segmentation class the rates of true positives (TP), true negatives (TN), false positives (FP) and false negatives (FN), each given in % of the total pixels of the whole training data set. The specificity [defined as TN/(TN+FP)] and the sensitivity [defined as TP/(TP+FN)], for each segmentation class, were also calculated, as these values are more suitable measures in cases of large class imbalance.

We trained each data set until the training error/loss function (difference between output and ground truth) converges minimum. We also verified that we did not overtrain, by tracking the pixel error in the 'test data'. If overtraining is happening, only the training error is still getting lower, while the test error increases. Therefore, training was stopped as soon as the pixel error starts to get worse not better.

Post training image analysis optimization.

After CNN training was completed, the quality of the CNN outputs for each task (summarized in **Table 1**) was further improved by, implementing additional classic image analysis procedures (a) to (e), specified below, into the individual CNN procedures. If an analysis step was further increasing the correlation between algorithm- and manually-obtained results for a distinct task, it was implemented into the respective algorithm. The specific steps (a-e) that were implemented post-training into each of the final algorithms are summarized in **Table 2**.

a) Watershed algorithm. This algorithm requires a set of markers, which are associated with the centers of respective target structures (Kornilov & Safonov, 2018). These markers are obtained by calculating the Euclidean distance transform of the binary mask of target structures cells (detected by the neural network), and then finding peaks in the distance image. Starting from these markers, the watershed algorithm "floods" the image until all pixels are assigned

760 with a watershed region. We used this algorithm in both FCN based algorithms, for a better
761 separation of mRNA molecule derived dots. The FCN output tend to connect single fluorescent
762 dots of individual mRNA molecules, which biases their number count. We found that by
763 applying a classical watershed algorithm, we can separate these points and get a number
764 count much closer to the truth (manual count). For the DeepLab3 based algorithms 4 and 5,
765 watershed algorithm were used to improve segmentation of neighboring nuclei/cells. This was
766 not necessary for DLAP-3.

767 *b) Morphological operations*. A series of morphological operations of type dilation and erosion
768 (Fisher, 1996) were applied to algorithms 1 and 2. These operations add to or remove pixels
769 from the object boundaries. This improves separation of individual neurons and smoothes out
770 uneven boundaries provided by the CNN. This approach was used in both FCN-based
771 algorithms for a better separation of individual neurons.

772 *c) Binary fill-holes-function.* This function was applied to the DeepLab3-based CNN outputs for
773 DLAP-4 to 6, were pixel-wise semantic segmentation resulted in holes within the detected
774 compartments, as such holes are of no biological meaning. Therefore, all holes in the
775 segmentation masks of each region were filled using the "*binary_fill_holes*" function (González-
776 Hernández et al., 2010) of the SciPy library
777 http://scipy.github.io/devdocs/reference/generated/scipy.ndimage.binary_fill_holes.html.

778 *d) Remove target gene color channel procedure.* This procedure was applied to the DeepLab3
779 based algorithms 5 and 6 to facilitate identification of the target areas within the ROI (i.e
780 neuronal cell bodies or neuronal compartments), in which the relative target-gene derived
781 fluorescence-signal was quantified. This procedure is removing the target gene channel for the
782 algorithm-based detection of the target areas, to ensure its recognition, independently of the
783 target gene fluorescence-signal. For excluding the target-gene channel, the respective color
784 layer of the image was set to zero before passing the image through the CNN (both for training
785 and analysis), and it was added back, for the target-signal quantification step of the algorithms.

786 e*) RGB intensity threshold*. Such threshold was included to the DeepLab3 based algorithms 5
787 and 6, to optimize background intensity quantification for calculation of relative target-gene
788 signal-intensities in identified target areas (i.e. neuronal cell bodies or neuronal compartments)
789 to correct for non-uniform intensity conditions in different images/experiments. It was not
790 always straight- forward to determine the individual background-intensities, because some
791 images contained large regions with no detected target areas, but also with no apparent blank
792 background. We included RGB intensity thresholds (for widefield and for confocal images) of
793 pixel values ranging from 10-40 for each channel, depending on its raw intensities, to exclude
794 pixels higher than this threshold from determining background signal intensities.

795

796 **Mice**

797 Juvenile (~PN13, Figure 5 data), and adult (~PN90) male mice were bred at Ulm University at
798 a 12-hour light/12-hour dark cycle and were fed ad libitum. Kv4.3 KO mice were obtained from
799 Jean-Marc Goaillard (Haddjeri-Hopkins et al., 2021). All animal procedures were approved by
800 the German Regierungspräsidium Tübingen (Ref: 35/9185.81-3; TV-No. 1043, Reg. Nr. o.147)
801 and carried out in accordance with the approved guidelines.

802 *Drug and saline treated animals* (Figure 4 data), were the same, cohort as already published
803 (Cav2.3 +/+ mice from Benkert et al. (2019)). Drug treated mice were treated in vivo with
804 MPTP/probenecid to introduce SN DA neuron degeneration. Briefly, MPTP hydrochloride was
805 injected 10 times (every 3.5 days for 5 weeks) subcutaneously at a concentration of 20 mg/kg
806 saline (sigma) together with probenecid intraperitoneally at a concentration of 250 mg/kg 1x
807 PBS (Thermo Fisher). Control mice were injected with saline and probenecid. For all details,
808 including, TH-DAB/hematoxillin staining, stereology, and Aforia-based automated analysis,
809 see (Benkert et al. (2019).

810

811 **Human brain samples**

812 Human midbrain tissue including the substantia nigra (SN) was obtained from the German
813 Brain Bank (www.brain-net.net) Grant-No. GA76 and GA82), as native cryo-preserved tissue
814 blocks (-80 °C/dry ice). Analysis of the human material was approved by the ethic commission
815 of the German Brain Bank as well as of Ulm University (277/07-UBB/se). Detailed information
816 on human midbrain samples is summarized in **Table S5.** Human tissue was processed,
817 stained, and the RNA integrity was assessed via determining the RNA integrity number (RIN),
818 using the Agilent 2100 Bioanalyzer as described (J. Duda et al., 2018).

819

820 **RNAscope® *in situ* hybridization, image acquisition, and data analysis**

821 *RNAscope experiments* were performed essentially as described (Benkert et al., 2019; Siller
822 et al., 2022). *The* RNAscope® technology (Advanced Cell Diagnostics, ACD) was according
823 to the provided protocol for fresh frozen tissue sections [https://acdbio.com]. Details of the used
824 RNAscope probes are given in **Table S2.** All used chemicals were RNAse free grade.

825 12 µm coronal cryosections of mouse or human midbrains were prepared, using a Leica
826 CM3050S cryotome as previously described (Gründemann et al. 2008; Duda et al. 2018),
827 mounted on SuperFrost® Plus glass slides (VWR), and allowed to dry in a drying chamber
828 containing silica gel (Merck) at -20°C for one hour. After fixation with 4% PFA (Thermo Fisher
829 Scientific) in 1x PBS (pH 7.4) for 15 min at 4°C and dehydration via an increasing ethanol

830 series (50%, 75%, 100%, 100%, Sigma), sections were permeabilized for 30 minutes by
831 digestion with protease IV (ACD) at room temperature (RT). Following digestion, respective
832 RNAscope probes (TH probes and target gene probes were processed in parallel) were
833 hybridized for 2 h at 40°C in a HybEZ II hybridization oven (ACD). Signal was amplified using
834 the RNAscope Fluorescent Multiplex Detection Kit (ACD) containing four amplification probes
835 (AMP1-4). In between each amplification step (incubation at 40 °C for 30 min with AMP1/3) or
836 15 min with AMP2/4), sections were washed twice for 2 min with wash buffer (ACD). After
837 RNAscope hybridization, sections were counterstained with 4′,6-diamidino-2-phenylindole
838 (DAPI) ready-to-use solution (ACD, included in Kit) for 30s at RT. Sides were coverslipped
839 with HardSet mounting medium (VectaShield), and allowed to dry overnight at 4 °C. RNAscope
840 probes for TH were labelled with AlexaFluor488, and target gene probes with Atto550.

841 *Image acquisition:* Fluorescent images containing the ROI (i.e. the SN), of murine and human
842 midbrain sections were acquired at 63x magnification using a Leica DM6 B epifluorescence
843 microscope. All images were acquired as z-stacks, covering the full depth of cells, and reduced
844 to maximum intensity Z-projections, utilizing Fiji [http://imagej.net/Fiji]. TH-derived RNAscope
845 fluorescence signals were visualized at 480/40 nm excitation, 527/30 nm emission and 505
846 nm dichroic mirror, target gene-derived fluorescence signals were visualized at 546/10 nm
847 excitation, 585/40 nm emission and 560 nm dichroic mirror, DAPI-signals were visualized at
848 350/50 nm excitation, 460/50 nm emission and 400 nm dichroic mirror. Files were aquired
849 using the LASX software (Leica), and stored as PNG files.

850 *Image analysis*: For manual analysis, the images were further processed using the Fiji software
851 [http://imagej.net/Fiji]. First, cell bodies of individual TH- and DAPI-positive neurons were
852 encircled, using the "Polygon selection" tool to define the area for RNAscope signal
853 quantification. In the next step, a classifier was trained on images only showing target gene
854 signal, by manually labelling and annotating background and dot regions (around 30 labels for
855 each class) in the "Trainable Weka Segmentation". This classifier was then used to classify all
856 target gene images into the two groups "dots" and "background". Afterwards, the threshold for
857 particle recognition was set on classified images, and dots were counted for each cell-specific
858 ROI using the "analyze particle" function. Target probe hybridization results in a small
859 fluorescent dot for each mRNA molecule, allowing absolute quantification of mRNA molecules
860 (via dot counting) independent from fluorescent signal intensity.

861 For automated quantification of RNAscope signals, custom-designed FCN based algorithms
862 DLAP-1 (for mouse-brain sections) and 2 (for human brain sections) and the Wolution-platform
863 were used [https://console.wolution.ai/] (Wolution GmbH & Co. KG, Planegg, Germany).
864 Processed images were uploaded on the Wolution platform, and the algorithms automatically
865 marked cell bodies of TH-positive cells and quantified the number (and the dot area) of target

gene derived fluorescence dots. After algorithm processing, correct identification of cells was controlled by hand and resulted in inclusion of ~50 % correctly identified cells for analysis. If a quantification of all TH-positive neurons is required, neuronal nuclei must be counted, before excluding neurons with not optimally separated cell-bodies for subsequent RNAscope based mRNA quantification in the target cells.

Statistical modelling for brightfield light adjustment:

To asses and correct for a possible influence of neuromelanin (NM) human-derived RNAscope data for, a linear mixed effect model was applied, similar as we had previously described (J. Duda et al., 2018; Schlaudraff et al., 2014). Briefly, we applied a bayesian probabilistic model approach conducted in RStan (Stan Development, 2018) with the R package version 2.21.7, https://mc-stan.org/) using R (version 4.2) under RStudio (version 2022.07). We applied normal distributions for priors of all parameters. To achieve a stable non-degenerate solution priors needed to be properly informed by restricting the effective parameter space. . The chosen model, detailed below, is well-informed by the data on all its parameters and shows an acceptable fit on the age level (see posterior-predictive plots in **Figure S2**).

The number of detected dots/mRNA-molecules for each component/gene (defined as Y_G) is assumed to follow a binomial distribution in which the trial size is derived from cell area s:

$$Y_G \sim Binom(s, p_G)$$

The probability pG of detecting a target molecule is expressed according to a logit-link function (linear combination) as:

$$p_G = \frac{p_{max}}{1 + e^{-g(x)}}$$

where $g(x)$ is an equation, indexed by the mixture-component and a binary discretization of a brains donor (adult vs. aged) that considers a cell's NM concentration (as given by brightfield light transmission, T) according to the Lambert-Beer law which states that concentration is proportional to the negative logarithm of light transmission

$$-log_{10}T = l\varepsilon \cdot c$$

Light transmission

T is the fraction of transmitted to incident light intensity

$$T = \frac{\mathrm{I}_t}{\mathrm{I}_i}$$

896 Since $\mathrm{I}_t < \mathrm{I}_i$ and light intensities are strictly positive, it follows that $0 < T < 1$. For the
897 probabilistic model a distribution for T has to be defined. A continuous distribution bounded on
898 [0, 1] is the Beta-distribution.

899 $$T \sim Beta(\mu_T, \kappa),$$

900 The Beta distribution is parameterized by its mean μ_T and the precision κ.

901 For μ_T we apply a logit-link function

902 $$\mu_T = \frac{1}{1 + e^{-h(x)}}$$

903 $h(x)$ is a linear equation, indexed by the mixture component and binarized age. In addition,
904 the intercept considers a random effect on individual brains. The mixture proportion is modeled
905 to depend on binarized age and to consider a random effect on the brain level, given in
906 Wilcoxon notation (Wilkinson & Rogers, 1973)

907 $$\theta = logit^{-1}(\theta_0 + \Delta_{\theta,age} + (1|brain))$$

908 To adjust experimental results for a mutual NM influence, data were fitted and then reproduced
909 from the model, with each cell's T set to a constant value according to the mean of all brains'
910 μ_T.The influence of BF light transmission (associated to NM content by –log T) on gene
911 expression / dot detection probability can be considered significant with 95%-credible intervals
912 from -5.1 to -1.5 or from -12.2 to -7.7 for low and high expressing cells, respectively
913 (corresponding intervals from the prior distribution vary from -7.8 to +8.0).

914

915 **Immunohistochemistry, image acquisition, and data analysis**

916 *DAB Immunohistochemistry (IHC)* experimental procedures were performed essentially as
917 previously described (Benkert et al., 2019). Briefly, mice were transcardially perfused with and
918 post-fixed (overnight at 4°C) in 4% PFA (Thermo Fisher Scientific) in 1x PBS (pH 7.4). Brains
919 were stored in 0.05% NaN_3 (Sigma) in PBS at 4°C until vibratome (VT 1000S, Leica) cutting
920 (30 µm coronal midbrain sections). All washing and incubation steps during the staining
921 procedure were performed while shaking (300 rpm, microplate shaker, VWR). Free-floating
922 sections were washed (three times in 1xPBS for 10 min) and blocked for 2 hours with 10%
923 normal goat serum (NGS, Vector Laboratories), 0.2% BSA (Carl Roth) and 0.5% Triton X-100
924 (Merck) in 1x PBS to prevent non-specific antibody binding. After further washing (one time in
925 1xPBS for 10 min), sections were incubated with rabbit anti-TH primary antibody (1:5000,
926 Merck) in 1% NGS, 0.2% BSA and 0.5% Triton X-100 (in 1x PBS) overnight at room
927 temperature. Sections were then washed three times in 0.2% Triton X-100 in 1xPBS for 10
928 min and incubated with biotinylated goat anti-rabbit (1:1000, Vector Laboratories) for 2 hours

929 at room temperature. Immunostaining was visualized via VECTASTAIN® ABC system based
930 on Horseradish peroxidase (HRP) detection (Vector Laboratories) using 3,3'-
931 Diaminobenzidine (DAB, Vector Laboratories) as substrate. The slices were mounted on
932 SuperFrost® Plus glass slides (VWR), dehydrated in ascending ethanol series (50%, 70%,
933 90%, 100%, 100%, Sigma) for 10 min each, and cleared with xylene (Sigma) two times for 10
934 min each. Slides were mounted with VectaMount Permanent Mounting Medium (Vector
935 Laboratories).

936 *Hematoxylin-counterstaining:* For counterstaining of already DAB-stained and permanently
937 mounted adult mouse brain sections, slides were incubated in xylene (two times for 5 min) to
938 remove coverslips and rehydrated by an ethanol series (100%, 100%, 90%, 70%, 50%) and
939 H_2O (5 min each). After drying for 5 min, slides were incubated with Vector hematoxylin QS (2
940 min) to counterstain nuclei (Vector Hematoxylin QS Kit, Vector Laboratories). After dehydration
941 in ethanol series and clearing in xylene they were again mounted using VectaMount (all steps
942 as described for DAB-staining).

943 *Stereology:* Stereological estimates of TH-positive neuron numbers were determined using a
944 Leica CTR5500 microscope and the unbiased optical fractionator method (StereoInvestigator
945 software; MBF Bioscience), similar as previously described (Benkert et al., 2019; B. Liss et al.,
946 2005). The SN region throughout the whole caudo-rostral SN axis (Bregma -3.8 to -2.7,
947 according to (Paxinos & Keith B. J. Franklin, 2007) was identified, using well established
948 landmarks (Fu et al., 2012)), and was marked as ROI for TH-positive neuron count. The ROI
949 was marked ab analysed unilaterally on each of the serial DAB-stained sections (37 for
950 juvenile, 40 for adult mice). Sampling grid dimensions were 75 x 75 µm (x,y-axes), counting
951 frame size were 50 x 50 µm (x,y-axes), and counting frame height was 9 or 11 µm for juvenile
952 and adult mice, respectively. Estimated total number of TH-positive neurons (N) was calculated
953 for each animal according to equation (1):

954 $$1)\ N = \sum Q^{-} \cdot \frac{t}{h \cdot asf \cdot ssf}$$

955 with ΣQ^{-} = number of counted neurons, t = mean mounted section thickness (i.e. ~10-11 µm),
956 h = counting frame height (i.e. 80 % of the mounted section thickness), asf = area sampling
957 fraction (i.e. 0.44), and ssf = section sampling fraction (i.e. 1 for SN).

958 Reliability of the estimation was evaluated by the Gundersen coefficient (CE, m = 1) according
959 to equation (2). CE values were all ≤0.05 for all analyzed animals.

960 $$2)\ CE = \frac{\sqrt{s^2 + VAR_{SRS}}}{s^2}$$

961 with $A = \sum_{i=1}^{n} (Q_i^{-})^2$; $B = \sum_{i=1}^{n-1} Q_i^{-} Q_{i+1}^{-}$; $C = \sum_{i=1}^{n-2} Q_i^{-} Q_{i+2}^{-}$

962 s^2 = variance due to noise, and VAR_{SRS} = variance due to systematic random sampling,
963 according to equation (3) for m = 1.

964 $$3)\ VAR_{SRS} = \frac{3(A-s^2)-4B+C}{240} \text{ for m=1}$$

965

966

967 *Automated neuron counting:*

968 *Image acquisition:* Digital images of DAB-stained sections were acquired using a whole slide
969 scanner (3D-Histech Pannoramic 250 Flash III, Sysmex Deutschland GmbH, Norderstedt,
970 Germany or Aperio Versa 8, Leica Biosystems Nussloch GmbH, Nußloch, Germany) and
971 processed using the Fiji software [http://imagej.net/Fiji] were used to combine these layers.

972 *Image analysis*: The digital slides were processed using QuPath [https://qupath.github.io/] to
973 label and cut out the sections of interest (37/40 consecutive SN sections covering the entire
974 caudo-rostral axis). As for stereology, the SN ROI was identified according to the typical
975 landmarks (Fu et al., 2012; Paxinos & Keith B. J. Franklin, 2007) and analyzed unilaterally.
976 Processed sections (showing the ROIs) were afterwards uploaded on the Aiforia® Cloud
977 platform [https://www.aiforia.com/] (Aiforia Technologies Oy, Helsinki, Finland) or the the
978 Wolution platform [https://console.wolution.ai/] (Wolution GmbH & Co. KG, Planegg,
979 Germany). For both automated platforms, in case of flawed sections that could not be
980 automatically analyzed, the counts from the section before and after were averaged to prevent
981 methodological bias (for stereology, these sections were omitted, and this information was
982 taken account for the calculation of the stereological estimates).

983 The Aiforia-platform was only used for analysis of Hematoxylin-counterstained DAB-stained
984 brain sections. It uses a supervised training to establish a non-disclosed deep CNN algorithm
985 that recognized TH-positive neurons, based on nuclear/cell morphology and TH signal. The
986 Aiforia algorithm was trained with 4064 TH-positive neurons (Benkert et al., 2019) and
987 comprised two layers. The individual TH-positive cells were segmented in the first one and
988 counted in the second one (see Penttinen et al. (2018)). For generating the ground truth data
989 used for algorithm training, one circle is placed on top of the nucleus within each TH-positive
990 neuron (instead of marking the whole nucleus), similar as for our respective Wolution-based
991 algorithms DLAP-3 and 4. Only TH-positive cells with a clearly visible/focused nucleus were
992 considered for neuron counting, to avoid counting the same cell on more than one section.
993 Processed images were uploaded on the Wolution platform. For counting of only DAB-stained
994 TH-positive neurons (juvenile mice), DLAP-3 was used, for counting of hematoxylin
995 counterstained TH-positive neurons (adult mice), DLAP-4 was utilized.

996

997 **Immunofluorescence, image acquisition, and analysis**

998 *Immunofluorescence (IF)* experimental procedures were performed essentially as previously
999 described (Benkert et al., 2019). Mouse brains were perfused, stored and cut as already
1000 described for IHC. All washing and incubation steps were performed while shaking (300 rpm,
1001 microplate shaker, VWR).

1002 For automated counting and relative signal-intensity quantification analysis with the DLAP-5
1003 algorithm, immunostaining was performed in two separate cohorts using sequential antibody
1004 incubation. 30 µm coronal midbrain free-floating sections were washed (three times in 1xPBS
1005 for 10 min) and blocked for 2 hours with 10% normal goat serum (NGS, Vector Laboratories)
1006 and 0.5% Triton X-100 in 1x PBS. After blocking, sections were incubated with mouse anti-
1007 DAT (1:500, Thermo Fisher Scientific) primary antibody in carrier solution (1% NGS, 0.5%
1008 Triton X-100 in 1x PBS) overnight at 4°C. Sections were then washed (three times in 1xPBS
1009 for 10 min) and incubated with Alexa Fluor 488 goat anti-mouse secondary antibody (1:1000,
1010 Thermo Fisher Scientific) in carrier solution for 3 hours at room temperature in darkness. All
1011 subsequent staining steps were carried out in darkness. For the second primary antibody
1012 incubation, sections were washed (three times in 1xPBS for 10 min) and incubated overnight
1013 at 4°C with rabbit anti-TH primary antibody (1:1000, Merck) in carrier solution. After washing
1014 (three times in 1xPBS for 10 min), sections were incubated for 3 hours at room temperature
1015 with Alexa Fluor 546 goat anti-rabbit secondary antibody (1:1000, Thermo Fisher Scientific) in
1016 carrier solution. After washing (three times in 1xPBS for 10 min), the sections -were mounted
1017 on SuperFrost® Plus glass slides (VWR) with VectaMount Permanent Mounting Medium with
1018 DAPI (Vector Laboratories).

1019 For relative quantification of fluorescence-signal intensities in cellular compartments (plasma-
1020 membrane, cytoplasm, nucleus) with DLAP-6, two similar Kv4.3 staining protocols were
1021 utilized, adapted from (Haddjeri-Hopkins et al., 2021), leading to very similar results. More
1022 precisely, one WT and one Kv4.3 KO brain (dataset 1) was processed, and images were
1023 acquired in the Goillard lab essentially as described (Haddjeri-Hopkins et al., 2021). The other
1024 brains (dataset 2) were perfused in the Goillard lab, and further processed in the Liss lab,
1025 according to the following protocol. 50 µm free-floating coronal midbrain sections were blocked
1026 for 1 hour 30 minutes with 5% NGS and 0.3% Triton X-100 in 1x PBS, followed by incubation
1027 with a rabbit anti-Kv4.3 primary antibody (1:10000, Alomone Labs) together with chicken
1028 (G)/mouse (L) anti-TH primary antibody (1:1000, Abcam / Merck) in a carrier solution (1% NGS,
1029 0.3% Triton X-100 in 1x PBS) overnight at 4°C. Sections were then washed (three times in
1030 0.3% Triton X-100 in 1x PBS for 15 min) and incubated with Alexa Fluor 488 goat anti-rabbit
1031 secondary antibody (1:1000, Thermo Fisher Scientific) and Alexa Fluor 546 goat anti-mouse

1032 secondary antibody (1:1000, Thermo Fisher Scientific) in carrier solution for 2 hours at room
1033 temperature. After washing (three times in 0.3% Triton X-100 in 1x PBS for 15 min), sections
1034 were incubated with DAPI (1.5 µg/mL; Sigma-Aldrich) for 10 min, washed (two times in 1x PBS
1035 for 10 min), and mounted on glass slides using Vectashield mounting medium.

1036 *Image acquisition:* For automated counting of TH-IF positive neurons und and relative signal
1037 intensity quantification (DAT-IF), fluorescent images of all sections were acquired with Leica
1038 DM6 B epifluorescence microscope (Leica Microsystems) using a 63X oil objective. All image
1039 parameters were set using the LAS X software (Leica microsystems) to avoid saturated pixels,
1040 and identical acquisition settings were maintained (a prerequisite for relative signal-intensity
1041 quantification). TH-IF was visualized at 546 nm (exposure = 300-500 ms, gain = 2), DAT-IF at
1042 488nm (exposure = 600 ms, gain = 2) and DAPI at 405nm (exposure = 300 ms, gain = 1).
1043 Images were acquired as tile scans from a single plane of focus. Merged images were exported
1044 as Leica Image File (LIF).

1045 For relative quantification of fluorescence-signal intensities in cellular compartments, 63X
1046 confocal quality images were acquired using a Zeiss LSM780 with the settings defined in
1047 (Haddjeri-Hopkins et al., 2021) for dataset 1. For dataset 2, confocal images using 100X/1.4
1048 NA oil objective were acquired with STEDYCON (Abberior Instruments) mounted on an
1049 Olympus BX53 upright microscope (Olympus LS), and image parameters were adjusted using
1050 the STEDYCON web-based software (Abberior Instruments). To avoid saturated pixels (a
1051 prerequisite for relative signal-intensity quantification), photon counts from all channels were
1052 monitored in the photon count range indicator using the “fire blue” colour-map. This map
1053 indicates saturated image parts in blue over a yellow-red gradient for each individual channel.
1054 Fluorochromes were excited using an Argon laser, and the following wavelengths were used
1055 for excitation: TH-IF at 546 nm, Kv4.3-IF at 488nm, and DAPI at 405nm. The following
1056 acquisition parameters were adjusted at the stedycon user interface: Pixel size 78 nm; pinhole
1057 diameter 0.71 AU; one-directional line accumulation acquisition; laser power 10% for TH and
1058 Kv4.3, 12% for DAPI. Images were acquired from a single plane of focus and were exported
1059 as OsmAnd Binary Maps (OBF) files.

1060 *Image analysis:* For automated counting of TH-IF positive neurons und and relative signal
1061 intensity quantification, images were converted to 8 bit RGB color TIFF images. The Fiji
1062 software was used to label and cut out the sections of interest (~28 consecutive SN sections
1063 within the caudo-rostral axis, bilaterally), and the ROI was identified according to the typical
1064 landmarks for each section, similar as described for IHC/DAB-stained neuron counting (Fu et
1065 al. (2012), https://mouse.brain-map.org). Processed images were uploaded on the Wolution
1066 platform and DLAP-5 (Wolution GmBH & Co. HG) was used for analysis. The algorithm
1067 automatically identified cell bodies and nucleus of both TH- (red channel) and DAPI-positive

1068 (blue channel) cells within the ROI and directly quantified the mean IF signal intensity per area
1069 for TH, DAPI and the target gene (green channel, DAT) in the cell body and nucleus.
1070 Background (BG) regions (for normalization of signal intensities) were taken from regions
1071 outside the ROI by application of individual IF intensity thresholds for each RGB channel (as
1072 described in post-training procedures). All identified SN cells were manually checked for the
1073 correct and clear identification of full cell bodies and nuclei. If cell bodies were not completely
1074 separated from each other, or if they were cropped, fragmented, very small, or did not show a
1075 full nucleus, these cells were excluded from further semi-quantitative analysis (~30% of
1076 identified TH-positive SN neurons, **Figure 5a**, **Table S12**). This strategy was used, as our aim
1077 was analysis of TH and DAT co-expression and signal-quantification. For absolute
1078 quantification of all TH-positive (or DAT-positive) neurons, a count of neuronal nuclei is
1079 required (and possible), as described for DLAP-3/4.

1080 Raw signal intensities of each cell were normalized to the determined BG signals from the
1081 respective section. The BG signals determined from each analysed section were then
1082 normalized to the mean BG-value for each animal, and outliers were removed. The threshold
1083 for defining DAT-negative SN DA neurons was manually determined and set as the mean
1084 normalized BG value for each mouse, plus 2 times SD or 1.5 times SD (due to different raw
1085 signal intensities of the two different mouse cohorts; **Figure S5c**).

1086 For the generation of anatomical 2D maps, the x and y coordinates (provided by DLAP-5), of
1087 all analysed TH-positive neurons were used, to plot the TH and DAT RF signals, using R
1088 computational environment (Gantz et al., 2018) version 4.2.1 with Tidyverse package
1089 (Carmichael, Sullivan, Lopez, Sun, & Cai, 2021). To merge / compare results from distinct
1090 experiments, data were adjusted for average RF-signals for DAT (or TH). More precisely, as
1091 cohort 2 (3 mice) had ~1.2 fold lower DAT signals, a corresponding correcting factor, CF =
1092 mean DAT cohort 1/ mean DAT cohort 2, was applied.

1093 For relative quantification of fluorescence-signal intensities in cellular compartments with
1094 DLAP-6 algorithm, OBF images were converted to 8 bit RGB color TIFF images using the Fiji
1095 software. For manual analysis, images were further processed using Fiji. First, the “polygon
1096 selection” tool was used to manually delineate a continuous membrane ROI around the cell
1097 based on the Kv4.3 IF signal (green channel). The cytoplasm was marked according to the
1098 immunofluorescence signal for the cytoplasmic TH (red channel), and nucleus was marked
1099 according to the DAPI signal (blue channel). In the next step, the “measure” function (under
1100 the “analyze” toolbar) was used to calculate the mean, RF signal-intensity for each
1101 compartment, already normalized to the respective area. For automated analysis, the same
1102 high resolution RGB color TIFF images were uploaded on the Wolution platform and analysed
1103 with DLAP-6. Each identified TH-positive neuron was segmented into “cytoplasm”,

1104 “membrane” and “nucleus”, based on the cytoplasmic TH and nuclear DAPI fluorescence
1105 signal (after training, the plasma-membrane was reliably identified without a third membrane-
1106 marker). BG signal-intensities were determined from images acquired outside the region of
1107 analysis, using individual RGB channel thresholds, and were used to normalize signal
1108 intensities for both, manual and automated analyses. All images were manually checked for
1109 the correct identification of membrane, cytoplasm and nuclear compartments similar as
1110 performed for analysis with DLAP-5 and ~90 % of cells were used for further quantitative
1111 analysis. In case of non-continuous membrane compartment identification, the weighted mean
1112 (area) of RF signal-intensity in all identified membrane ROIs from each cell was used for
1113 analysis.

1114 **Statistics and software**

1115 Data analysis and graphical illustrations were performed using GraphPad Prism 9 (GraphPad
1116 Software, Inc.), Adobe Illustrator CC2015.3 (Adobe Systems Software), Wolution
1117 (https://wolution.com/), and Fiji (https://imagej.net/Fiji) software. Statistical tests were
1118 performed with GraphPad Prism 9. Anatomical maps were plotted using R computational
1119 environment (Gantz et al., 2018) version 4.2.1 with Tidyverse package (Carmichael et al.,
1120 2021).

1121 Normal distribution was tested with D`Agostino-Pearson omnibus normality test. Correlations
1122 were performed using Pearson correlation test, proportionality constant was calculated from
1123 the ratio between two directly corresponding values. In graphs, data are given as boxplots
1124 showing median and whiskers representing 10th -90th percentile. For analyzing one parameter
1125 non-parametric Mann-Whitney U test and Kruskal Walis test, with post hoc Dunn’s was used.
1126 Testing for two independent parameters was performed via two-way ANOVA with Tukey’s
1127 multiple comparison test. ROUT outlier test (Q=1) was used to remove outliers. Statistical
1128 significances are indicated as ns > 0.05, $p < 0.05$ (*), $p < 0.01$ (**), $p < 0.001$ (***) and $p <$
1129 0.0001 (****).

1130

1131 **Author contributions/Acknowledgment**

1132 NB carried out the RNAscope analysis. SR carried out the protein quantification in cellular
1133 compartments, and assisted MH with neuron count and protein quantification in IF images. DW
1134 and MM implemented and customized all algorithms for automated analysis. SM performed
1135 IHC and IF staining, JW performed stereology and automated cell count analysis for juvenile
1136 mice, HH and JB for adult mice. JRF and JMG provided Kv4.3 KO mice, and high resolution
1137 Kv4.3 immunofluorescence images. MF performed model-based data adjustments. CP
1138 generated 2D maps, JD and RP supervised experiments and helped with analysis. BL

designed and supervised the study, and wrote the manuscript together with NB and SR. All authors revised the manuscript.

We are particularly grateful to the brain donors and the German BrainBank. This study was supported by the German DFG (LI-1745/11-3, GRK1789, SFB1506), the Austrian FWF (F44-12), the Alfried Krupp Foundation, the Boehringer Ingelheim Ulm University BioCenter (BIU), a Wellcome Trust Collaborative Award, and a Research Fellowship by the Hamburg Institute for Advanced Study (HIAS), all to B.L. NB was supported by the International Graduate Schools of Molecular Medicine and of Aging (CEMMA) at Ulm University. MH was supported by an “Experimental Medicine” scholarship of Ulm University.

Competing interests: The authors declare that they have no conflict of interest.

Supplementary material

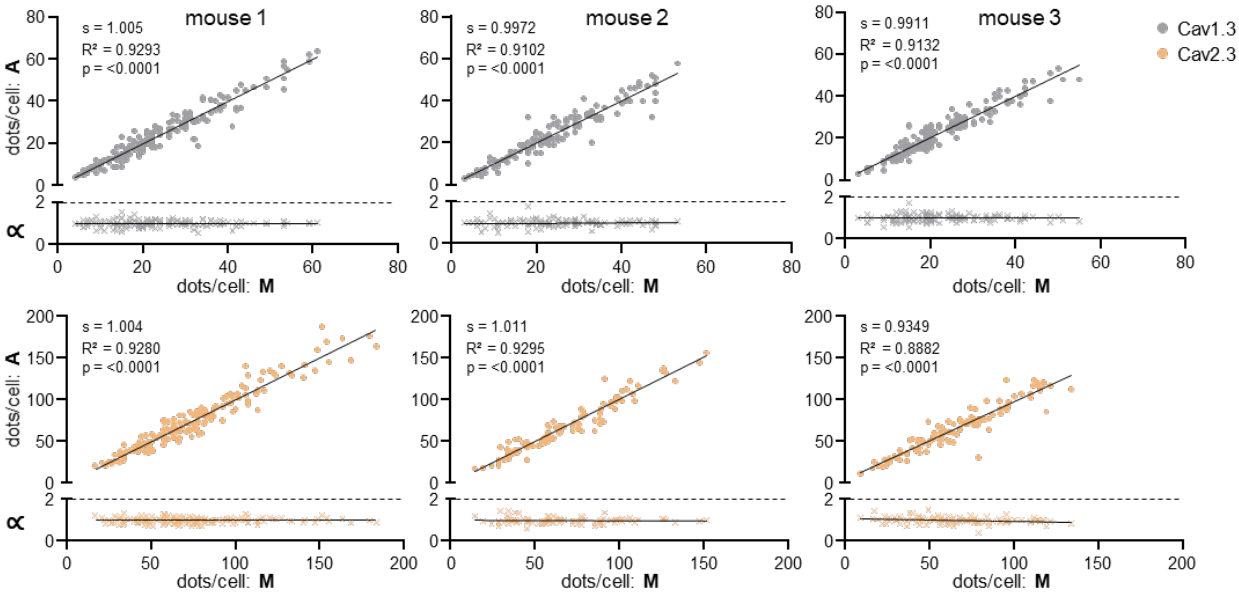

Figure S 1: Comparison between manual and automated RNAscope-derived image analysis. Upper: Single neuron correlations of Cav1.3 (grey) and Cav2.3 (light brown) mRNA-derived dot counts/mouse SN DA neuron between manual and automated analysis according to Pearson correlation test separately for each mouse. Lower: corresponding proportionality constants ∝, calculated from the manual and automated dot count ratios.

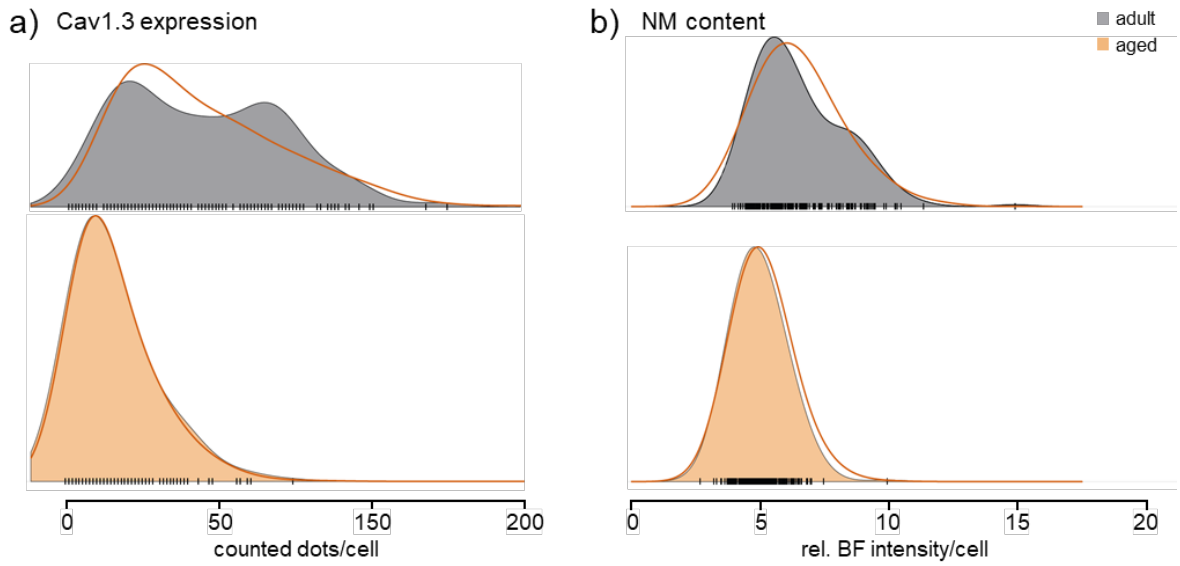

Figure S 2: Posterior-Predictive check of model fits for each brain. Cav1.3 expression (a) and NM content (measured by BF light transmission) (b) data is represented by vertical black lines and the colour-filled kernel densities for adult and aged brains, as indicated. Red continuous lines display the kernel distribution of data reproduced from the fitted model. Note the bimodal distribution in the group of adult brains in Cav1.3 expression and BF light transmission. The model does attribute for the wider base of the distribution of the number of

detected Cav1.3 mRNA moecules (two components mixture of binomials) and BF light transmission (two components of beta), but does not identify the correct mixture proportion.

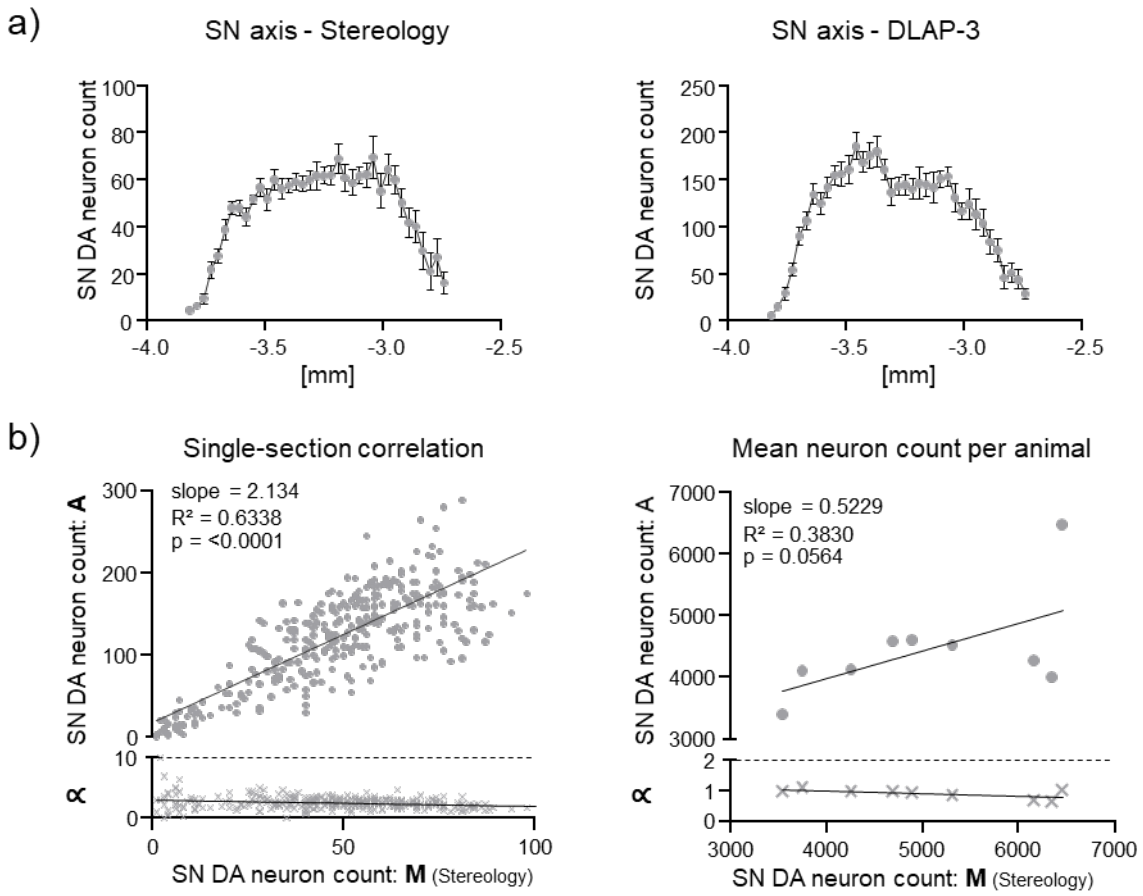

Figure S 3: Comparison between unbiased stereology and automated IHC-derived image analysis of juvenile mouse midbrain sections. a) Mean SN DA neuron counts for all animals (N = 10) in all analyzed sections along the caudal-rostral axis quantified via unbiased stereology (extrapolated via the optical fractionator method, M) or automatically (A) via DLAP-3. Data are given as mean ± SEM. b) Upper: correlations of individual SN DA neuron counts/section and animal (left) and mean SN DA neuron counts/animal (right) between unbiased stereology and automated analysis according to Pearson correlation test. Lower: corresponding proportionality constants ∝, calculated from the manual and automated cell count ratios.

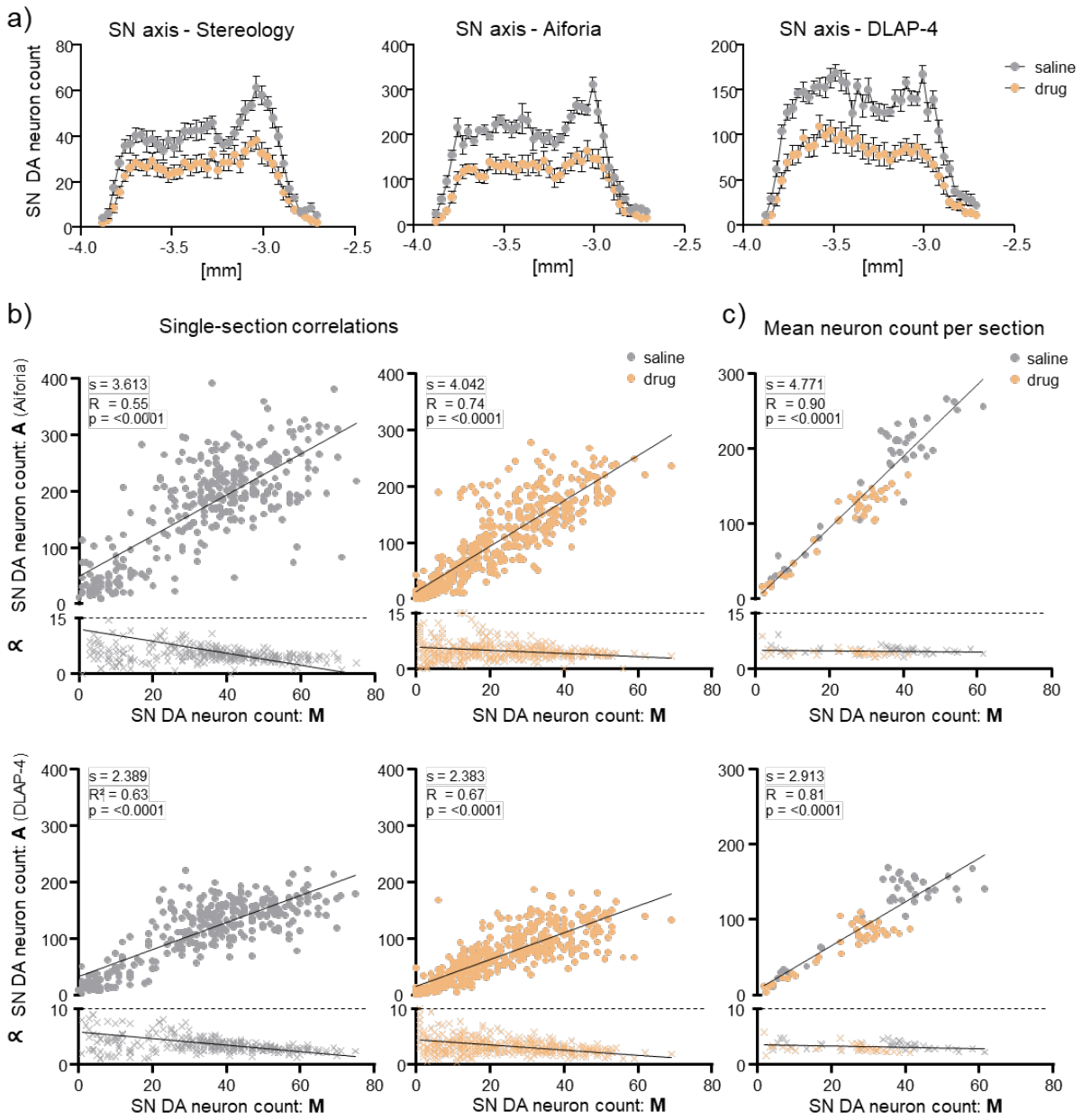

Figure S 4: Comparison between unbiased stereology and automated IHC-derived image analysis of adult mouse midbrain sections. a) Mean SN DA neurons for all animals (saline: N = 9; PD-drug: N = 12) in all analyzed sections along the caudal-rostral axis quantified via unbiased stereology (extrapolated via the optical fractionator method, M) or automatically (A) via an algorithm provided by Aiforia or DLAP-4, as indicated. Data are given as mean ± SEM. b/c) Upper: correlations of individual SN DA neuron counts/section and animal (b) and mean animal counts/section along caudo-rostral axis (calculated from the individual values for each animal, c) between unbiased stereology and automated analysis (Aiforia, or DLAP-4, as indicated) according to Pearson correlation test. Lower: corresponding proportionality constants ∝, calculated from the manual and automated cell count ratios. Stereology data and Aiforia data modified from Benkert et al. (2019).

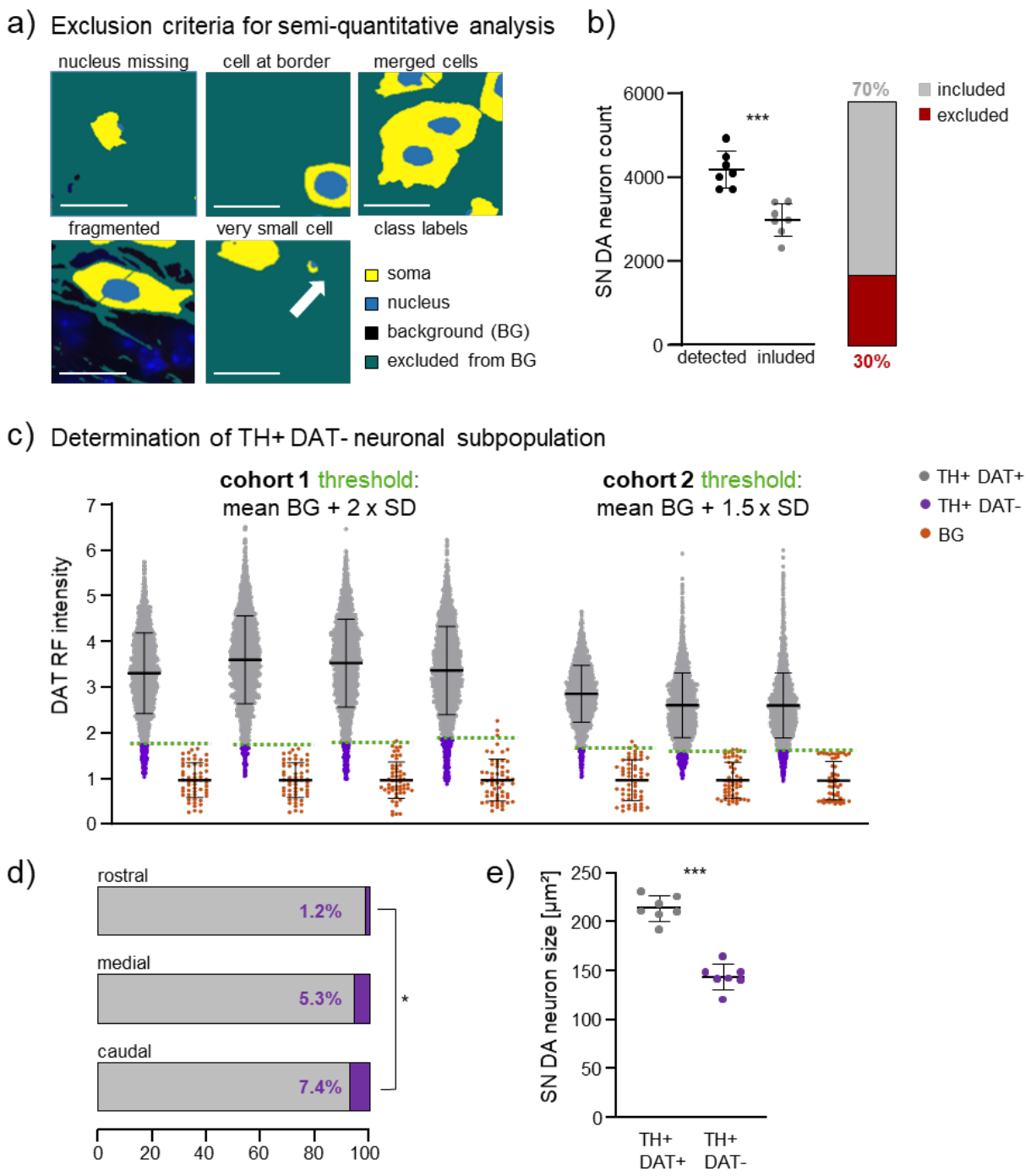

Figure S 5: Semi-quantitative analysis with DLAP-5. a) Detected neurons, where cell bodies were not properly marked, cropped, not clearly separated from each other, fragmented, very small, or did not show a full nucleus, were excluded from further semi-quantitative analysis. Scale bar: 20 µm. b) Left: SN DA neurons/mouse quantified via DLAP-5. Shown are the total TH+ neuron count of all detected neurons and the number of neurons included for semi-quantitative analysis. Data are given as scatterplots (mean, SD) for all analyzed mice (N = 7). Significant differences according to Mann-Whitney test are indicated by asterisks (***: $p < 0.001$). Right: Vertically sliced bar giving the percentage of included and excluded neurons. c) DAT relative fluorescence (RF) intensity per SN DA neuron (TH+) or per BG image, as indicated, quantified vis DLAP-5. Data are given as scatterplots (mean, SD) for all analysed neurons separately for each animal. d) Horizontally sliced bar giving the percentage of TH+DAT+ and TH+DAT- neurons separately for rostral, medial and caudal midbrain sections.

Significant differences indicated according to Chi square test (*: $p < 0.05$) e) SN DA neuron (TH+) (cytoplasm) size of TH+DAT+ or TH+DAT- neurons, as indicated, quantified vis DLAP-5. Data are given as scatterplots (mean, SD) for all analysed animals.

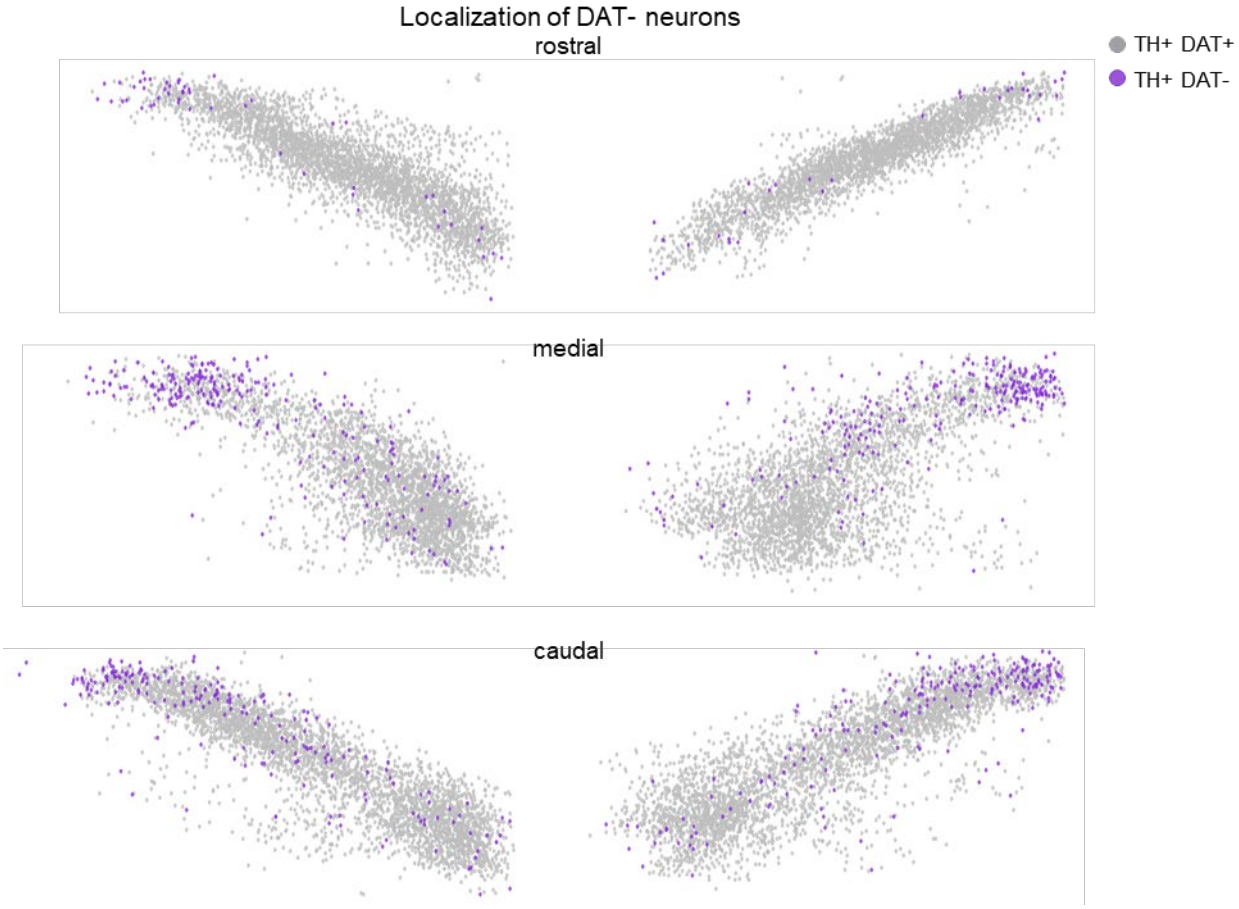

Figure S 6: SN region maps after automated IF-derived image analysis of mouse midbrain sections. Localization maps showing the distribution of TH+DAT+ and TH+DAT- neurons. Given are the individual neurons separately for rostral, medial and caudal sections (N = 7; rostral: TH+DAT- n = 85, TH+DAT+ n = 6584; medial: TH+DAT- n = 423, TH+DAT+ n = 7466; caudal: TH+DAT- n = 469, TH+DAT+ n = 5869).

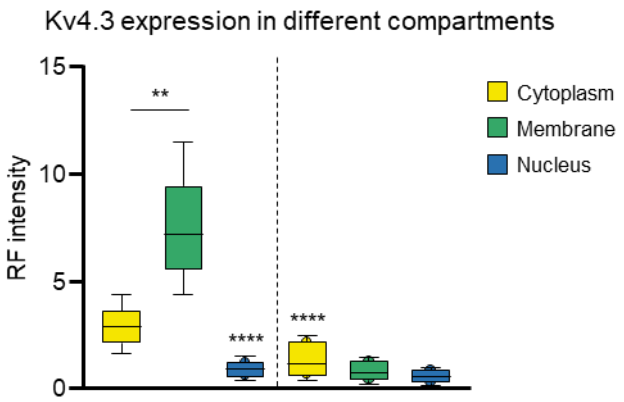

Figure S 7: Automated IF-derived image analysis of WT and Kv4.3 KO mice. Kv4.3 relative fluorescence (RF) intensity/SN DA neurons in different sub-cellular compartments, quantified in WT and Kv4.3 KO mice, as indicated. Data are given as boxplots (median, 10-90 percentile) for all analyzed neurons (WT: n=179, Kv4.3 KO: n = 200). Significant differences according to Kruskal-Wallis with Dunn's multiple comparison tests are indicated by asterisks (**: $p<0.01$, ****: $p < 0.0001$).

1226 **Table S 1: Comparison of FCN and Deeplab3 network performances in distinct tasks.**
1227 Performances were determined by comparing analysis results the test data to the ground truth
1228 data (provided by manual labeling). The following quality measures were assessed separately
1229 for each class: pixel error rate, rates for true positive (TP), true negative (TN), false positive
1230 (FP), false negative (FN) detection as well as specificity (spec.) [defined as TN/(TN+FP)] and
1231 sensitivity (sens.) [defined as TP/(TP+FN)].

D-LAP algorithm		Error [%]	class name	TP [%]	TN [%]	FP [%]	FN [%]	Spec [%]	Sens [%]
1	FCN	5.08	mRNA	0.3	98.9	0.7	0.0	99.3	92.5
			neuron	10.3	84.7	4.1	0.8	95.3	92.7
	DeepLab3	4.39	mRNA	0.0	99.7	0.0	0.3	100.0	0.0
			neuron	11.0	84.6	4.2	0.2	95.2	98.3
2 (human)	FCN	4.13	mRNA	0.2	98.9	0.9	0.0	99.1	94.7
			neuron	5.2	91.0	2.5	1.4	97.3	80.8
	DeepLab3	2.49	mRNA	0.0	99.8	0.0	0.2	100.0	0.0
			neuron	6.1	91.4	2.1	0.4	97.8	95.6
3	FCN	0.64	nucleus	0.0	99.4	0.0	0.6	100.0	1.7
	DeepLab3	0.61	nucleus	0.5	98.9	0.5	0.1	99.5	85.5
4	FCN	0.31	nucleus	0.2	99.5	0.3	0.0	99.7	46.7
	DeepLab3	0.26	nucleus	0.1	99.7	0.2	0.0	99.8	59.8
5	FCN	7.08	nucleus	1.0	97.3	1.5	0.2	98.4	80.9
			cytoplasm	3.7	90.8	4.9	0.7	94.8	83.8
	DeepLab3	3.3	nucleus	0.9	98.5	0.3	0.3	99.7	74.5
			cytoplasm	4.1	92.9	2.2	0.8	97.7	83.7
6	FCN	8.34	nucleus	9.4	87.9	1.2	1.5	98.7	87.2
			cytoplasm	12.4	82.8	4.1	0.8	95.3	93.4
			membrane	2.3	94.2	1.7	1.7	98.2	58.9
	DeepLab3	5.49	nucleus	3.0	93.5	2.5	1.0	97.4	75.6
			cytoplasm	9.7	89.0	0.8	0.5	99.1	95.0
			membrane	11.7	85.2	2.2	0.9	97.5	92.4

1232
1233
1234

1235 **Table S 2: Details of RNAscope probes.** RNAscope target probes were obtained from the
1236 Advanced Cell Diagnostics (ACD) library. All probes detected but did not discriminate between
1237 known splice variants of the respective target genes. Abbreviations: NCBI: National Center for
1238 Biotechnology Information.

Species	Gene	ACD Cat No.	Assay target region according to NCBI Genbank gene accession no. (NM)
mouse	Tyrosine hydroxylase (*Th*)	317621	483 – 1603 of NM_009377.1 (exon 3-13)
	Cav1.3 (*Cacna1d*)	502591	522 – 1994 of NM_001302637.1 (exon 1-10)
	Cav2.3 (*Cacna1e*)	449211	2319 – 3317 of NM_009782.3 (exon 20-22)
human	Tyrosine hydroxylase (*TH*)	441651	596 – 1681 of NM_199292.2 (exon 4-14)
	Cav1.3 (*CACNA1D*)	502591	522 – 1994 of NM_001302637.1 (exon 1-10)

1239

1240 **Table S 3: Mean mRNA molecule numbers in individual mouse SN DA neurons,**
1241 **determined manually and via DLAP algorithm 1.** Data and statistics for graphs in Fig. 3b.
1242 Number of total analyzed neurons is given by n, N represents the number of analyzed mice.
1243 P-values according to Two-way ANOVA followed by Tukey's multiple comparison (significant
1244 values in bold red).

		manual				automated				p-value
	n N	median	10-90 %	mean	±SD	median	10-90 %	mean	±SD	
Cav1.3	449	22	9-41	24	12	23	9-41	24	12	0.9988
	3	24	22-24	24	1	24	23-24	24	1	
Cav2.3	372	66	32-113	70	31	65	31-117	70	32/	0.9995
	3	67	66-75	69	5	67	65-75	69	5	
	Cav1.3 M vs Cav2.3 M, **<0.0001**; Cav1.3 A vs Cav2.3 A, **<0.0001**									

1245
1246
1247

1248 **Table S 4: Single cell correlation analyses between manually and DLAP algorithm 1**
1249 **determined results.** Data and statistics for graphs in Fig. 3c and S1a, according to Pearson
1250 correlation (slope of the linear regression with its own 95% confidence interval).

	Cav1.3	Cav2.3
all mice (N = 3)		
Pearson r (95% confidence interval)	0.959 (0.950-0.966)	0.959 (0.950-0.967)
R squared	0.919	0.920
p-value	<0.0001	<0.0001
No. of XY pairs	444	372
Slope (95% confidence interval)	0.998 (0.971-1.026)	0.989 (0.960-1.020)
Proportionality constant ∝	1.01 ± 0.16	1.00 ± 0.14
mouse 1		
Pearson r (95% confidence interval)	0.964 (0.952-0.973)	0.963 (0.951-0.973)
R squared	0.929	0.928
p-value	<0.0001	<0.0001
No. of XY pairs	168	167
Slope (95% confidence interval)	1.005 (0.962-1.047)	1.004 (0.961-1.047)
Proportionality constant ∝	1.01 ± 0.15	1.00 ± 0.13
mouse 2		
Pearson r (95% confidence interval)	0.954 (0.936-0.967)	0.964 (0.947-0.976)
R squared	0.910	0.930
p-value	<0.0001	<0.0001
No. of XY pairs	131	96
Slope (95% confidence interval)	0.997 (0.943-1.052)	1.011 (0.954-1.068)
Proportionality constant ∝	1.00 ± 0.17	1.00 ± 0.14
mouse 3		
Pearson r (95% confidence interval)	0.956 (0.939-0.968)	0.943 (0.917-0.960)
R squared	0.913	0.888
p-value	<0.0001	<0.0001
No. of XY pairs	145	109
Slope (95% confidence interval)	0.991 (0.941-1.042)	0.935 (0.871-0.998)
Proportionality constant ∝	1.02 ± 0.16	1.01 ± 0.15

1251
1252
1253

1254 **Table S 5: Details of human *postmortem* midbrain samples.** Samples were provided by
1255 the German BrainBank. The mean age of the aged cohort was significantly higher compared
1256 to that of the adult cohort (** = 0.0012; t-test), the mean RIN was significantly lower (*0.038; t-
1257 test), PMI was not significantly different. Abbreviations: AD: Alzheimer's disease; CERAD:
1258 Consortium to establish a registry for Alzheimer's disease; f: female; LB: Lewy Body; m: male;
1259 NFT: neurofibrillary tangles; PD: Parkinson's disease; PMI: post mortem interval, RIN: RNA
1260 integrity number.

Cohort	Age, gender	PMI [h]	RIN	Braak AD/NFT, PD	CERA-stage	LB-pathology
adult	46, f	27	8.5	- , 0	0	no
	34, m	10	8.3	- , 0	0	no
	46, m	19	8.4	- , 0	0	no
mean±SD	42 ± 7**	19 ± 9	8.4 ± 0.1*			
aged	76, m	24	6.9	I, -	A	no
	76, f	11	6.4	0, -	0	no
	81, f	18	4.0	II, -	0	no
mean±SD	78 ± 3	18 ± 7	5.8 ± 1.6			

1261
1262
1263

1264 **Table S 6: mRNA molecule numbers per human SN DA neuron, determined manually**
1265 **and via DLAP algorithm 2.** Data and statistics for graphs in Fig. 4b and c. Number of total
1266 analyzed neurons is given by n, N represents the number of analyzed brain samples. P-values
1267 according to Two-way ANOVA followed by Tukey's multiple comparison (significant values in
1268 bold red).

Cav1.3 mRNA-derived dots/cell										
		manual				automated				p-value
	n N	median	10-90 %	mean	±SD	median	10-90 %	mean	±SD	
adult	223	36	11-68	39	23	37	13-78	42	25	0.6376
	3	38	34-43	38	5	39	34-47	40	7	
aged	258	10	2-32	13	12	12	2-38	17	15	0.2982
	3	16	10-16	14	3	19	13-20	17	4	
	adult M vs aged M, **<0.0001**; adult A vs aged A, **<0.0001**									
rel. BF signal intensity/cell										
		manual				automated				p-value
	n N	median	10-90 %	mean	±SD	median	10-90 %	mean	±SD	
adult	223	16.4	10.8-22.3	16.4	4.5	16.7	11.0-23.1	16.7	4.7	0.9964
	3	16.2	14.5-18.9	16.5	2.2	16.6	14.7-19.0	16.7	2.2	
aged	258	20.4	15.4-26.8	21.2	5.4	20.7	15.6-26.5	21.1	5.1	>0.9999
	3	21.6	20.7-22.2	21.5	0.8	21.5	20.6-22.2	21.4	0.8	
	adult M vs aged M, **<0.0001**; adult A vs aged A, **<0.0001**									
BF-adjusted Cav1.3 mRNA-derived dots/cell										
		manual				automated				p-value
	n N	median	10-90 %	mean	±SD	median	10-90 %	mean	±SD	
adult	180	31	18-50	32	12	31	17-49	32	12	>0.9999
	3	33	30-34	32	2	33	29-34	32	3	
aged	224	17	9-30	19	9	20	11-35	21	10	**0.0436**
	3	18	14-21	17	3	21	16-22	20	3	
	adult M vs aged M, **<0.0001**; adult A vs aged A, **<0.0001**									

1269
1270
1271

1272 **Table S 7: Single cell correlation analyses between manually and DLAP algorithm 2**
1273 **determined results.** Data and statistics for graphs in Fig. 4d and S1b and c, according to
1274 Pearson correlation (slope of the linear regression with its own 95% confidence interval).

	Cav1.3 mRNA dot counts / cell	rel. BF intensity / cell	Cav1.3 molecules, NM/BF-adjusted according to model
all human samples (N = 6)			
Pearson r (95% confidence interval)	0.964 (0.957-0.970)	0.992 (0.990-0.993)	0.897 (0.877-0.915)
R squared	0.928	0.983	0.805
p-value	<0.0001	<0.0001	<0.0001
No. of XY pairs	481	481	404
Slope (95% confidence interval)	1.034 (1.008-1.060)	0.968 (0.957-0.979)	0.867 (0.827-0.910)
Proportionality constant ∝	1.28 ± 1.18	1.01 ± 0.03	1.10 ± 0.25
adult samples (N = 3)			
Pearson r (95% confidence interval)	0.975 (0.967-0.980)	0.996 (0.995-0.997)	0.876 (0.837-0.906)
R squared	0.950	0.992	0.767
p-value	<0.0001	<0.0001	<0.0001
No. of XY pairs	223	223	180
Slope (95% confidence interval)	1.044 (1.012-1.076)	1.033 (1.021-1.046)	0.851 (0.781-0.920)
Proportionality constant ∝	1.23 ± 1.51	1.01 ± 0.02	1.01 ± 0.18
aged samples (N = 3)			
Pearson r (95% confidence interval)	0.890 (0.861-0.913)	0.988 (0.984-0.990)	0.872 (0.836-0.900)
R squared	0.792	0.976	0.872
p-value	<0.0001	<0.0001	<0.0001
No. of XY pairs	258	258	224
Slope (95% confidence interval)	1.130 (1.059-1.201)	0.940 (0.9221-0.958)	0.977 (0.905-1.050)
Proportionality constant ∝	1.33 ± 0.78	1.00 ± 0.03	1.17 ± 0.27

1275
1276
1277

Table S 8: SN DA neuron numbers determined via unbiased stereology and via DLAP algorithm 3 on DAB-stained sections. Data and statistics for graphs in Fig. 5b. Given are the numbers of all TH-positive SN neurons, unilaterally determined for each mouse by stereology or algorithm. N represents the number of analyzed mice. P-values according to Mann-Whitney test (significant values in bold red).

		manual (Stereology)				automated			
	N	median	10-90 %	mean	±SD	median	10-90 %	mean	±SD
	10	4789	3561-6444	4951	1079	4199	3100-6297	4317	911.8
p-value	Mann-Whitney test: 0.2176								

Table S 9: SN DA neuron numbers determined via unbiased stereology and via DLAP algorithm 4 on DAB- and hematoxylin-stained sections. Data and statistics for graphs in Fig. 6b. Given are the numbers of all TH-positive SN neurons/mouse, unilaterally determined by stereology or algorithm. N represents the number of analyzed mice. P-values according to Two-way ANOVA followed by Tukey's multiple comparison (significant values in bold red).

		saline				PD-drug					p-value
	N	median	10-90 %	mean	± SD	N	median	10-90 %	mean	± SD	
manual (stereology)	9	3826	2666-4919	3959	643	12	2556	1209-3587	2504	922	**0.022**
automated (Aiforia)		6881	5749-8418	7048	823		4619	1680-5913	4108	1596	**<0.000**
automated (Wolution)		4797	3442-5084	4614	500		2768	1314-4230	2708	975	**0.0010**
p-values	saline M vs. saline A (W), 0.7441; drug M vs. drug A (W), 0.9963; saline M vs. saline A (A), **<0.0001**; drug M vs. drug A (A), **0.0036**; saline A (W) vs saline A (A), **<0.0001**; drug A (W) vs drug A (A), **0.0156**										

Table S 10: Remaining SN DA neurons after PD-drug (MPTP) treatment determined via unbiased stereology and via DLAP algorithm 4. Data and statistics for graphs in Fig. 6b. Given are the percentages of remaining TH-positive SN neurons/mouse after drug treatment relative to saline, unilaterally determined by stereology or algorithm. N represents the number of analyzed mice. P-values according to Kruskal-Wallis with Dunn's multiple comparison (significant values in bold red).

group	N	median	10-90 %	mean	±SD
manual (Stereology)	12	64.6	30.5-90.6	63.3	23.3
automated (Aiforia)		65.5	23.8-83.9	58.3	22.7
automated (Wolution)		60.0	28.5-91.7	58.7	21.1
p-values	M vs A (W), >0.9999; M vs A (A), >0.9999, A (W) vs A (A), >0.9999				

1298 **Table S 11: Single cell correlation analyses between manually and DLAP algorithm 3**
1299 **and 4 determined results** Data and statistics for graphs in Fig. 5c/6c, according to Pearson
1300 correlation (slope of the linear regression with its own 95% confidence interval).

	juvenile	adult (Aiforia)	adult (Wolution)
Individual sections			
Pearson r (95% confidence interval)	0.796 (0.753-0.832)	0.742 (0.688-0.787)	0.791 (0.746-0.829)
R squared	0.634	0.5500	0.626
p-value	<0.0001	<0.0001	<0.0001
No. of XY pairs	332	3189	319
Slope (95% confidence interval)	2.134 (1.959-2.310)	3.613 (3.251-3.974)	2.389 (2.185-2.593)
Proportionality constant ∝	2.60 ± 1.00	6.48 ± 8.43	3.86 ± 2.34
Individual sections: PD-drug			
Pearson r (95% confidence interval)		0.860 (0.833-0.882)	0.815 (0.781-0.845)
R squared		0.739	0.665
p-value		<0.0001	<0.0001
No. of XY pairs		433	433
Slope (95% confidence interval)		4.042 (3.814-4.269)	2.383 (2.223-2.544)
Proportionality constant ∝		5.00 ± 3.16	3.46 ± 2.12
Mean (for all animals) per section			
Pearson r (95% confidence interval)	0.889 (0.828-0.929)	0.946 (0.917-0.965)	0.897 (0.844-0.933)
R squared	0.790	0.895	0.805
p-value	<0.0001	<0.0001	<0.0001
No. of XY pairs	73	80	80
Slope (95% confidence interval)	2.383 (2.092-2.674)	4.771 (4.402-5.139)	2.913 (2.590-3.236)
Proportionality constant ∝	2.58 ± 0.58	4.81 ± 1.01	3.20 ± 0.74
Mean per animal			
Pearson r (95% confidence interval)	0.619 (-0.018-0.898)	0.901 (0.768-0.960)	0.919 (0.808-0.967)
R squared	0.383	0.812	0.845
p-value	0.0564	<0.0001	<0.0001
No. of XY pairs	10	21	21
Slope (95% confidence interval)	0.5229 (-0.018-1.064)	1.639 (1.260-2.018)	1.057 (0.8396-1.275)
Proportionality constant ∝	0.89 ± 0.15	1.71 ± 0.29	1.13 ± 0.15

1301
1302

Table S 12: Number of SN neurons analyzed via DLAP-5. Data and statistics for graphs in Fig. 7c & S5b,d. Given are the numbers of all TH-positive SN neurons/mouse, bilaterally determined by the algorithm, the number of neurons excluded/included neurons for further DAT analysis (criteria specified in Figure S5a), and the determined number of TH-positive DAT-positive/DAT-negative SN neurons. Rostral, medial and caudal locations were determined according to the respective sterotactic coordinates (bregma: -2.7 mm to -3.1 mm (rostral); -3.1 to -3.5 (medial); -3.5 to -3.9 (caudal)). N represents the number of analyzed mice. P-values according to Wilcoxon or Mann-Whitney tests (significant values in bold red).

	N	mean	±SD	%	mean	±SD	%	mean	±SD	%
		all detected TH+ SN neurons			excluded TH+ neurons from further DAT analysis			included TH+ neurons for further DAT analysis		
whole axis	7	4187	439	100	1171	152	28 ± 3.3	3015	374	72 ± 3.3
p-value		MWU: all vs analyzed TH+ neurons **0.006**								
		identified TH+ DAT+			identified TH+ DAT-			all included TH+ neurons		
whole axis		2876	340	95.5 ± 1.5	139	54	4.5 ± 1.5	3015	374	100
rostral		941	199	98.8 ± 0.6	12	8	1.2 ± 0.6	953	203	100
medial		1067	208	94.7 ± 2.2	60	29	5.3 ± 2.2	1127	225	100
caudal		838	120	92.6 ± 2.4	67	25	7.4 ± 2.4	905	129	100
p-value		Wilcoxon: all analyzed TH+ vs analyzed TH+ DAT+ **0.0156** Chi-square: rostral vs medial, 0.0973 , rostral vs caudal, **0.0304** , caudal vs medial, 0.5515								

Table S 13: Semi-quantitative DAT immunofluorescence per mouse SN DA neuron, determined via DLAP algorithm 5. Data and statistics for graphs in Fig. S5c. n represents the number of total analyzed SN DA neurons or the number background images.

	SN DA neurons					background					threshold
mouse No	n	median	10-90 %	mean	±SD	median	n	10-90 %	mean	±SD	BG-RF+2SD
1	3407	3.4	2.2-4.5	3.3	0.9	1.0	56	0.5-1.5	1.0	0.4	1.8
2	2945	3.6	2.4-4.9	3.6	1.0	0.9	58	0.5-1.4	1.0	0.4	1.8
3	2969	3.6	2.3-4.8	3.6	1.0	0.9	56	0.5-1.6	1.0	0.4	1.8
4	3129	3.4	2.1-4.7	3.4	1.0	0.9	60	0.5-1.6	1.0	0.5	1.9
											BG-RF+1.5SD
5	2715	2.9	2.1-3.7	2.9	0.6	1.1	58	0.4-1.6	1.0	0.4	1.9
6	2314	2.6	1.8-3.6	2.6	0.7	0.9	54	0.6-1.6	1.0	0.4	1.8
7	3417	2.6	1.8-3.5	2.6	0.7	0.9	54	0.5-1.6	1.0	0.4	1.9

Table S 14: SN neuron size according to x,y-coordinates (marked cell body) determined via DLAP-5. Data and statistics for graphs in Fig. S5e. Number of total analyzed neurons is given by n, N represents the number of analyzed mice. P-values according to Mann-Whitney test (significant values in bold red).

		analyzed TH+ DAT+				analyzed TH+ DAT-				p-value
	N	median	10-90 %	mean	±SD	median	10-90 %	mean	±SD	
µm²	7	211	192-231	214	13	142	120-164	144	13	**0.006**

Table S 15: Semi-quantitative immunofluorescence per mouse SN DA neuron, determined manually and via DLAP algorithm 6. Data and statistics for graphs in Fig. 8b. Number of total analyzed neurons is given by n, N represents the number of analyzed mice. P-values according to Kruskal-Wallis with Dunn's multiple comparison and Mann-Whitney test (significant values in bold red).

TH										
		manual				automated				p-value
ROI	n	median	10-90 %	mean	±SD	median	10-90 %	mean	±SD	
cell body	94	272.8	125.6-534.1	307.9	145.4	284.4	134.4-542.0	317.8	147.3	0.6029
membrane		181.2	81.44-357.1	203.4	101.8	162.0	79.78-316.2	180.3	86.10	0.1707
nucleus		39.52	24.33-75.87	45.78	22.51	46.93	26.80-88.50	52.00	24.14	**0.0334**
p-values	Kruskal-Wallis: M; cell body vs nucleus, <0.0001; cell body vs membrane, <0.0001; A; cell body vs nucleus, <0.0001; cell body vs membrane, <0.0001;									
Kv4.3										
		manual				automated				p-value
ROI	n	median	10-90 %	mean	±SD	median	10-90 %	mean	±SD	
cell body	94	2.3	1.4-3.8	2.5	1.0	2.3	1.3-3.9	2.6	1.1	0.5862
membrane		9.0	5.1-15.7	9.9	4.0	6.6	3.9-11.5	7.2	3.0	**<0.0001**
nucleus		0.6	0.3-1.2	0.6	0.4	0.6	0.3-1.1	0.7	0.4	0.9270
p-values	Kruskal-Wallis: M; membrane vs cell body, <0.0001; membrane vs nucleus, <0.0001; A; membrane vs cell body, <0.0001; membrane vs nucleus, <0.0001;									
DAPI										
		manual				automated				p-value
ROI	n	median	10-90 %	mean	±SD	median	10-90 %	mean	±SD	
cell body	94	1.9	1.0-3.2	2.1	1.1	1.6	0.9-2.8	1.8	0.9	0.0765
membrane		0.8	0.5-2.0	1.0	0.6	0.8	0.5-3.4	1.3	1.0	0.3500
nucleus		9.3	6.3-13.5	9.8	2.8	9.3	6.3-13.7	9.7	2.8	0.8212
p-values	Kruskal-Wallis: M; nucleus vs membrane, <0.0001; nucleus vs cell body, <0.0001; A; nucleus vs membrane, <0.0001; nucleus vs cell body, <0.0001;									

1332 **Table S 16: Single cell correlation analyses between manually and DLAP-6 determined**
1333 **results.** Data and statistics for graphs in Fig. 8c. , according to Pearson correlation (slope of
1334 the linear regression with its own 95% confidence interval).

	Cytoplasm: TH	Membrane: Kv4.3	Nucleus: DAPI
Pearson r (95% confidence interval)	0.995 (0.992-0.997)	0.966 (0.949-0.977)	0.996 (0.994-0.008)
R squared	0.990	0.933	0.993
p-value	<0.0001	<0.0001	<0.0001
No. of XY pairs	94	94	94
Slope (95% confidence interval)	1.01 (0.989-1.029)	0.737 (0.696-0.777)	0.986 (0.969-1.00)
Proportionality constant ∝	0.96 ± 0.05	1.38 ± 0.15	1.01 ± 0.03

1335
1336
1337 **Table S 17: Relative immunofluorescence-signal quantification for Kv4.3 in SN DA**
1338 **neuron membranes from WT and Kv4.3 KO mice, determined via DLAP-6.** Data and
1339 statistics for graphs in Fig. 8e & S7. Number of analyzed neurons is given by n, N represents
1340 the number of analyzed mice. P-values according Mann-Whitney test (significant values in bold
1341 red).

WT					Kv4.3 KO					p-value
n N	median	10-90 %	mean	±SD	n N	median	10-90 %	mean	±SD	
179	7.2	4.4-11.5	7.7	2.9	200	0.7	0.21-1.5	0.8	0.5	**<0.0001**
2	7.7	7.2-8.2	7.7	0.7	2	0.9	0.5-1.3	0.9	0.6	

1342
1343
1344
1345

References

Agatonovic-Kustrin, S., & Beresford, R. (2000). Basic concepts of artificial neural network (ANN) modeling and its application in pharmaceutical research. *Journal of Pharmaceutical and Biomedical Analysis, 22*(5), 717-727. doi: https://doi.org/10.1016/S0731-7085(99)00272-1

Aidi-Knani, S., Regaya, I., Amalric, M., & Mourre, C. (2015). Kv4 channel blockade reduces motor and neuropsychiatric symptoms in rodent models of Parkinson's disease. *Behavioural pharmacology, 26*(1-2), 91-100. doi: 10.1097/fbp.0000000000000107

Alam, G., Edler, M., Burchfield, S., & Richardson, J. R. (2017). Single low doses of MPTP decrease tyrosine hydroxylase expression in the absence of overt neuron loss. *NeuroToxicology, 60*, 99-106. doi: https://doi.org/10.1016/j.neuro.2017.03.008

Ambrosi, P., & Lerner, T. N. (2022). Striatonigrostriatal circuit architecture for disinhibition of dopamine signaling. *Cell Rep, 40*(7), 111228. doi: https://doi.org/10.1016/j.celrep.2022.111228

Angermueller, C., Pärnamaa, T., Parts, L., & Stegle, O. (2016). Deep learning for computational biology. *Mol Syst Biol, 12*(7), 878. doi: 10.15252/msb.20156651

Arganda-Carreras, I., Kaynig, V., Rueden, C., Eliceiri, K. W., Schindelin, J., Cardona, A., & Sebastian Seung, H. (2017). Trainable Weka Segmentation: a machine learning tool for microscopy pixel classification. *Bioinformatics, 33*(15), 2424-2426. doi: 10.1093/bioinformatics/btx180

Baddeley, A. (2001). Is stereology 'unbiased'? *Trends Neurosci, 24*(7), 375-376. doi: https://doi.org/10.1016/S0166-2236(00)01833-6

Bankhead, P., Loughrey, M. B., Fernández, J. A., Dombrowski, Y., McArt, D. G., Dunne, P. D., . . . Hamilton, P. W. (2017). QuPath: Open source software for digital pathology image analysis. *Sci Rep, 7*(1), 16878. doi: 10.1038/s41598-017-17204-5

Bannon, D., Moen, E., Schwartz, M., Borba, E., Kudo, T., Greenwald, N., . . . Van Valen, D. (2021). DeepCell Kiosk: scaling deep learning-enabled cellular image analysis with Kubernetes. *Nature Methods, 18*(1), 43-45. doi: 10.1038/s41592-020-01023-0

Bazelon, M., Fenichel, G. M., & Randall, J. (1967). Studies on neuromelanin. I. A melanin system in the human adult brainstem. *Neurology, 17*(5), 512-519. doi: 10.1212/wnl.17.5.512

Benkert, J., Hess, S., Roy, S., Beccano-Kelly, D., Wiederspohn, N., Duda, J., . . . Liss, B. (2019). Cav2.3 channels contribute to dopaminergic neuron loss in a model of Parkinson's disease. *Nat Commun, 10*(1), 5094. doi: 10.1038/s41467-019-12834-x

Berke, J. D. (2018). What does dopamine mean? *Nat Neurosci, 21*(6), 787-793. doi: 10.1038/s41593-018-0152-y

Björklund, A., & Dunnett, S. B. (2007). Dopamine neuron systems in the brain: an update. *Trends Neurosci, 30*(5), 194-202.

Blanchard, V., Raisman-Vozari, R., Vyas, S., Michel, P. P., Javoy-Agid, F., Uhl, G., & Agid, Y. (1994). Differential expression of tyrosine hydroxylase and membrane dopamine transporter genes in subpopulations of dopaminergic neurons of the rat mesencephalon. *Brain Res Mol Brain Res, 22*(1-4), 29-38. doi: 10.1016/0169-328x(94)90029-9

Bloem, B. R., Okun, M. S., & Klein, C. (2021). Parkinson's disease. *Lancet, 397*(10291), 2284-2303. doi: 10.1016/s0140-6736(21)00218-x

Brichta, L., & Greengard, P. (2014). Molecular determinants of selective dopaminergic vulnerability in Parkinson's disease: an update. *Front Neuroanat, 8*, 152. doi: 10.3389/fnana.2014.00152

Brodie, C. (2020). Overcoming autofluorescence (AF) and tissue variation in image analysis of in situ hybridization *In Situ Hybridization Protocols* (pp. 19-32): Springer.

Brown, D. L. (2017). Bias in image analysis and its solution: unbiased stereology. *J Toxicol Pathol, 30*(3), 183-191. doi: 10.1293/tox.2017-0013

Bu, M., Farrer, M. J., & Khoshbouei, H. (2021). Dynamic control of the dopamine transporter in neurotransmission and homeostasis. *NPJ Parkinson's disease, 7*(1), 22-22. doi: 10.1038/s41531-021-00161-2

Burgoyne, R. D., Helassa, N., McCue, H. V., & Haynes, L. P. (2019). Calcium Sensors in Neuronal Function and Dysfunction. *Cold Spring Harb Perspect Biol, 11*(5). doi: 10.1101/cshperspect.a035154

Carmichael, K., Sullivan, B., Lopez, E., Sun, L., & Cai, H. (2021). Diverse midbrain dopaminergic neuron subtypes and implications for complex clinical symptoms of Parkinson's disease. *Ageing Neurodegener Dis, 1*(4). doi: 10.20517/and.2021.07

Carpenter, A. E., Jones, T. R., Lamprecht, M. R., Clarke, C., Kang, I. H., Friman, O., . . . Sabatini, D. M. (2006). CellProfiler: image analysis software for identifying and quantifying cell phenotypes. *Genome Biol, 7*(10), R100. doi: 10.1186/gb-2006-7-10-r100

Chen, A. P. F., Chen, L., Kim, T. A., & Xiong, Q. (2021). Integrating the Roles of Midbrain Dopamine Circuits in Behavior and Neuropsychiatric Disease. *Biomedicines, 9*(6). doi: 10.3390/biomedicines9060647

Chen, L.-C., Papandreou, G., Schroff, F., & Adam, H. (2017). Rethinking atrous convolution for semantic image segmentation. *arXiv preprint arXiv:1706.05587*.

Chen, L. C., Papandreou, G., Kokkinos, I., Murphy, K., & Yuille, A. L. (2018). DeepLab: Semantic Image Segmentation with Deep Convolutional Nets, Atrous Convolution, and Fully Connected CRFs. *IEEE Trans Pattern Anal Mach Intell, 40*(4), 834-848. doi: 10.1109/TPAMI.2017.2699184

Ciliax, B., Heilman, C., Demchyshyn, L., Pristupa, Z., Ince, E., Hersch, S., . . . Levey, A. (1995). The dopamine transporter: immunochemical characterization and localization in brain. *The Journal of Neuroscience, 15*(3), 1714-1723. doi: 10.1523/jneurosci.15-03-01714.1995

Condon, M. D., Platt, N. J., Zhang, Y. F., Roberts, B. M., Clements, M. A., Vietti-Michelina, S., . . . Cragg, S. J. (2019). Plasticity in striatal dopamine release is governed by release-independent depression and the dopamine transporter. *Nat Commun, 10*(1), 4263. doi: 10.1038/s41467-019-12264-9

Damier, P., Hirsch, E., Agid, Y., & Graybiel, A. (1999). The substantia nigra of the human brain: I. Nigrosomes and the nigral matrix, a compartmental organization based on calbindin D28K immunohistochemistry. *Brain, 122*(8), 1421-1436.

Damier, P., Hirsch, E. C., Agid, Y., & Graybiel, A. M. (1999). The substantia nigra of the human brain. II. Patterns of loss of dopamine-containing neurons in Parkinson's disease. *Brain, 122 (Pt 8)*, 1437-1448. doi: 10.1093/brain/122.8.1437

Daubner, S. C., Le, T., & Wang, S. (2011). Tyrosine hydroxylase and regulation of dopamine synthesis. *Arch Biochem Biophys, 508*(1), 1-12. doi: 10.1016/j.abb.2010.12.017

Dragicevic, E., Schiemann, J., & Liss, B. (2015). Dopamine midbrain neurons in health and Parkinson's disease: Emerging roles of voltage-gated calcium channels and ATP-sensitive potassium channels. *Neuroscience, 284*, 798-814. doi: https://doi.org/10.1016/j.neuroscience.2014.10.037

Duda, J., Fauler, M., Grundemann, J., & Liss, B. (2018). Cell-Specific RNA Quantification in Human SN DA Neurons from Heterogeneous Post-mortem Midbrain Samples by UV-Laser Microdissection and RT-qPCR. *Methods Mol Biol, 1723*, 335-360. doi: 10.1007/978-1-4939-7558-7_19

Duda, J., Pötschke, C., & Liss, B. (2016). Converging roles of ion channels, calcium, metabolic stress, and activity pattern of Substantia nigra dopaminergic neurons in health and Parkinson's disease. *J Neurochem, 139*, 156-178.

Dumrongprechachan, V., Salisbury, R. B., Soto, G., Kumar, M., MacDonald, M. L., & Kozorovitskiy, Y. (2021). Cell-type and subcellular compartment-specific APEX2 proximity labeling reveals activity-dependent nuclear proteome dynamics in the striatum. *Nat Commun, 12*(1), 4855. doi: 10.1038/s41467-021-25144-y

Düzel, E., Bunzeck, N., Guitart-Masip, M., Wittmann, B., Schott, B. H., & Tobler, P. N. (2009). Functional imaging of the human dopaminergic midbrain. *Trends Neurosci, 32*(6), 321-328.

Everingham, M., Eslami, S. M. A., Van Gool, L., Williams, C. K. I., Winn, J., & Zisserman, A. (2015). The PASCAL Visual Object Classes Challenge: A Retrospective. *International Journal of Computer Vision, 111*(1), 98-136. doi: 10.1007/s11263-014-0733-5

Everingham, M., Zisserman, A., Williams, C. K. I., Van Gool, L., Allan, M., Bishop, C. M., . . . Zhang, J. G. (2006). The 2005 PASCAL visual object classes challenge. *Machine Learning Challenges, 3944*, 117-176.

Falk, T., Mai, D., Bensch, R., Cicek, O., Abdulkadir, A., Marrakchi, Y., . . . Ronneberger, O. (2019). U-Net: deep learning for cell counting, detection, and morphometry (vol 16, pg 67, 2019). *Nature Methods, 16*(4), 351-351. doi: 10.1038/s41592-019-0356-4

Farassat, N., Costa, K. M., Stojanovic, S., Albert, S., Kovacheva, L., Shin, J., . . . Roeper, J. (2019). In vivo functional diversity of midbrain dopamine neurons within identified axonal projections. *eLife, 8*. doi: 10.7554/eLife.48408

Fisher, R. B. (1996). *Hypermedia image processing reference*.

Fu, Y., Yuan, Y., Halliday, G., Rusznák, Z., Watson, C., & Paxinos, G. (2012). A cytoarchitectonic and chemoarchitectonic analysis of the dopamine cell groups in the substantia nigra, ventral tegmental area, and retrorubral field in the mouse. *Brain Structure and Function, 217*(2), 591-612. doi: 10.1007/s00429-011-0349-2

Gantz, S. C., Ford, C. P., Morikawa, H., & Williams, J. T. (2018). The Evolving Understanding of Dopamine Neurons in the Substantia Nigra and Ventral Tegmental Area. *Annu Rev Physiol, 80*, 219-241. doi: 10.1146/annurev-physiol-021317-121615

German, D. C., Manaye, K., Smith, W. K., Woodward, D. J., & Saper, C. B. (1989). Midbrain dopaminergic cell loss in Parkinson's disease: computer visualization. *Annals of Neurology: Official Journal of the American Neurological Association and the Child Neurology Society, 26*(4), 507-514.

Glock, C., Biever, A., Tushev, G., Nassim-Assir, B., Kao, A., Bartnik, I., . . . Schuman, E. M. (2021). The translatome of neuronal cell bodies, dendrites, and axons. *Proc Natl Acad Sci U S A, 118*(43). doi: 10.1073/pnas.2113929118

Golub, V. M., Brewer, J., Wu, X., Kuruba, R., Short, J., Manchi, M., . . . Reddy, D. S. (2015). Neurostereology protocol for unbiased quantification of neuronal injury and neurodegeneration. *Front Aging Neurosci, 7*, 196. doi: 10.3389/fnagi.2015.00196

Gómez-de-Mariscal, E., García-López-de-Haro, C., Ouyang, W., Donati, L., Lundberg, E., Unser, M., . . . Sage, D. (2021). DeepImageJ: A user-friendly environment to run deep learning models in ImageJ. *Nature Methods, 18*(10), 1192-1195.

Gong, S., Doughty, M., Harbaugh, C. R., Cummins, A., Hatten, M. E., Heintz, N., & Gerfen, C. R. (2007). Targeting Cre Recombinase to Specific Neuron Populations with Bacterial Artificial Chromosome Constructs. *The Journal of Neuroscience, 27*(37), 9817-9823. doi: 10.1523/jneurosci.2707-07.2007

González-Hernández, T., Cruz-Muros, I., Afonso-Oramas, D., Salas-Hernández, J., & CastroHernández, J. (2010). Vulnerability of Mesostriatal Dopaminergic Neurons in Parkinson's Disease. *Front Neuroanat, 4*. doi: 10.3389/fnana.2010.00140

Greener, J. G., Kandathil, S. M., Moffat, L., & Jones, D. T. (2022). A guide to machine learning for biologists. *Nature Reviews Molecular Cell Biology, 23*(1), 40-55. doi: 10.1038/s41580-021-00407-0

Haber, S. N., & Fudge, J. L. (1997). The primate substantia nigra and VTA: integrative circuitry and function. *Critical Reviews™ in Neurobiology, 11*(4).

Haddjeri-Hopkins, A., Tapia, M., Ramirez-Franco, J., Tell, F., Marqueze-Pouey, B., Amalric, M., & Goaillard, J. M. (2021). Refining the Identity and Role of Kv4 Channels in Mouse Substantia Nigra Dopaminergic Neurons. *eNeuro, 8*(4). doi: 10.1523/ENEURO.0207-21.2021

Halliday, G., Reyes, S., & Double, K. (2012). Substantia nigra, ventral tegmental area and retrorubral fields. *The human nervous system*, 439-455.

Hassabis, D., Kumaran, D., Summerfield, C., & Botvinick, M. (2017). Neuroscience-Inspired Artificial Intelligence. *Neuron, 95*(2), 245-258. doi: https://doi.org/10.1016/j.neuron.2017.06.011

Hassler, R. 1238 Zur Pathologic der Paralysis Agitans und des Post-Enzephalitischen Parkinsonismus. *J. Psychol. Neurol, 18*, 387.

Healy-Stoffel, M., Ahmad, S. O., Stanford, J. A., & Levant, B. (2012). A novel use of combined tyrosine hydroxylase and silver nucleolar staining to determine the effects of a unilateral intrastriatal 6-hydroxydopamine lesion in the substantia nigra: A stereological study. *Journal of Neuroscience Methods, 210*(2), 187-194. doi: https://doi.org/10.1016/j.jneumeth.2012.07.013

Helmstadter, K. G., Ljubojevic-Holzer, S., Wood, B. M., Taheri, K. D., Sedej, S., Erickson, J. R., . . . Bers, D. M. (2021). CaMKII and PKA-dependent phosphorylation co-regulate nuclear localization of HDAC4 in adult cardiomyocytes. *Basic Res Cardiol, 116*(1), 11. doi: 10.1007/s00395-021-00850-2

Hirsch, E. C., Faucheux, B., Damier, P., Mouatt-Prigent, A., & Agid, Y. (1997). Neuronal vulnerability in Parkinson's disease. *J Neural Transm Suppl, 50*, 79-88. doi: 10.1007/978-3-7091-6842-4_9

Hobson, B. D., Choi, S. J., Mosharov, E. V., Soni, R. K., Sulzer, D., & Sims, P. A. (2022). Subcellular proteomics of dopamine neurons in the mouse brain. *eLife, 11*, e70921. doi: 10.7554/eLife.70921

Hobson, B. D., Kong, L., Angelo, M. F., Lieberman, O. J., Mosharov, E. V., Herzog, E., . . . Sims, P. A. (2022). Subcellular and regional localization of mRNA translation in midbrain dopamine neurons. *Cell Rep, 38*(2), 110208. doi: 10.1016/j.celrep.2021.110208

Hofman, F. (2002). Immunohistochemistry. *Curr Protoc Immunol, Chapter 21*, Unit 21 24. doi: 10.1002/0471142735.im2104s49

Holland, I., & Davies, J. A. (2020). Automation in the Life Science Research Laboratory. *Front Bioeng Biotechnol, 8*, 571777. doi: 10.3389/fbioe.2020.571777

Hurd, Y., Pristupa, Z., Herman, M., Niznik, H., & Kleinman, J. (1994). The dopamine transporter and dopamine D2 receptor messenger RNAs are differentially expressed in limbic-and motor-related subpopulations of human mesencephalic neurons. *Neuroscience, 63*(2), 357-362.

Jauhar, S., Johnstone, M., & McKenna, P. J. (2022). Schizophrenia. *Lancet, 399*(10323), 473-486. doi: 10.1016/s0140-6736(21)01730-x

Jellinger, K. A. (2012). Neuropathology of sporadic Parkinson's disease: evaluation and changes of concepts. *Movement disorders, 27*(1), 8-30.

Jolly, S., Lang, V., Koelzer, V. H., Sala Frigerio, C., Magno, L., Salinas, P. C., . . . Palomer, E. (2019). Single-Cell Quantification of mRNA Expression in The Human Brain. *Sci Rep, 9*(1), 12353. doi: 10.1038/s41598-019-48787-w

Jonkman, J., Brown, C. M., Wright, G. D., Anderson, K. I., & North, A. J. (2020). Tutorial: guidance for quantitative confocal microscopy. *Nat Protoc, 15*(5), 1585-1611. doi: 10.1038/s41596-020-0313-9

Katikireddy, K. R., & O'Sullivan, F. (2011). Immunohistochemical and immunofluorescence procedures for protein analysis. *Methods Mol Biol, 784*, 155-167. doi: 10.1007/978-1-61779-289-2_11

Kegeles, L. S., Abi-Dargham, A., Frankle, W. G., Gil, R., Cooper, T. B., Slifstein, M., . . . Laruelle, M. (2010). Increased synaptic dopamine function in associative regions of the striatum in schizophrenia. *Arch Gen Psychiatry, 67*(3), 231-239. doi: 10.1001/archgenpsychiatry.2010.10

Kim, H. F., Ghazizadeh, A., & Hikosaka, O. (2015). Dopamine neurons encoding long-term memory of object value for habitual behavior. *Cell, 163*(5), 1165-1175.

Kingma, D. P., & Ba, J. (2014). Adam: A method for stochastic optimization. *arXiv preprint arXiv:1412.6980*.

Klein, M. O., Battagello, D. S., Cardoso, A. R., Hauser, D. N., Bittencourt, J. C., & Correa, R. G. (2019). Dopamine: Functions, Signaling, and Association with Neurological Diseases. *Cell Mol Neurobiol, 39*(1), 31-59. doi: 10.1007/s10571-018-0632-3

Kordower, J. H., Olanow, C. W., Dodiya, H. B., Chu, Y., Beach, T. G., Adler, C. H., . . . Bartus, R. T. (2013). Disease duration and the integrity of the nigrostriatal system in Parkinson's disease. *Brain, 136*(8), 2419-2431. doi: 10.1093/brain/awt192

Kornilov, A. S., & Safonov, I. V. (2018). An Overview of Watershed Algorithm Implementations in Open Source Libraries. *Journal of Imaging, 4*(10), 123.

Kraus, O. Z., Grys, B. T., Ba, J., Chong, Y., Frey, B. J., Boone, C., & Andrews, B. J. (2017). Automated analysis of high-content microscopy data with deep learning. *Mol Syst Biol, 13*(4), 924. doi: 10.15252/msb.20177551

Krenn, M., Pollice, R., Guo, S. Y., Aldeghi, M., Cervera-Lierta, A., Friederich, P., . . . Nigam, A. (2022). On scientific understanding with artificial intelligence. *Nature Reviews Physics*, 1-9.

Lammel, S., Hetzel, A., Hackel, O., Jones, I., Liss, B., & Roeper, J. (2008). Unique properties of mesoprefrontal neurons within a dual mesocorticolimbic dopamine system. *Neuron, 57*(5), 760-773. doi: 10.1016/j.neuron.2008.01.022

Lammel, S., Steinberg, Elizabeth E., Földy, C., Wall, Nicholas R., Beier, K., Luo, L., & Malenka, Robert C. (2015). Diversity of Transgenic Mouse Models for Selective Targeting of Midbrain Dopamine Neurons. *Neuron, 85*(2), 429-438. doi: https://doi.org/10.1016/j.neuron.2014.12.036

LeCun, Y., Bengio, Y., & Hinton, G. (2015). Deep learning. *Nature, 521*(7553), 436-444. doi: 10.1038/nature14539

Lerner, Talia N., Shilyansky, C., Davidson, Thomas J., Evans, Kathryn E., Beier, Kevin T., Zalocusky, Kelly A., . . . Deisseroth, K. (2015). Intact-Brain Analyses Reveal Distinct Information Carried by SNc Dopamine Subcircuits. *Cell, 162*(3), 635-647. doi: https://doi.org/10.1016/j.cell.2015.07.014

Levet, F., Carpenter, A. E., Eliceiri, K. W., Kreshuk, A., Bankhead, P., & Haase, R. (2021). Developing open-source software for bioimage analysis: opportunities and challenges. *F1000Res, 10*, 302. doi: 10.12688/f1000research.52531.1

Li, X., Qi, J., Yamaguchi, T., Wang, H. L., & Morales, M. (2013). Heterogeneous composition of dopamine neurons of the rat A10 region: molecular evidence for diverse signaling properties. *Brain Struct Funct, 218*(5), 1159-1176. doi: 10.1007/s00429-012-0452-z

Lichtman, J. W., & Conchello, J. A. (2005). Fluorescence microscopy. *Nature Methods, 2*(12), 910-919. doi: 10.1038/nmeth817

Lin, M., Chen, Q., & Yan, S. (2013). Network in network. *arXiv preprint arXiv:1312.4400*.

Liss, B., Franz, O., Sewing, S., Bruns, R., Neuhoff, H., & Roeper, J. (2001). Tuning pacemaker frequency of individual dopaminergic neurons by Kv4.3L and KChip3.1 transcription. *EMBO J, 20*(20), 5715-5724. doi: 10.1093/emboj/20.20.5715

Liss, B., Haeckel, O., Wildmann, J., Miki, T., Seino, S., & Roeper, J. (2005). K-ATP channels promote the differential degeneration of dopaminergic midbrain neurons. *Nat Neurosci, 8*(12), 1742-1751. doi: 10.1038/nn1570

Liss, B., & Surmeier, D. J. (2022). Calcium Channels and Selective Neuronal Vulnerability in Parkinson's Disease *Voltage-Gated Calcium Channels* (pp. 575-598): Springer.

Liu, C., & Kaeser, P. S. (2019). Mechanisms and regulation of dopamine release. *Curr Opin Neurobiol, 57*, 46-53. doi: 10.1016/j.conb.2019.01.001

Long, J., Shelhamer, E., & Darrell, T. (2015). Fully Convolutional Networks for Semantic Segmentation. *2015 Ieee Conference on Computer Vision and Pattern Recognition (Cvpr)*, 3431-3440. doi: DOI 10.1109/cvpr.2015.7298965

Maffeis, V., Cappellesso, R., Nicolè, L., Guzzardo, V., Menin, C., Elefanti, L., . . . Fassina, A. (2019). Loss of BAP1 in Pheochromocytomas and Paragangliomas Seems Unrelated to Genetic Mutations. *Endocrine Pathology, 30*(4), 276-284. doi: 10.1007/s12022-019-09595-0

Maier-Hein, L., Eisenmann, M., Reinke, A., Onogur, S., Stankovic, M., Scholz, P., . . . Kopp-Schneider, A. (2018). Why rankings of biomedical image analysis competitions should be interpreted with care. *Nat Commun, 9*(1), 5217. doi: 10.1038/s41467-018-07619-7

Matsumoto, M., & Hikosaka, O. (2009). Two types of dopamine neuron distinctly convey positive and negative motivational signals. *Nature, 459*(7248), 837-841. doi: 10.1038/nature08028

McCutcheon, R. A., Abi-Dargham, A., & Howes, O. D. (2019). Schizophrenia, dopamine and the striatum: from biology to symptoms. *Trends Neurosci, 42*(3), 205-220.

McQuin, C., Goodman, A., Chernyshev, V., Kamentsky, L., Cimini, B. A., Karhohs, K. W., . . . Carpenter, A. E. (2018). CellProfiler 3.0: Next-generation image processing for biology. *PLoS Biol, 16*(7), e2005970. doi: 10.1371/journal.pbio.2005970

Menegas, W., Babayan, B. M., Uchida, N., & Watabe-Uchida, M. (2017). Opposite initialization to novel cues in dopamine signaling in ventral and posterior striatum in mice. *eLife, 6*. doi: 10.7554/eLife.21886

Miles, R. E., & Davy, P. (1976). Precise and general conditions for the validity of a comprehensive set of stereological fundamental formulae. *Journal of Microscopy, 107*(3), 211-226. doi: https://doi.org/10.1111/j.1365-2818.1976.tb02444.x

Miller, D. R., Guenther, D. T., Maurer, A. P., Hansen, C. A., Zalesky, A., & Khoshbouei, H. (2021). Dopamine Transporter Is a Master Regulator of Dopaminergic Neural Network Connectivity. *The Journal of Neuroscience, 41*(25), 5453. doi: 10.1523/JNEUROSCI.0223-21.2021

Moen, E., Bannon, D., Kudo, T., Graf, W., Covert, M., & Van Valen, D. (2019). Deep learning for cellular image analysis. *Nature Methods, 16*(12), 1233-1246. doi: 10.1038/s41592-019-0403-1

Montero, T., Gatica, R. I., Farassat, N., Meza, R., González-Cabrera, C., Roeper, J., & Henny, P. (2021). Dendritic Architecture Predicts in vivo Firing Pattern in Mouse Ventral Tegmental Area and Substantia Nigra Dopaminergic Neurons. *Frontiers in Neural Circuits, 15*. doi: 10.3389/fncir.2021.769342

Morales, M., & Margolis, E. B. (2017). Ventral tegmental area: cellular heterogeneity, connectivity and behaviour. *Nature Reviews Neuroscience, 18*(2), 73-85. doi: 10.1038/nrn.2016.165

Mouton, P. R., Phoulady, H. A., Goldgof, D., Hall, L. O., Gordon, M., & Morgan, D. (2017). Unbiased estimation of cell number using the automatic optical fractionator. *Journal of Chemical Neuroanatomy, 80*, A1-A8. doi: https://doi.org/10.1016/j.jchemneu.2016.12.002

Nair, V., & Hinton, G. E. (2010). *Rectified linear units improve restricted boltzmann machines*. Paper presented at the Proceedings of the 27th International Conference on International Conference on Machine Learning, Haifa, Israel.

Naranjo, J. R., & Mellström, B. (2012). Ca2+-dependent transcriptional control of Ca2+ homeostasis. *J Biol Chem, 287*(38), 31674-31680. doi: 10.1074/jbc.R112.384982

Nelson, E. L., Liang, C. L., Sinton, C. M., & German, D. C. (1996). Midbrain dopaminergic neurons in the mouse: computer-assisted mapping. *J Comp Neurol, 369*(3), 361-371. doi: 10.1002/(sici)1096-9861(19960603)369:3<361::aid-cne3>3.0.co;2-3

Noori, H. R., & Fornal, C. A. (2011). The Appropriateness of Unbiased Optical Fractionators to Assess Cell Proliferation in the Adult Hippocampus. *Front Neurosci, 5*. doi: 10.3389/fnins.2011.00140

Ortner, N. J. (2021). Voltage-Gated Ca(2+) Channels in Dopaminergic Substantia Nigra Neurons: Therapeutic Targets for Neuroprotection in Parkinson's Disease? *Front Synaptic Neurosci, 13*, 636103. doi: 10.3389/fnsyn.2021.636103

Osborne, P., Halliday, G., Cooper, H., & Keast, J. (2005). Localization of immunoreactivity for deleted in colorectal cancer (DCC), the receptor for the guidance factor netrin-1, in ventral tier dopamine projection pathways in adult rodents. *Neuroscience, 131*(3), 671-681.

Owen, M. J., Sawa, A., & Mortensen, P. B. (2016). Schizophrenia. *Lancet, 388*(10039), 86-97. doi: 10.1016/s0140-6736(15)01121-6

Paget-Blanc, V., Pfeffer, M. E., Pronot, M., Lapios, P., Angelo, M. F., Walle, R., . . . Herzog, E. (2022). A synaptomic analysis reveals dopamine hub synapses in the mouse striatum. *Nat Commun, 13*(1), 3102. doi: 10.1038/s41467-022-30776-9

Palermo, G., & Ceravolo, R. (2019). Molecular Imaging of the Dopamine Transporter. *Cells, 8*(8), 872.

Papathanou, M., Dumas, S., Pettersson, H., Olson, L., & Wallén-Mackenzie, Å. (2019). Off-Target Effects in Transgenic Mice: Characterization of Dopamine Transporter (DAT)-Cre Transgenic Mouse Lines Exposes Multiple Non-Dopaminergic Neuronal Clusters Available for Selective Targeting within Limbic Neurocircuitry. *eNeuro, 6*(5), ENEURO.0198-0119.2019. doi: 10.1523/ENEURO.0198-19.2019

Paxinos, G., & Keith B. J. Franklin, M. (2007). *The Mouse Brain in Stereotaxic Coordinates*: Elsevier Science.

Peck, A. R., Girondo, M. A., Liu, C., Kovatich, A. J., Hooke, J. A., Shriver, C. D., . . . Rui, H. (2016). Validation of tumor protein marker quantification by two independent automated immunofluorescence image analysis platforms. *Mod Pathol, 29*(10), 1143-1154. doi: 10.1038/modpathol.2016.112

Penttinen, A. M., Parkkinen, I., Blom, S., Kopra, J., Andressoo, J. O., Pitkanen, K., . . . Airavaara, M. (2018). Implementation of deep neural networks to count dopamine neurons in substantia nigra. *Eur J Neurosci, 48*(6), 2354-2361. doi: 10.1111/ejn.14129

Poulin, J.-F., Gaertner, Z., Moreno-Ramos, O. A., & Awatramani, R. (2020). Classification of Midbrain Dopamine Neurons Using Single-Cell Gene Expression Profiling Approaches. *Trends Neurosci, 43*(3), 155-169. doi: 10.1016/j.tins.2020.01.004

Rausch, W. D., Wang, F., & Radad, K. (2022). From the tyrosine hydroxylase hypothesis of Parkinson's disease to modern strategies: a short historical overview. *J Neural Transm (Vienna)*. doi: 10.1007/s00702-022-02488-3

Reilly, W. M., & Obara, C. J. (2021). Advances in Confocal Microscopy and Selected Applications. In J. Brzostowski & H. Sohn (Eds.), *Confocal Microscopy: Methods and Protocols* (pp. 1-35). New York, NY: Springer US.

Rodríguez, M., Barroso-Chinea, P., Abdala, P., Obeso, J., & González-Hernández, T. (2001). Dopamine cell degeneration induced by intraventricular administration of 6-hydroxydopamine in the rat: similarities with cell loss in Parkinson's disease. *Experimental neurology, 169*(1), 163-181.

Roeper, J. (2013). Dissecting the diversity of midbrain dopamine neurons. *Trends Neurosci, 36*(6), 336-342. doi: 10.1016/j.tins.2013.03.003

Ryan, R. M., Ingram, S. L., & Scimemi, A. (2021). Regulation of Glutamate, GABA and Dopamine Transporter Uptake, Surface Mobility and Expression. *Frontiers in Cellular Neuroscience, 15*. doi: 10.3389/fncel.2021.670346

Salatino-Oliveira, A., Rohde, L. A., & Hutz, M. H. (2018). The dopamine transporter role in psychiatric phenotypes. *Am J Med Genet B Neuropsychiatr Genet, 177*(2), 211-231. doi: 10.1002/ajmg.b.32578

Sandoval, A., Duran, P., Corzo-López, A., Fernández-Gallardo, M., Muñoz-Herrera, D., Leyva-Leyva, M., . . . Felix, R. (2022). The role of voltage-gated calcium channels in the pathogenesis of Parkinson’s disease. *International Journal of Neuroscience*, 1-10. doi: 10.1080/00207454.2022.2115905

Sansalone, L., Zhang, R., Evans, R., & Khaliq, Z. (2022). Unraveling the substantia nigra pars lateralis: electrophysiological intrinsic properties of non-canonical dopaminergic neurons. *Soc. Neurosci (SFN), 441.01*.

Savchenko, A., Müller, C., Lubec, J., Leo, D., Korz, V., Afjehi-Sadat, L., . . . Sukhanov, I. (2022). The Lack of Dopamine Transporter Is Associated With Conditional Associative Learning Impairments and Striatal Proteomic Changes. *Front Psychiatry, 13*. doi: 10.3389/fpsyt.2022.799433

Schlaudraff, F., Gründemann, J., Fauler, M., Dragicevic, E., Hardy, J., & Liss, B. (2014). Orchestrated increase of dopamine and PARK mRNAs but not miR-133b in dopamine neurons in Parkinson's disease. *Neurobiol Aging, 35*(10), 2302-2315. doi: 10.1016/j.neurobiolaging.2014.03.016

Serôdio, P., & Rudy, B. (1998). Differential expression of Kv4 K+ channel subunits mediating subthreshold transient K+ (A-type) currents in rat brain. *J Neurophysiol, 79*(2), 1081-1091. doi: 10.1152/jn.1998.79.2.1081

Shin, J., Kovacheva, L., Thomas, D., Stojanovic, S., Knowlton, C. J., Mankel, J., . . . Roeper, J. (2022). Ca(v)1.3 calcium channels are full-range linear amplifiers of firing frequencies in lateral DA SN neurons. *Sci Adv, 8*(23), eabm4560. doi: 10.1126/sciadv.abm4560

Siller, A., Hofer, N. T., Tomagra, G., Burkert, N., Hess, S., Benkert, J., . . . Striessnig, J. (2022). β2-subunit alternative splicing stabilizes Cav2.3 Ca(2+) channel activity during continuous midbrain dopamine neuron-like activity. *eLife, 11*. doi: 10.7554/eLife.67464

Smeland, O. B., Frei, O., Dale, A. M., & Andreassen, O. A. (2020). The polygenic architecture of schizophrenia - rethinking pathogenesis and nosology. *Nat Rev Neurol, 16*(7), 366-379. doi: 10.1038/s41582-020-0364-0

Sommer, C., & Gerlich, D. W. (2013). Machine learning in cell biology - teaching computers to recognize phenotypes. *J Cell Sci, 126*(Pt 24), 5529-5539. doi: 10.1242/jcs.123604

Stan Development, T. (2018). RStan: the R interface to Stan. *R package version 2.17. 3.*

Stuber, Garret D., Stamatakis, Alice M., & Kantak, Pranish A. (2015). Considerations When Using Cre-Driver Rodent Lines for Studying Ventral Tegmental Area Circuitry. *Neuron, 85*(2), 439-445. doi: https://doi.org/10.1016/j.neuron.2014.12.034

Subramaniam, M., Althof, D., Gispert, S., Schwenk, J., Auburger, G., Kulik, A., . . . Roeper, J. (2014). Mutant α-synuclein enhances firing frequencies in dopamine substantia nigra neurons by oxidative impairment of A-type potassium channels. *J Neurosci, 34*(41), 13586-13599. doi: 10.1523/jneurosci.5069-13.2014

Surmeier, D. J., Obeso, J. A., & Halliday, G. M. (2017). Selective neuronal vulnerability in Parkinson disease. *Nature Reviews Neuroscience, 18*(2), 101-113. doi: 10.1038/nrn.2016.178

Todd, K. L., Lipski, J., & Freestone, P. S. (2022). Subthalamic nucleus exclusively evokes dopamine release in the tail of the striatum. *Journal of Neurochemistry, 162*(5), 417-429.

Torres, G. E., Gainetdinov, R. R., & Caron, M. G. (2003). Plasma membrane monoamine transporters: structure, regulation and function. *Nature Reviews Neuroscience, 4*(1), 13-25. doi: 10.1038/nrn1008

Uhl, G. R., Walther, D., Mash, D., Faucheux, B., & Javoy-Agid, F. (1994). Dopamine transporter messenger RNA in Parkinson's disease and control substantia nigra neurons. *Annals of Neurology: Official Journal of the American Neurological Association and the Child Neurology Society, 35*(4), 494-498.

Vaughan, R. A., & Foster, J. D. (2013). Mechanisms of dopamine transporter regulation in normal and disease states. *Trends Pharmacol Sci, 34*(9), 489-496. doi: 10.1016/j.tips.2013.07.005

Vijiaratnam, N., Simuni, T., Bandmann, O., Morris, H. R., & Foltynie, T. (2021). Progress towards therapies for disease modification in Parkinson's disease. *Lancet Neurol, 20*(7), 559-572. doi: 10.1016/s1474-4422(21)00061-2

Vila, M. (2019). Neuromelanin, aging, and neuronal vulnerability in Parkinson's disease. *Mov Disord, 34*(10), 1440-1451. doi: 10.1002/mds.27776

von Chamier, L., Laine, R. F., & Henriques, R. (2019). Artificial intelligence for microscopy: what you should know. *Biochem Soc Trans, 47*(4), 1029-1040. doi: 10.1042/BST20180391

Wang, F., Flanagan, J., Su, N., Wang, L. C., Bui, S., Nielson, A., . . . Luo, Y. (2012). RNAscope: a novel in situ RNA analysis platform for formalin-fixed, paraffin-embedded tissues. *J Mol Diagn, 14*(1), 22-29. doi: 10.1016/j.jmoldx.2011.08.002

Wang, S., Yang, D. M., Rong, R., Zhan, X., & Xiao, G. (2019). Pathology Image Analysis Using Segmentation Deep Learning Algorithms. *Am J Pathol, 189*(9), 1686-1698. doi: 10.1016/j.ajpath.2019.05.007

West, M. J. (1999). Stereological methods for estimating the total number of neurons and synapses: issues of precision and bias. *Trends Neurosci, 22*(2), 51-61. doi: 10.1016/s0166-2236(98)01362-9

Wilkinson, G., & Rogers, C. (1973). Symbolic description of factorial models for analysis of variance. *Journal of the Royal Statistical Society: Series C (Applied Statistics), 22*(3), 392-399.

Wise, R. A. (2004). Dopamine, learning and motivation. *Nature Reviews Neuroscience, 5*(6), 483-494. doi: 10.1038/nrn1406

Xu, Y. K. T., Chitsaz, D., Brown, R. A., Cui, Q. L., Dabarno, M. A., Antel, J. P., & Kennedy, T. E. (2019). Deep learning for high-throughput quantification of oligodendrocyte ensheathment at single-cell resolution. *Commun Biol, 2*, 116. doi: 10.1038/s42003-019-0356-z

Yamada, T., McGeer, P., Baimbridge, K., & McGeer, E. (1990). Relative sparing in Parkinson's disease of substantia nigra dopamine neurons containing calbindin-D28K. *Brain research, 526*(2), 303-307.

Yang, G. R., & Wang, X. J. (2020). Artificial Neural Networks for Neuroscientists: A Primer. *Neuron, 107*(6), 1048-1070. doi: 10.1016/j.neuron.2020.09.005